AE-4

A MODEL ENVIRONMENT FOR OUTER ZONE ELECTRONS

DECEMBER 1972

NATIONAL SPACE SCIENCE DATA CENTER
NATIONAL AERONAUTICS AND SPACE ADMINISTRATION • GODDARD SPACE FLIGHT CENTER, GREENBELT, MD.

NSSDC 72-13

A MODEL ENVIRONMENT FOR OUTER ZONE ELECTRONS

G. Wayne Singley
The KMS Technology Center

and

James I. Vette
Goddard Space Flight Center

National Space Science Data Center
National Aeronautics and Space Administration
Goddard Space Flight Center
Greenbelt, Maryland 20771

December 1972

CONTENTS

LIST OF ILLUSTRATIONS

CONTENTS (continued)

CONTENTS (continued)

CONTENTS (continued)

CONTENTS (continued)

CONTENTS (continued)

NOTATION

A	OGO calibration constant, $1/\bar{\varepsilon}G$
B, B_i	Magnetic field strength
B_0	Magnetic field strength at the equator
B_m	Magnetic field strength at the mirror point
B_c	Atmospheric cutoff magnetic field strength
C_j	Coefficient of local time dependence (equation 4.4)
E	Energy
E_1	Threshold energy (equation 4.1)
E_0	Hardness of exponential spectrum
F	OGO arbitrary count rate
G	Geometric factor or B dependence function (equation 4.3)
j	Integral flux
J	Omnidirectional integral flux (equation 4.5)
$\overline{J}$	Time-averaged omnidirectional integral flux (equation 4.6)
K, K'	Coefficient of omnidirectional flux function (equations 4.5 and 4.6)
L	McIlwain's magnetic shell parameter
m	B dependence parameter (equation 4.3)
N	Equatorial local time averaged flux (equation 4.8)
N	Number of local time intervals (equation 4.8)
P	Pitch angle parameter (equation 4.10)
P_i	Count rate data normalized to the equator (equation 4.12)
r	Detector response, Explorer 26 (equation 4.2)
R, R_i	Omnidirectional count rate (equations 4.2 and 4.12)
R_0	Detector response, ERS 17 (equation 3.3)
R_t	True count rate, ERS 17 (equation 3.3)
R_E	Earth radius
t	Time
α_0	Equatorial pitch angle
ε	Detector efficiency (equation 4.1)

NOTATION (continued)

$\bar{\varepsilon}$	Detector average efficiency (equation 4.1)
θ	Angle between spin axis and B vector (equation 4.2)
τ	Detector dead time (equation 3.3)
ϕ, ϕ_i	Local time
ϕ_j	Coefficient of local time dependence (equation 4.4)
Φ	Local time function (equation 4.4)

1. INTRODUCTION

The AE-4 model of the outer radiation zone electrons has been presented in an earlier document (Singley and Vette, 1972) along with numerous graphs and tables displaying this model in a variety of formats. The purpose of the present report is to give the details of the construction of the AE-4 environment and to show how the model fits the various data from which it was derived.

In Section 2 a brief morphology of outer zone electrons is given to illustrate the nature of the phenomena that we are attempting to model. This is followed by a discussion of the data processing that was done with the various data received from the experimenters before incorporating it into the data base from which this model was ultimately derived. The details of the derivation are given in Section 4, and several comparisons of the final model with the various experimental measurements are presented in the final section.

For those persons interested only in the model and its use, the papers by Singley and Vette (1972) and Teague et al. (1972) will suffice. The present document should be consulted if one is concerned with the accuracy of the model and its overall agreement with various magnetospheric experiments.

2. MORPHOLOGY OF OUTER ZONE ELECTRONS

The morphology of outer zone electrons is very complex, and numerous physical processes contribute to the dynamics of this spatial region. Here we outline and illustrate the main features of the morphology for users of the AE-4 model environment who are unfamiliar with the particle measurements and the physical processes. The simplifications used in constructing the model and the departure from physical reality are described. For more detailed discussions of this region, see the books edited by McCormac (1966, 1968, 1970), the book by Hess (1968), and review articles by Vernov et al. (1969), Williams (1971), and Paulikas (1971).

In a dipole magnetic field, the B, L, ϕ coordinate system we have chosen would be physically meaningful. If there were only a constant number of electrons in the outer zone with no loss mechanisms, there would be no local time variations. The dipole approximation for the earth's internal magnetic field at distances above 2.5 R_E is reasonable. However, the outer zone is surrounded by complex regions of plasmas which strongly determine the behavior of the higher energy particles that we are modeling. The environment near earth is depicted in Figure 1. The solar wind protons, which fill the interplanetary medium to distances well beyond the orbit of the earth, interact with the earth's magnetic field to form a bow shock and a magnetopause. Within the magnetosheath the solar wind protons are diverted around the magnetopause. There is some leakage of plasma through the polar regions, and it is now believed that this plasma forms the main source for the plasma sheet formed in the earth's downwind tail region. The magnetic field lines originating within the earth generally are contained within the magnetopause. Owing to surface currents in the magnetopause, many field lines are swept back to form the geomagnetic tail.

In the resulting field geometry there are only certain magnetic lines that can support stable trapping of particles, and the adiabatic motion is more complex than in a dipole field. Particles that mirror at different points on a magnetic field line at a given longitude will actually mirror on different field lines as they drift in longitude. This effect has been well illustrated by Roederer (1967), who computed the effect known as shell splitting for a model magnetic field similar to the real field depicted in Figure 1. The results are shown in Figures 2 and 3. In Figure 2 the particle mirroring on a common field line in the noon meridian at the points corresponding to given equatorial pitch angles is shown in the midnight meridian plane. The shell splitting effect begins around 5 R_E and becomes more pronounced with larger radial distances. The reverse situation is given in Figure 3, where particles start in the midnight meridian and drift around to noon. As the distance from the earth increases, there are regions where particles starting at midnight will drift out through the magnetopause boundary before reaching the noon meridian. In addition, particles mirroring at high latitude in the noon meridian will drift out in the geomagnetic tail and will be lost from the trapping region. These areas are shown in Figure 4 as quasi-trapping regions. Thus the region covered with our model environment includes portions where particles cannot execute drift motion around the earth. A typical satellite pass through the radiation belt and the dayside pseudo-trapping region is shown in Figure 5.

Very strong sources are continually supplying electrons to the outer zone. In addition, loss processes remove particles from the region. The major mechanism for loss seems to be caused by pitch angle scattering, which produces a diffusion type transport of particles along the magnetic field lines until they are lost or precipitated into the atmosphere. The main processes that produce this scattering are resonant interactions between electromagnetic waves and electrons

in which a momentum transfer results. The resonant condition exists between the gyrofrequency of the particle and the Doppler shifted wave frequency. Processes of this type have been discussed by numerous authors (Dragt, 1961; Dungey, 1963; Cornwall, 1964, 1965, 1966; and Kennel and Petschek, 1966). An illustration of the validity of such a process is shown in Figure 6, which compares the maximum fluxes observed in the outer zone with a theoretical limit resulting from calculations of Kennel and Petschek (1966).

In addition to pitch angle scattering, there are transport mechanisms that result in diffusion of electrons across magnetic field lines. This diffusion results from fluctuating magnetic or electric fields that have power spectra at frequencies near the drift frequency of the particles. There is an extensive literature on radiation belt diffusion; a number of references can be found in the books by McCormac (1966, 1968, 1970) and Hess (1968). An observation of outer zone electrons that clearly suggests rapid radial diffusion is given in Figure 7, where an inward motion of energetic electrons is evident. There is also some coupling between pitch angle diffusion and radial diffusion in the distorted magnetic field of the magnetosphere.

During periods of magnetic substorms when the shape of the magnetic field in the tail is changing, it is now well established that plasma from the plasma sheet is injected into the radiation belts near the midnight meridian. Some of these electrons are accelerated to energies in the 100-keV range as they move inward and begin their drift around the earth. A schematic of this process has been given by Winckler (1970) and is shown in Figure 8. Pitch angle diffusion causes many of these particles to precipitate rapidly into the atmosphere, but large numbers diffuse radially inward, gaining energy.

The result of these processes is an electron distribution that is quite chaotic in time. The typical time behavior at given points in space is shown in Figure 9. The fluxes change two to three orders of magnitude and subsequently decay following magnetic disturbances.

Two features clearly seen in the outer zone fluxes are not represented by the AE-4 model. During quiet periods the equatorial pitch angle distribution observed in the regions where shell splitting occurs shows the normal peaking at $\alpha = 90°$ on the dayside, but near the midnight meridian the peak occurs at angles considerably less than 90°. An example as measured on ATS 1 (Winckler, 1970) is shown in Figure 10. The results are understood in terms of shell splitting and the actual radial gradients of the flux distribution near the noon meridian. Recent results of West et al. (1971) show that the equatorial pitch angle distribution tends to peak at 30° over the dark hemisphere of the magnetopause between about 5 to 15 R_E. This effect requires a B/B_0 variation, which depends on local time and energy. As these refined measurements become available, more sophisticated models hopefully can be constructed.

No attempt has been made to account for the fact that the local time dependence at low altitude (high B values) is different than in the near equatorial regions. To illustrate this point, Figure 11 shows the percentage of occurrence of 40-keV electrons above a given flux threshold that mirror at $B_m \geq 0.56$ gauss. The peak clearly occurs around 0700 hours rather than around 1100 hours as at the equator. In addition, the peak around 0100 hours is not seen at the equator.

In the AE-4 model, some attempt has been made to qualitatively account for the solar cycle effect. The first evidence of such an effect was given by Frank and Van Allen (1966), who noticed that the minimum in the slot region moved outward roughly in accordance with

the decline of the average sunspot number. Vernov et al. (1969) showed that both the maximum and minimum flux positions varied smoothly with solar activity. The analysis presented later in Section 4 with the OGO 1 and OGO 3 data confirms these trends and shows that the variation is not just a shift in the outer radiation belt but a filling up of the inner side of this zone. (See Figures 30 and 31.) Since the peak fluxes are limited by wave-particle interactions, it is understandable that the average fluxes beyond 5 R_E do not increase, even though the frequency of substorm occurrence increases and results in injection of more particles into the belts. However, these particles diffuse into the regions below 5 R_E, and the average fluxes are increased.

3. DATA PROCESSING

Since there was considerable processing of the experimental data used in AE-4 after they were obtained from the principal investigators, this effort is discussed here. The experiments that provided data for the AE-4 study are listed in Table 1. The experimental data processed by NSSDC represent the total data from these experiments available in forms that could be handled appropriately to perform the analysis. The time coverage of the data spans the period August 1959 to March 1968, but there are considerable gaps in this period. Actual time coverage for each satellite is indicated in Figure 12. Smoothed sunspot number vs time is included as an indication of solar cycle activity. The data coverages as a function of L, energy, and local time are given in Figures 13, 14, and 15, respectively. Hopefully, as further data become available to NSSDC, the period of data coverage will be increased and gaps will be eliminated.

Because the available data were in a variety of forms, they were reduced to a common form for comparative analysis. Twenty discrete L values were chosen for individual study so that the variable L did not have to be dealt with explicitly until after the data were analyzed with respect to B and ϕ. The data from some experiments were available at discrete L values, whereas other data had to be interpolated to these values.

The data from the University of Iowa Explorer 12 and Explorer 14 experiments and the Bell Telephone Laboratories Explorer 26 experiment were available on magnetic tapes in chronological order, with position and magnetic coordinates available for each data record. These data were interpolated to discrete L values by performing least squares fits to rate vs L for short segments (approximately 20 data records) of the data. Rates were then calculated for the appropriate discrete L values

in the interval of fit. Position and magnetic coordinates and time were interpolated linearly to the corresponding discrete L values. The fitting technique introduced some smoothing of the data. The Explorer 12 and 14 data had to be corrected for detector dead time using curves provided by Prof. L. A. Frank. Local time and B/B_0 were calculated from given parameters. After interpolation, the data were sorted by L value so that each L set could be analyzed separately.

Data from the experiments on Explorer 6, Explorer 18, and ERS 17 were available as rate vs time plots. The position and magnetic coordinates were available on magnetic tapes as a function of time. The position and magnetic coordinates as well as time were linearly interpolated to discrete L values. Detector rates were read from plots at the interpolated time of discrete L crossings. Local time and B/B_0 were calculated using the equations

$$B/B_0 = BL^3/.311653 \tag{3.1}$$

$$\phi = t + \frac{\text{Longitude}}{15} \tag{3.2}$$

where ϕ is local time in hours, t is universal time of day in hours, and longitude is in degrees east. ERS 17 data were corrected for dead time using the equation

$$R_t = \frac{R_0}{1 - \tau R_0} \tag{3.3}$$

where R_0 is the detector response, R_t is true count rate, and $\tau = 2.5 \times 10^{-6}$ sec (Peterson et al., 1968).

The Explorer 18 (IMP 1) data from K. A. Anderson's experiment posed a peculiar problem. The onboard accumulator for this detector had a capacity of 2^{17} counts (131,072). The accumulation time was

39.36 seconds. While in the radiation belts, the accumulator frequently filled to capacity and recycled, often more than once, during one accumulation time. There was no way to keep track of the number of times the accumulator was filled during the accumulation time. An onboard divide-by-4 circuit provided a number between 0 and 2^{15} (32,728) for telemetering (Anderson et al., 1966).

The counting rates from these data were deduced by analyzing the time plots made by Anderson and associates at the University of California, Berkeley. Because Anderson's prime interest was in data outside the radiation zone where no overflows occurred, the time plots were made by plotting the telemetered rates without regard to accumulator overflow. Determination of the counting rates inside the radiation belts required determination of the number of overflows. As the satellite moved through the radiation belts, one would expect the counting rate to behave in a rather orderly fashion. By looking at the plots with continuous data, it was possible to note when the satellite passed into a region where the accumulator consistently filled to capacity once, then consistently filled to capacity twice, and so on, thus permitting certain determination of the number of overflows. However, when time gaps occurred in the data, the number of overflows often became ambiguous, thus making use of the data impossible.

The parameter plotted on the time plots was telemetered rate times 4 (to account for the onboard divide-by-4 circuit) corrected for dead time. In regions where the accumulator overflowed, the dead-time correction was invalid. Therefore, the rates read from the plots were first "uncorrected" for dead time, the number of accumulator overflows times 2^{17} were added, and the proper dead-time corrections were made using a dead time of $\tau = 10^{-4}$ sec (Anderson et al., 1965).

Data interpolated to discrete L values were provided by McIlwain of the University of California at San Diego, from his experiment flown on Explorer 26. To prepare the data for analysis, the proton background was subtracted and the data were reformatted; the dead-time corrections had been made by McIlwain and associates.

The ERS 13 data were available at discrete L values, and thus only minor reformatting was required to prepare these data for analysis.

The electron spectrometers flown on OGO 1 and OGO 3 by the University of Minnesota (Winckler, Principal Investigator) measured unidirectional electron fluxes in five energy bands. The University of Minnesota group provided data at discrete L values, including arbitrary rate,* equatorial pitch angle, local time, and ephemeris. In addition, plots of arbitrary rate vs L from other time periods were available. Arbitrary rate was read from the plots at the desired L values. The corresponding ephemeris and pitch angle data were read from printouts and were merged with the rate data.

*Arbitrary rate is a normalized rate that allows direct comparison of OGO 1 and OGO 3 data. See Pfitzer (1968), pp. 91-92.

4. DATA ANALYSIS

Analysis of Detector Efficiency

Most of the data were measurements from detectors that were approximately threshold detectors. Detector efficiency under assumed spectral conditions was analyzed using the method outlined by Vette (1966) and Vette et al. (1966). The procedure involves evaluation of the expression

$$\bar{\varepsilon}[E_1] = \frac{\int_0^\infty \varepsilon[E]\ (dj/dE)\ dE}{\int_{E_1}^\infty (dj/dE)\ dE} \qquad (4.1)$$

for assumed differential spectra, dj/dE, and various threshold energies, E_1. For this analysis, differential spectra of the form dj/dE = exp $(-E/E_0)$ were assumed. Plots of $\bar{\varepsilon}$ vs E for various E_1 are presented for the Explorer 6 Geiger-Mueller counter, ion chamber, and scintillation counter in Figures 16 to 18. A nominal threshold energy was chosen for each detector, and thus $\bar{\varepsilon}$ was nearly independent of E_0 over the spectral range that might be encountered. This threshold yielded a single average efficiency value corresponding to a threshold energy that was used to convert count rate to integral flux with little error even though the true value of the spectral parameter E_0 was unknown.

Efficiency vs energy curves were not available for all the detectors from which data were used. Average efficiencies quoted by experimenters were used when the curves were unavailable. The threshold energies and average efficiencies used for the various detectors are summarized in Table 1 with the count rate to flux conversion factors, $1/\bar{\varepsilon}G$. The source is indicated for each case.

The Explorer 26 "D" detector was a directional detector perpendicular to the satellite spin axis. During the early lifetime of the satellite, the spin rate was high enough that the directional accumulation was averaged over several spin periods. Omnidirectional counting rates, R, were estimated using the formula given by McIlwain (1966):

$$R = \frac{r}{1.25 - .5\ \theta/90} \qquad (4.2)$$

where r is detector response in counts per second and θ is the angle in degrees between the satellite spin axis and the local B vector. Because there was a slowdown in the Explorer 26 spin rate, data from the D detector were used only through June 1965.

A detailed analysis of the University of Minnesota OGO 1 and 3 spectrometer efficiency was made by Teague (1970). This instrument measured electrons over five energy windows. The analysis yielded the conversion factors and energy windows shown in Table 2 (after Teague, 1970), which are used in the AE-4 study. The energy bands are designated by the index m.

Radial Profiles, Magnetic Field and Local Time Dependence

Data from each detector were analyzed to obtain the functional dependence of the flux on the chosen variables. This process was evolutionary and resulted in the selection of various functional forms from which a least squares fit to the logarithm of the flux was made to obtain the time averaged behavior as a function of the chosen variables. This process will be described in order to justify the final procedure.

The first method used was described by Vette and Lucero (1967) in constructing the AE-3 environment. The counting rate data over a selected time interval were sorted into B/B_0 cells for each discrete L value. In most cases the number of data points was too small to allow a two-dimensional sort on B/B_0 and ϕ cells simultaneously -- it is important to get a reasonable number of data points in each cell in order to obtain a reliable time average for that cell. By ignoring local time, an average over this variable is, in effect, also performed. To obtain a crude local time dependence, this same process can be repeated using a ϕ cell and ignoring B/B_0.

The B/B_0 dependence of fluxes thus obtained is shown in Figures 19 to 22 for several L values, with the number of data points given beneath each cell. These figures show that in some instances the number of data points was too small to obtain a good time average. Because of the orbit of the satellite, in some cases the number of points in the equatorial cell was adequate to obtain a good determination of average flux at the equator. In other cases, the trend line through the cell averages provided a better estimate of average equatorial flux. From these analyses, it was observed that the B dependence could be adequately represented by the function

$$G[B,L] = (B/B_0)^{-m[L]} \qquad (4.3)$$

In examining the local time dependence through the cell averaging technique, it became apparent that a suitable form was

$$\Phi = 10^{\sum_j C_j \cos\left(\frac{\pi j}{12}(\phi - \phi_j)\right)} \qquad (4.4)$$

Although both first and second order harmonics were investigated, the data coverage clearly warranted carrying only the first term of this series. Furthermore, the ATS 1 data of Paulikas and Blake (1971) showed that the first harmonic was completely adequate. The most extensive data set for determining Φ at any L value was clearly these ATS 1 data. However, as will be seen later, the coefficient C_1 obtained for the ATS 1 data was lower than the coefficient for the data from other satellites. This might be attributed to a solar cycle effect, but this relationship cannot be completely established on the basis of the present data.

To account for both B and ϕ dependence, the iterative cell averaging procedure of Vette and Lucero could have been used. However, a least squares fit using the related functional forms offered a more direct means of handling the data.

Because of the large time variation of the flux at any point, a linearly weighted least squares program will on occasion give a distorted functional form because of a few high flux points. It was decided to work with the logarithm of the flux in the least squares analysis because this method would give relatively less weighting to storm time conditions when the fluxes were elevated. On the other hand, this procedure gives the time average of the log of the flux, and for practical purposes it is more desirable to know the time average of the flux itself. The procedure adopted for low-altitude satellite data was to fit the logarithm of the counting rate using a least squares criterion with the following functional form

$$\log_{10} J[>E,B,L,\phi] = \log_{10} K' - m[L] \log_{10}(B/B_0) + C_1[E,L] \cos\left(\frac{\pi}{12}(\phi - \phi_1)\right) \tag{4.5}$$

The Generalized Least Squares with Statistics (GLSWS) program, described by Daniels (1966), was used to determine the coefficients K', m, C_1, and ϕ_1. To find the correct time averaged value of the flux for the data sample, the following equation was solved for the parameter K:

$$\bar{J} = \sum_{i=1}^{M} \frac{J_i}{M} = K \sum_{i=1}^{M} (B_i/B_0)^{-m} \, 10^{C_1 \cos\left(\frac{\pi}{12}(\phi_i - \phi_1)\right)} \tag{4.6}$$

This procedure was performed for each set of data at each discrete L. Thus the time averaged flux was represented functionally by

$$\bar{J} = K(B/B_0)^{-m} \, 10^{C_1 \cos\left(\frac{\pi}{12}(\phi - \phi_1)\right)} \tag{4.7}$$

The local time variation (the final term in the above equation) as determined by the fits is plotted for three data sets in Figures 23 to 25. These plots illustrate a low-amplitude random behavior at low L values. Above L = 5, however, a fairly consistent pattern emerges. The amplitude (C_1) of the function is greater than the "noise" at lower L values, and the phase (ϕ_1) varies between 0900 and 1200 hours. The local-time-averaged radial profile at the geomagnetic equator was obtained for each sample by integrating the result over local time and setting $B = B_0$. Thus,

$$N[E,L] = K \frac{1}{N} \sum_{n=1}^{N} \int_{\phi=n}^{n+1} 10^{C_1 \cos\left(\frac{\pi}{12}(\phi - \phi_1)\right)} d\phi \tag{4.8}$$

where the integral was performed only over the 1-hour local time intervals that contain 1% or more of the data points in the total sample (N was the total number of such intervals). In other words,

the functional fits were used to integrate over local time, but those segments of local time in which there were little or no data available were not included.

For the Explorer 26 detectors, the number of data points at each L value was large enough to sort into B/B_0-ϕ cells. For these data sets, the above fits were performed using the logarithm of the cell averages of counting rates weighted by the standard deviation of the cell averages of the logarithm of the counting rates. Details of the analysis of data from Explorer 26 detectors are given by Singley (1971a, b).

Sample radial profiles of equatorial flux obtained using the above techniques are shown in Figures 26 to 28. Although each method produced a different radial profile for a given set of data, the differences were within a factor of 2. The data sets represented on the plots range from 1959 to 1967; in this form, the solar cycle effects are difficult to see. However, the L position of the outer zone maxima as observed from these plots demonstrates an outward movement as solar minimum is approached. This movement is illustrated more clearly in Figure 29, where the L values of the peak fluxes are plotted as a function of time.

Solar cycle effects are more clearly demonstrated by comparison of the spectrometer data from OGO 1 and OGO 3. The OGO 1 data were taken in 1964 during solar minimum conditions. The OGO 3 data were taken in late 1966 and in 1967, when the sunspot number was rising rapidly to its maximum value for this cycle (see Figure 12). In addition, the two experiments used identical energy windows and were intercalibrated, thus aiding comparison of the two data sets.

Because the spectrometers made unidirectional measurements of flux over energy windows, the analysis procedures were necessarily different. Average pitch angle distributions for each energy window were determined by making least squares fits with the function

$$\log_{10} F[L,\phi,\alpha_0] = K'[L] + P[L] \log_{10} (\sin \alpha_0) + \log_{10}\Phi[\phi] \quad (4.9)$$

to the equatorial pitch angle data taken over several months. In this function, F is arbitrary rate* and α_0 is equatorial pitch angle. Normalization of the function to the average of the local time dependence as in equation 4.8 yields the following representation of the average pitch angle distribution of arbitrary counting rate:

$$F[L,\alpha_0] = K[L] (\sin \alpha_0)^{P[L]} \quad (4.10)$$

Unidirectional flux was obtained using

$$j[L,\alpha_0] = F[L,\alpha_0] (A \cdot \Delta E) \quad (4.11)$$

where $(A \cdot \Delta E)$ is given for each energy band in Table 2. Omnidirectional flux for each energy band was obtained by integration. Integral omnidirectional flux at the equator was then calculated for the lower threshold of each energy window by summing over all higher energy windows. A more complete description of the analysis of the OGO data is given by Singley (1971c). The equatorial radial profiles thus obtained are shown in Figures 30 and 31. These plots show that the slot region was much deeper under solar minimum conditions than during solar maximum conditions. The slot region appears to have filled up during solar maximum, but the profiles at higher L values (L above 5) remained relatively unchanged. Thus the maxima of the profiles moved inward, but this was not a shift of the entire curve.

*Arbitrary rate is a normalized count rate that allows direct comparison of the data from the spectrometers on OGO 1 and OGO 3 (Pfitzer, 1968).

Statistical Variance

Large temporal fluctuations of the electron intensities in the outer radiation belt made it necessary to study the data statistically in order to make meaningful predictions about intensity levels. The logarithm of the flux was found to be approximately normally distributed. The mean (over time) is presented by the AE-4 model. A model for the standard deviation of the distribution function was developed and used in conjunction with the mean to indicate the probability that certain flux levels would be exceeded. An equivalent interpretation is that the probability predicts the fraction of the time that the flux will be in excess of the chosen value.

As in all of the analysis, data from each L set were considered independently. Using the function that was fit to the data, the local time and magnetic field dependence were removed from each rate datum, R_i, thus yielding

$$P_i = \frac{R_i}{G[B_i/B_0]\ \Phi[\phi_i]} \tag{4.12}$$

where G is the functional magnetic field dependence and Φ is the functional local time dependence.

The normality of the logarithm of the rate data was illustrated by comparing the theoretical normal cumulative probability distribution with the empirical cumulative probability distribution. The empirical distribution was tabulated by forming the cumulative probability distribution from the rate frequency distribution. Plots of the theoretical curve (solid line) and the empirical curve (data points) for the four sample cases are given in two different presentations in Figures 32 to 37. Similar plots published by Paulikas and Blake (1971) for

ATS 1 data show similar results. Although the curves do not compare perfectly, the log normal theoretical curves fit the data closely enough to be adequate for modeling purposes.

5. COMPARISON OF THE AE-4 MODEL WITH DATA

The AE-4 model was developed from the results of the data analysis described in the previous section. Radial profiles of equatorial flux for various energies were idealized into spectral maps that plotted smoothly both as a function of energy at constant L and as a function of L for constant energy for two different epochs (Figures 38 to 41). The model curves do not fit the data perfectly, but are representative of all data, especially the OGO data. Comparisons of the model spectral curves and the actual data are made in Figures 42 to 59.

The local time model is also a smoothed representation of the results of the data analyses of all data. The analyses showed that the maximum amplitudes in local time variation occurred between 0900 and 1200 hours local time for most detectors for most L values (above L = 5). The parameter ϕ_1 (in equation 4.4) was set to 11 for the model.

The model amplitude function, C[E,L] (this was denoted as C_1 in equation 4.4), is a smoothed representation of the amplitudes derived from the analyses of the various detectors. The model amplitude is smooth in both the C,E plane and the C,L plane. Systematic differences as a function of solar cycle made it necessary to use two epochs as in the model spectrum. This is illustrated in Figure 60, where the amplitude of the local time variations for the ATS 1 data (1967) is lower than amplitudes from time periods nearer solar minimum.

The model power law parameter for the magnetic field dependence is shown in Figures 61 to 64 along with the power law parameters calculated during the analyses of the data from various detectors. As can be seen from these figures, the model parameter is a very simplified curve. The data do not permit a determination of any energy dependence in this

parameter. To provide a low-altitude cutoff for the model, the flux pair theorem of Roberts (1965) was employed so that the model B dependence is the modified power law

$$G[B,L] = \left(\frac{B}{B_0}\right)^{-m[L]} \left(\frac{B_c - B}{B_c - B_0}\right)^{m[L] + 1/2}$$

The magnetic field cutoff value, B_c, is defined as a function of L by the curve in Figure 65. This curve represents the B values as a function of L for which the maximum altitude is less than or equal to about 200 km. No attempt has been made to have the model fit the electron precipitation patterns nor is the cutoff dependent on longitude. Because of this lack of longitudinal dependence, the model will give very unrealistic fluxes at low altitudes in certain regions. When enough data are available at the National Space Science Data Center, the low-altitude region can be properly treated. It is interesting to compare the model with the Injun 3 302 Geiger tube fluxes presented by Craven (1966). These results are shown in Figure 66. Because the Injun 3 results spanned a large B range, the comparison was made by time averaging the results at each value and using a B value in the model that lay within the range covered by the data.

Assuming a normal distribution for the logarithm of the electron flux levels over time, as demonstrated in the previous section, a model of standard deviations of the flux levels predicted by the AE-4 model was developed. The model is given as a smooth tabular function over E and L, but this is a quantification of a rather subjective picture. (See Figures 67 and 68 for plots of the tabular model.) The model reflects the high variances for low-energy electrons at high L values. The high variances are due to the instabilities in the pseudo-trapping regions. In the same regions, the variance of the

higher energy electrons fall off and disappear, thus reflecting the absence of trapped higher energy electrons in the weak magnetic fields of that region. The variances remain relatively flat in a band across the mid-L region, falling off in an orderly fashion at lower L values, thus indicating more stability just outside the slot region. This mid-L region is affected by only the largest magnetic storms and thus is disturbed less frequently than at higher L. Early data indicated more stability at higher L values, but the variance of Explorer 26 and OGO 1 and 3 data remained high down to $L \simeq 3.5$. A composite display of the standard deviation data as a function of L is given in Figures 69 and 70. Comparisons of the model standard deviation vs energy with the standard deviation data are presented in Figures 71 to 85. Because the standard deviation data did not show significant changes with time, a single standard deviation model was made.

6. REFERENCES

1. Anderson, K. A., H. K. Harris, and R. J. Paoli, "Energetic Electron Fluxes in and Beyond the Earth's Outer Magnetosphere," J. Geophys. Res., 70, 1039-1050, 1965

2. Anderson, K. A., R. J. Paoli, and G. H. Pitt, "Technical Description of the University of California IMP 1 Energetic Particle Equipment," University of California, Berkeley, Space Sciences Laboratory, Sept. 1, 1966.

3. Arnoldy, R. L., R. A. Hoffman, and J. R. Winckler, "Observation of the Van Allen Radiation Regions during August and September, 1959," Part 4, "The Outer-Zone Electrons," J. Geophys. Res., 67, 2595-2612, 1962.

4. Cornwall, J. M., "Scattering of Energetic Trapped Electrons by Very-Low-Frequency Waves," J. Geophys. Res., 69, 1251, 1964.

5. Cornwall, J. M., "Cyclotron Instabilities and Electromagnetic Emission in the Ultra-Low-Frequency and Very-Low-Frequency Ranges," J. Geophys. Res., 70, 61, 1965.

6. Cornwall, J. M., "Micropulsations and the Outer Radiation Zone," J. Geophys. Res., 71, 2185, 1966.

7. Craven, J. D., "Temporal Variations of Electron Intensities at Low Altitudes in the Outer Radiation Zone as Observed with Satellite Injun 3," J. Geophys. Res., 71, 5643, 1966.

8. Daniels, Walter E., Jr., "GLSWS - Generalized Least Squares with Statistics," University of Maryland, Technical Report 579, July 1966.

9. Dragt, A. J., "Effect of Hydromagnetic Waves on the Lifetime of Van Allen Radiation Protons," J. Geophys. Res., 66, 1641, 1961.

10. Dungey, J. W., "Loss of Van Allen Electrons due to Whistlers," Planet. Space Sci., 11, 591, 1963.

11. Frank, L. A., and J. A. Van Allen, "Correlation of Outer Radiation Zone Electrons (E_e~1 Mev) with the Solar Activity Cycle," J. Geophys. Res., 71, 2697, 1966.

12. Hess, W. N., The Radiation Belt and Magnetosphere, 548 pp., Blaisdell, Waltham, Mass., 1968.

13. Kennel, C. F., and H. E. Petschek, "Limit on Stably Trapped Particle Fluxes," J. Geophys. Res., 71, 1, 1966.

14. McCormac, B. M., ed., Radiation Trapped in the Earth's Magnetic Field, 901 pp., D. Reidel, Dordrecht, Holland, 1966.

15. McCormac, B. M., ed., Earth's Particles and Fields, 464 pp., Reinhold, New York, 1968.

16. McCormac, B. M., ed., Particles and Fields in the Magnetosphere, 453 pp., D Reidel, Dordrecht, Holland, 1970.

17. McIlwain, C. E., "The Radiation Belts, Natural and Artificial," Science, 142, 355-361, 1963.

18. McIlwain, C. E., "Processes Acting Upon Outer Zone Electrons, I, Adiabatic Perturbations," UCSD-SP-66-5, 1966.

19. O'Brien, B. J., J. A. Van Allen, C. D. Laughlin, and L. A. Frank, "Absolute Electron Intensities in the Heart of the Earth's Outer Radiation Zone," J. Geophys. Res., 67, 397-403, 1962.

20. Paulikas, G. A., "High-Latitude Particle Precipitation," Rev. Geophys., 9, 659, 1971.

21. Paulikas, G. A., and J. B. Blake, "The Particle Environment of the Synchronous Altitude," Models of the Trapped Radiation Environment, Vol. VII, Long Term Time Variations, NASA SP-3024, 1971.

22. Peterson, L. E., J. L. Matteson, L. Huszar, and J. I. Vette, "Environmental Research Satellite-17 Data Reduction and Analysis," Vol. VII, Final Report, UCSD-SP-68-7, December 1968.

23. Pfitzer, K. A., "An Experimental Study of Electron Fluxes from 50 KeV to 5 MeV in the Inner Radiation Belt," University of Minnesota Technical Report No. CR-123, 1968.

24. Roberts, C. S., "On the Relationship Between the Unidirectional and Omnidirectional Flux of Trapped Particles on a Magnetic Line of Force," J. Geophys. Res., 70, 2517-2528, 1965.

25. Roederer, J. G., "On the Adiabatic Motion of Energetic Particles in a Model Magnetosphere," J. Geophys. Res., 72, 981, 1967.

26. Rosen, A., "The Radiation Belt Boundary Near Solar Cycle Maximum as Determined from the Trapping of Energetic Electrons," J. Geophys. Res., 70, 4793-4816, 1965.

27. Singley, G. W., "The Reduction and Analysis of Electron Data for Outer Zone Electron Model AE-4, Vol. I, Explorer 26, University of California at San Diego Experiment Data," NSSDC 71-06, 1971a.

28. Singley, G. W., "The Reduction and Analysis of Electron Data for Outer Zone Electron Model AE-4, Vol. II, Explorer 26, Bell Telephone Laboratories Experiment Data," NSSDC 71-07, 1971b.

29. Singley, G. W., "The Reduction and Analysis of Electron Data for Outer Zone Electron Model AE-4, Vol. III, OGO 1 and 3 University of Minnesota Experiment Data," NSSDC 71-08, 1971c.

30. Singley, G. W., and J. I. Vette, "The AE-4 Model of the Outer Radiation Zone Electron Environment," NSSDC 72-06, 1972.

31. Teague, M. J., "The Calibration Constants for the OGO 1/3 Electron Spectrometer," NSSDC 70-14, 1970.

32. Teague, M. J., J. Stein, and J. I. Vette, "The Use of the Inner Zone Electron Model AE-5 and Associated Computer Programs," NSSDC 72-11, 1972.

33. Vernov, S. N., E. V. Gorchakov, S. N. Kuznetsov, Ya. I. Logachev, E. N. Sosnovets, and V. G. Stolpousky, "Particle Fluxes in the Outer Geomagnetic Field," Rev. Geophys., 7, 257, 1969.

34. Vette, J. I., Models of the Trapped Radiation Environment, Vol. I, "Inner Zone Electrons and Protons," NASA SP-3024, 1966.

35. Vette, J. I., and A. B. Lucero, Models of the Trapped Radiation Environment, Vol. III, "Electrons at Synchronous Altitudes," NASA SP-3024, 1967.

36. Vette, J. I., A. B. Lucero, and J. A. Wright, Models of the Trapped Radiation Environment, Vol. II, "Inner and Outer Zone Electrons," NASA SP-3024, 1966.

37. West, H. I., Jr., R. M. Burk, and J. R. Walton, "Satellite Studies of Magnetospheric Substorms on August 15, 1968, 6, OGO-5 Energetic Electron Observations - Pitch Angle Distributions in the Nighttime Magnetosphere," University of California, Livermore, UCRL-73315, July 1971. To be published in J. Geophys. Res.

38. Williams, D. J., "Sources, Losses, and Transport of Magnetospherically Trapped Particles," to be published in Proceedings of the International Symposium on Solar-Terrestrial Physics, Leningrad, D. Reidel, Dordrecht, Holland, 1971. Available as ESSA Technical Report ERL 180-SDL 16, 1970.

39. Williams, D. J., J. F. Arens, and L. F. Lanzerotti, "Observations of Trapped Electrons at Low and High Altitudes," J. Geophys. Res., 73, 5673-5696, 1968.

40. Winckler, J. R., "Energetic Electrons in the Van Allen Radiation Belts," in Particles and Fields in the Magnetosphere, ed. B. M. McCormac, D. Reidel, Dordrecht, Holland, 1970.

Table 1. Experimental Data Used to Make Electron Model AE-4

Experimental Group	Satellite	Detector	Type of Measurement	Time Coverage	L Coverage	Nominal E_T (MeV)	Nominal $1/\bar{\varepsilon}G$	Source of ε, G Data
TRW	Expl. 6	Scintillator	omnidirectional	8/59-9/59	2.2-8	0.5	6.25	Rosen (1965)
U. Minn.	Expl. 6	GM	omnidirectional	8/59-10/59	2-8	3	7.75 E3	Arnoldy et al. (1962)
U. Minn.	Expl. 6	Ion Chamber	omnidirectional	8/7/59-8/25/59	2-8	1.6	7.75 E4	Arnoldy et al. (1962)
U. Iowa	Expl. 12	302 GM	omnidirectional	8/61-12/61	2-12	1.9	10.	Vette and Lucero (1967)
U. Iowa	Expl. 14	302 GM	omnidirectional	10/62-8/63	2-12	1.9	10.	Vette and Lucero (1967)
U. Iowa	Expl. 14	213A GM	directional	10/62-8/63	2-12	.040	6.28 E3	O'Brien et al. (1962)
U. Iowa	Expl. 14	213B GM	directional	10/62-8/63	2-12	.23	1.57 E4	O'Brien et al. (1962)
U. Calif. Berkeley	Expl. 18 (IMP 1)	GM-A (BETA)	scatter omni-directional	12/63-5/64	2-12	.045	7 E3	Anderson et al. (1965)
Aerospace	ERS 13	SSD	omnidirectional	7/64-11/64	2.5-8	.7	300	Vette, Private Communication
Aerospace	ERS 17	SSD	omnidirectional	7/65-10/65	2-12	.32	174	Peterson et al. (1968)
Aerospace	ERS 17	LEPM Hi Gain	omnidirectional	7/65-10/65	2-12	.1	25	Peterson et al. (1968)
UCSD	Expl. 26	A	omnidirectional	1/65-12/65	2.5-6.9	4.0	300	McIlwain (1963)
UCSD	Expl. 26	D	directional averaged over spin	1/65-6/65	2.5-7.0	.5	2.5 E4	McIlwain (1967)
BTL	Expl. 26	E1	scatter omni-directional	1/65-5/67	3.5-6.5	1.0	4.19 E3	Williams et al. (1968)
BTL	Expl. 26	E2	scatter omni-directional	1/65-5/67	3.5-6.5	3.5	3.29 E3	Private Calculations
BTL	Expl. 26	E3	scatter omni-directional	1/65-5/67	3.5-6.5	2.5	3.29 E3	Private Calculations
U. Minn.	OGO 1	5-Channel Spectrometer	directional	9/64-6/67	1.3-7.0	See Table 2		Teague (1970)
U. Minn.	OGO 3	5-Channel Spectrometer	directional	6/66-12/67	1.3-8.0	See Table 2		Teague (1970)
U. Iowa	Injun 3	302 GM	omnidirectional	1/63-7/63	3.0-6.0	1.9	10	Vette and Lucero (1967)
Aerospace	ATS 1	E1	omnidirectional	12/66-2/68	6.6	.300		Paulikas and Blake (1971)
Aerospace	ATS 1	E2	omnidirectional	12/66-2/68	6.6	.450		Paulikas and Blake (1971)
Aerospace	ATS 1	E3	omnidirectional	12/66-2/68	6.6	1.05		Paulikas and Blake (1971)
Aerospace	ATS 1	E4	omnidirectional	12/66-2/68	6.6	1.9		Paulikas and Blake (1971)

Table 2. Summary of Energy Bands and Efficiency Characteristics for the OGO 1 and OGO 3 Spectrometers

Energy Band (m)	A_m $(cm^2\text{-sec-ster-keV})^{-1}$	E_m (keV)	E_{m+1} (keV)	ΔE_m (keV)	$A_m \Delta E_m$ $(cm^2\text{-sec-ster})^{-1}$
1	3.691	36	133	97	358
2	6.23	133	292	159	991
3	6.10	292	690	398	2428
4	6.66	690	1970	1280	8525
5*	2.16×10^4	1970	∞ Assumed	-	2.16×10^4

*Channel 5 was effectively a threshold detector with threshold 1970 keV. The A value given is $1/\bar{\varepsilon}G$; $\bar{\varepsilon}$ and G were obtained from Teague (1970).

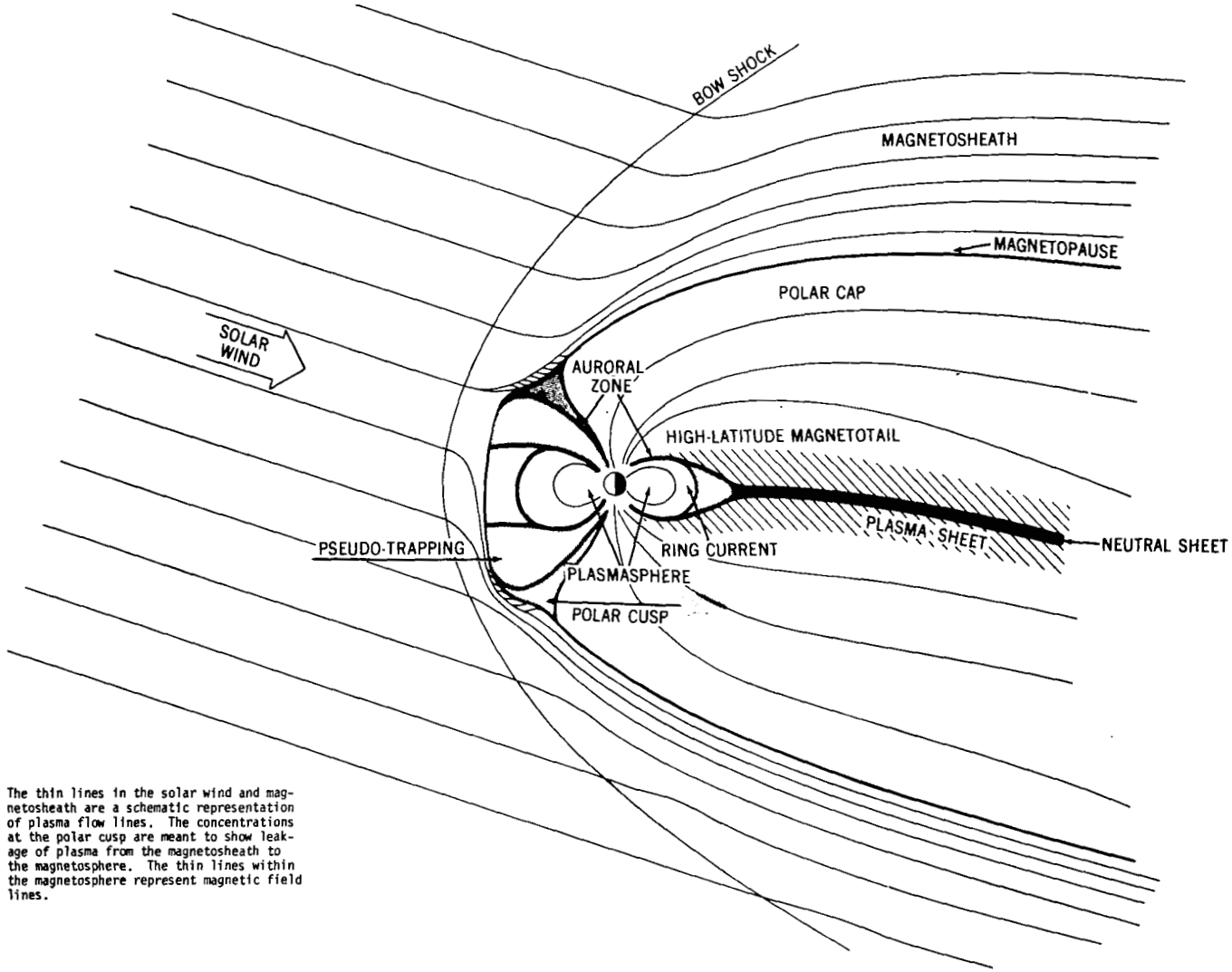

The thin lines in the solar wind and magnetosheath are a schematic representation of plasma flow lines. The concentrations at the polar cusp are meant to show leakage of plasma from the magnetosheath to the magnetosphere. The thin lines within the magnetosphere represent magnetic field lines.

Figure 1. Regions of the Magnetosphere Shown in the Noon-Midnight Meridian Plane

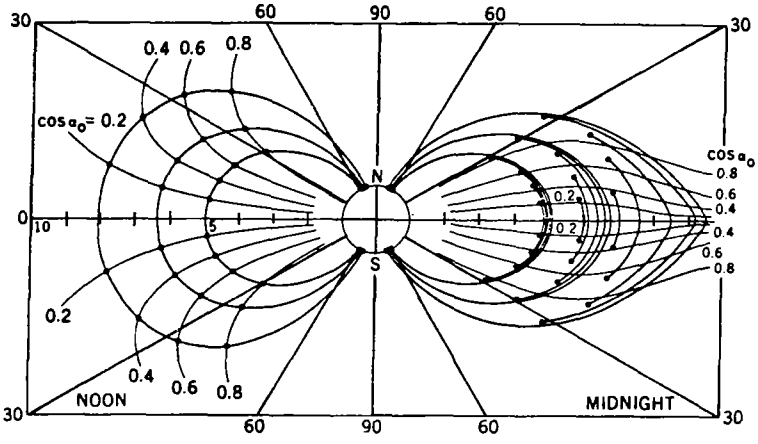

Dots represent particles' mirror points. Curves giving position of mirror points for constant equal pitch angle α_o are shown.

Figure 2. Computed Shell Splitting for Particles Starting on Common Field Lines in the Noon Meridian (Taken from Roederer, 1967)

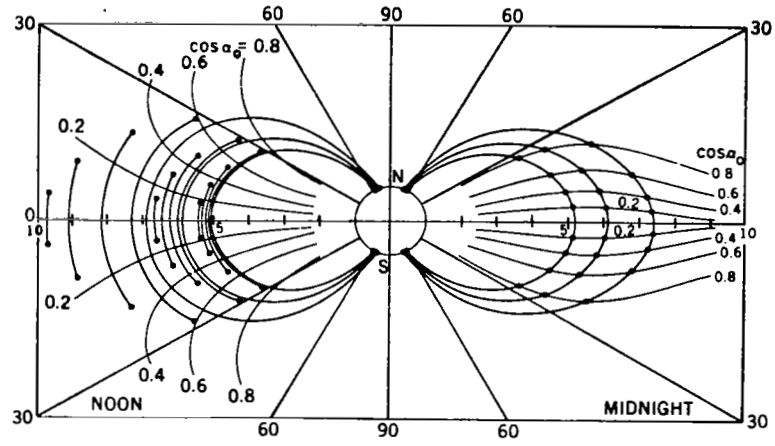

Figure 3. Computed Shell Splitting for Particles Starting on Common Field Lines in the Midnight Meridian (Taken from Roederer, 1967)

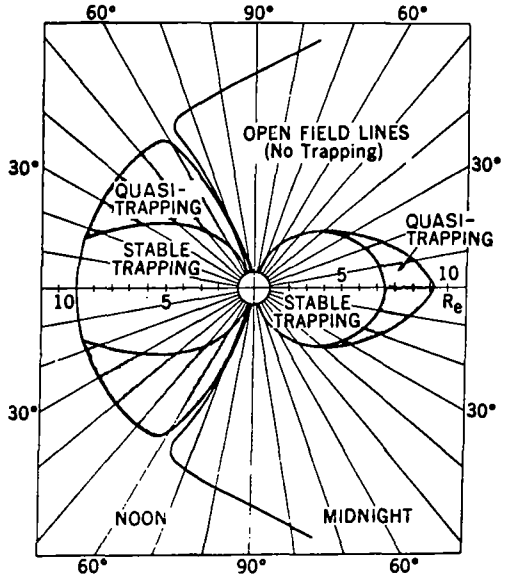

Figure 4. Location of the Quasi- or Pseudo-Trapping Regions in the Magnetosphere (Taken from Roederer, 1967)

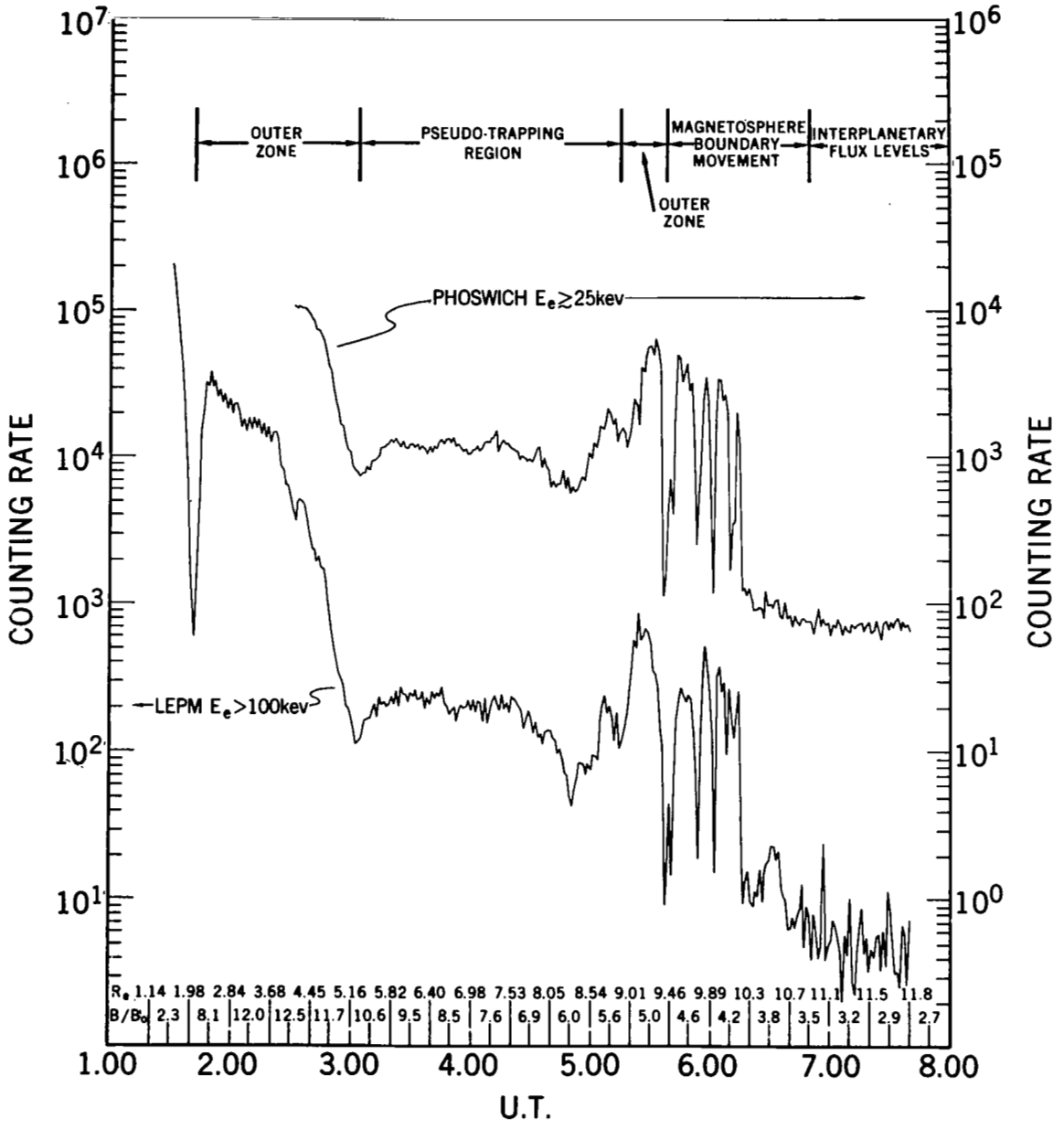

Figure 5. Typical Electron Flux Profiles Obtained in Passing Through the Outer Zone, the Pseudo-Trapping Region, and the Magnetopause, and into the Magnetosheath, Where Interplanetary Flux Levels Are Seen for the Particles of the Energies Shown

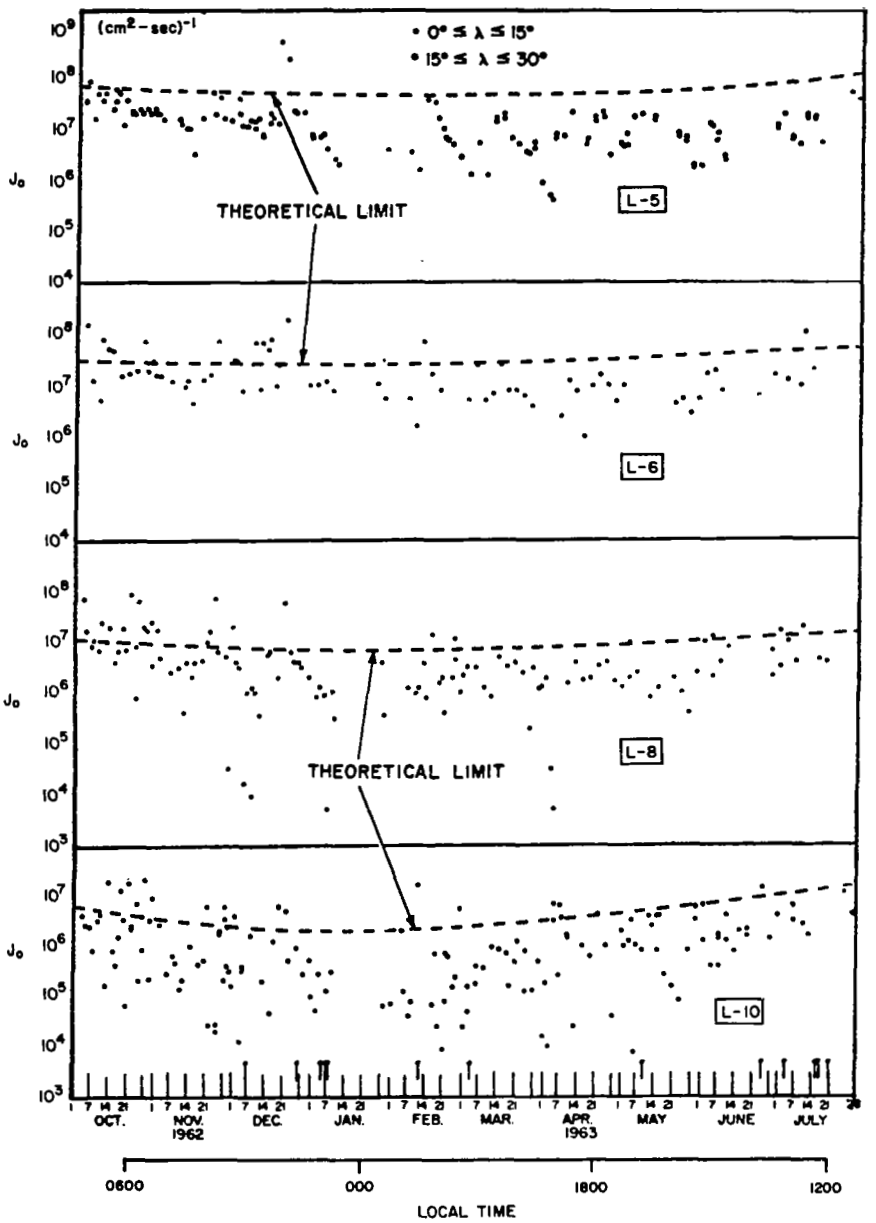

The calculated limits are shown as dotted lines, and the Explorer 14 data are shown as points. The small scatter of points at L = 6 suggested a region of strong acceleration that is now understood in terms of substorm injection.

Figure 6. Limitation on Trapped Electrons >40 keV by Wave-Particle Interactions (Taken from Kennel and Petschek, 1966)

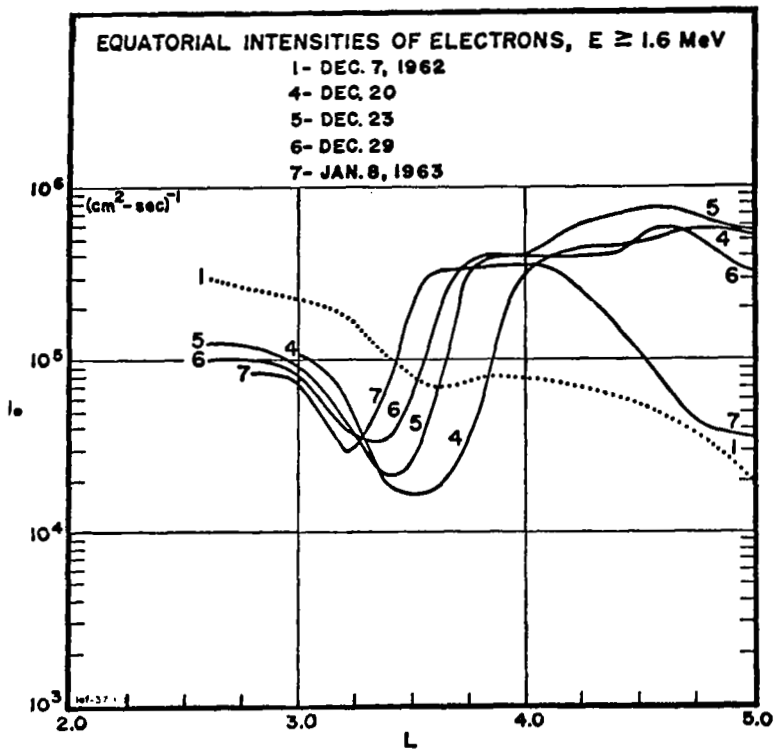

Figure 7. Electron Radial Distribution Showing Inward Motion
$E \gtrsim 1.6$ MeV Electrons Following a Magnetic Storm
(Taken from Frank et al., 1964)

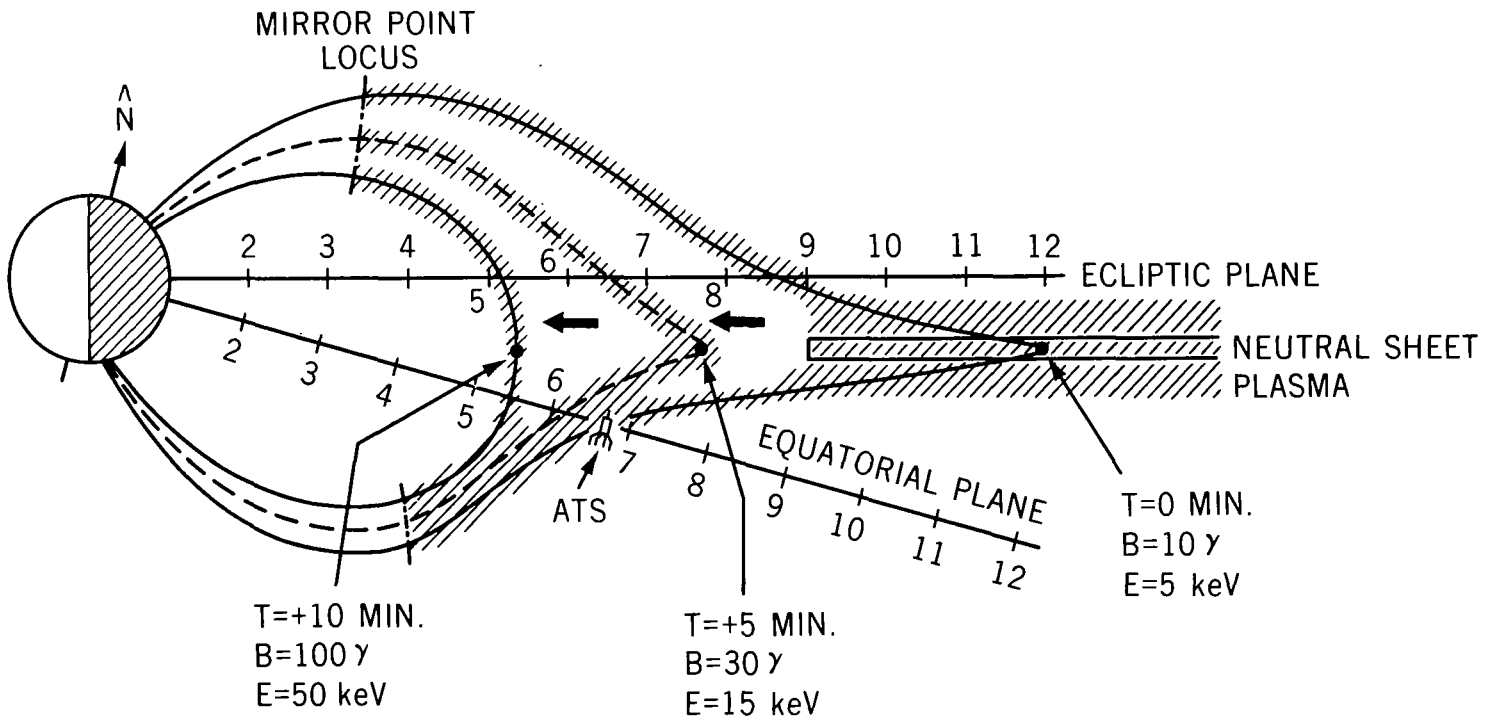

The three contours show possible successive positions of a line of force during the substorm and the resultant field strengths and particle energies.

Figure 8. Plausible Geometry Derived from Actual Observations Showing Possible Acceleration Effects During the Post-Midnight Injection Associated with Substorms (Taken from Winckler, 1970)

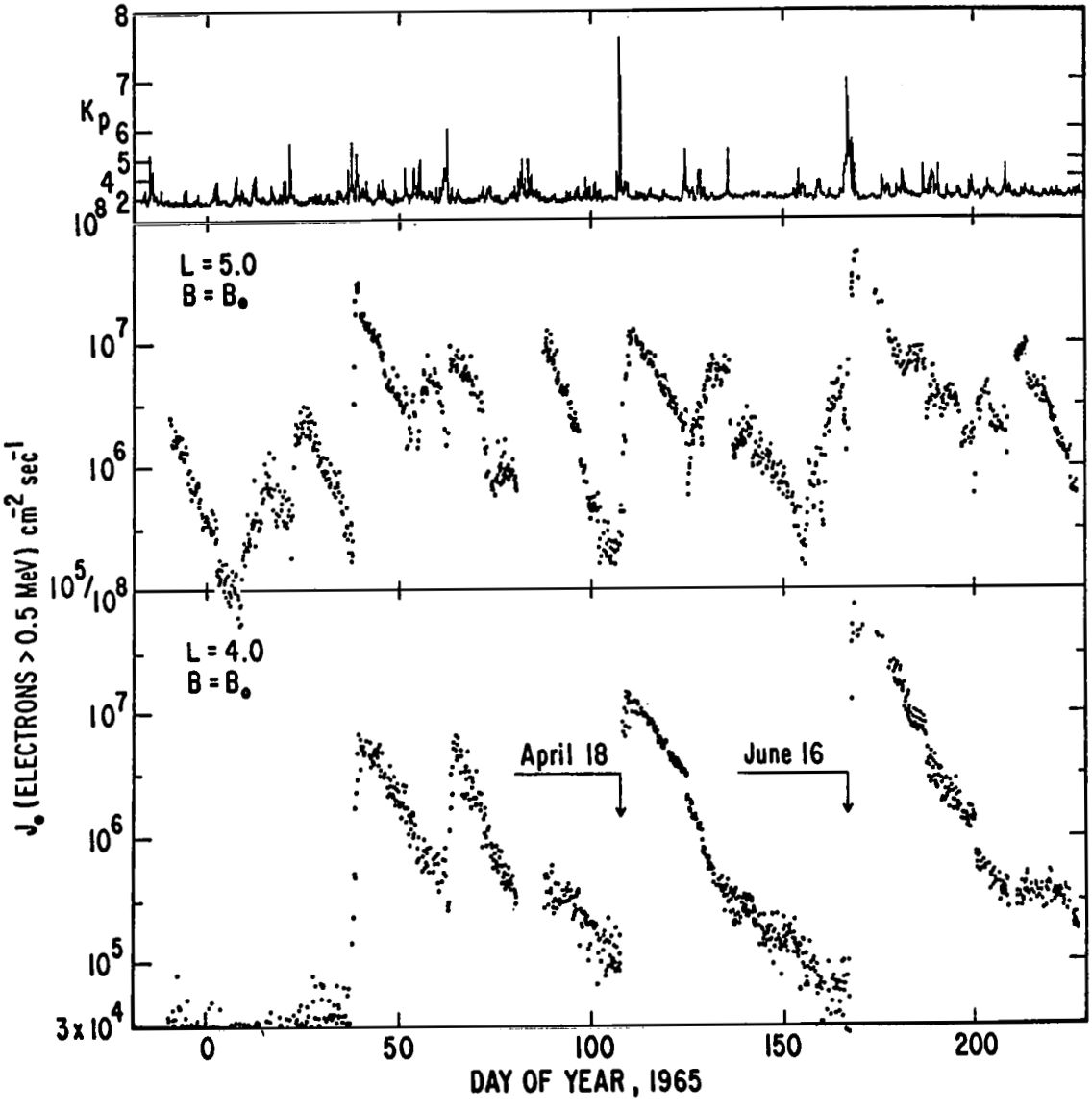

The measurements have been converted to the equatorial flux values. The 3-hour magnetic index, Kp, is at the top of the graph. Intense magnetic storms occurred on April 18 and June 16, 1965.

Figure 9. Omnidirectional Flux of Electrons Greater than 0.5 MeV as a Function of Time in the Outer Zone (Taken from McIlwain, 1966)

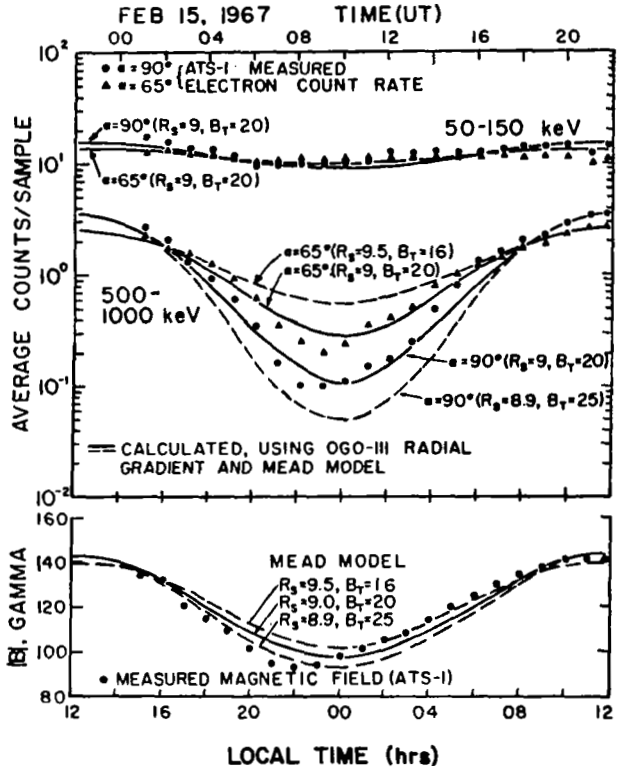

Figure 10. Quiet Day Pitch Angle Variation at Synchronous Orbit Showing Greater Intensity of Particles Mirroring Off the Equator at Midnight

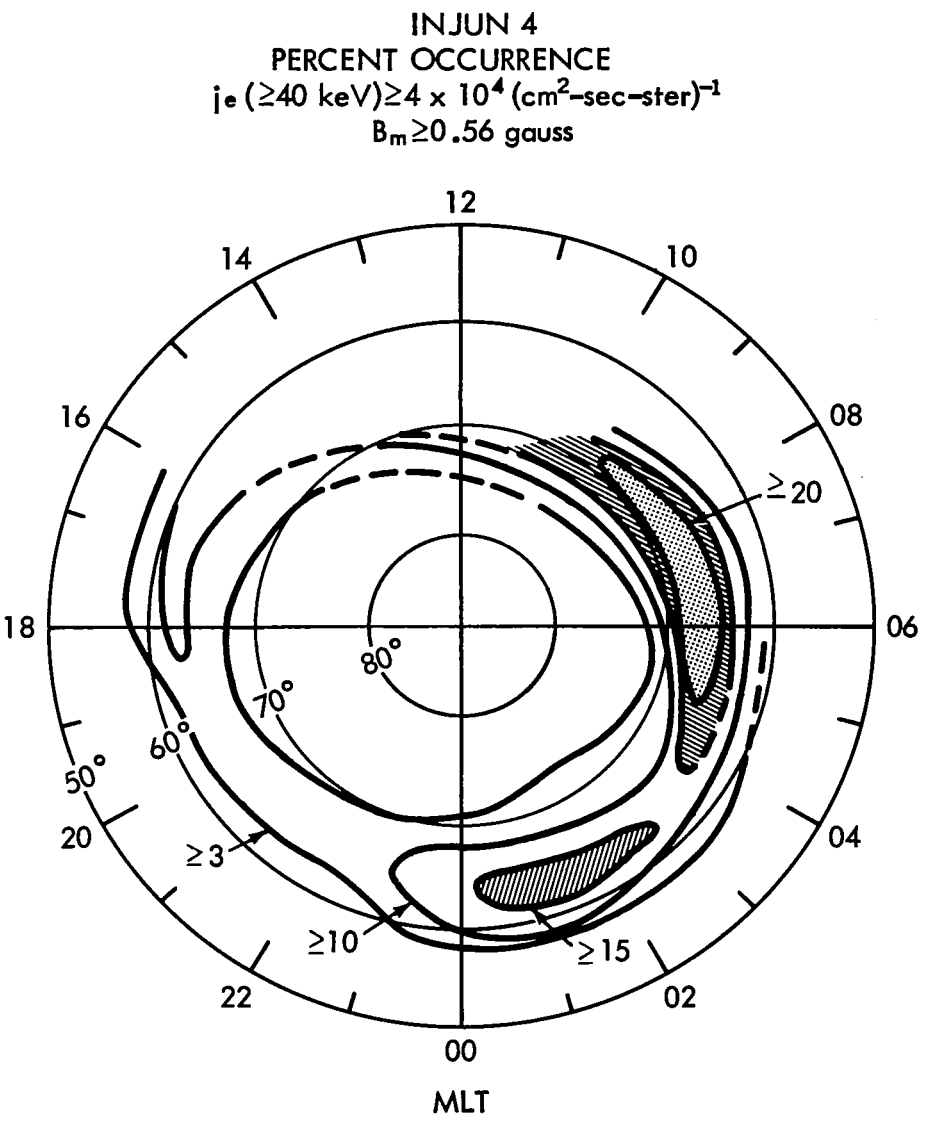

Figure 11. Percentage of Occurrence of j (>40 keV) Mirroring at Bm > 0.56 gauss as Observed Aboard Injun 4 (by J. D. Craven, Taken from Paulikas, 1971)

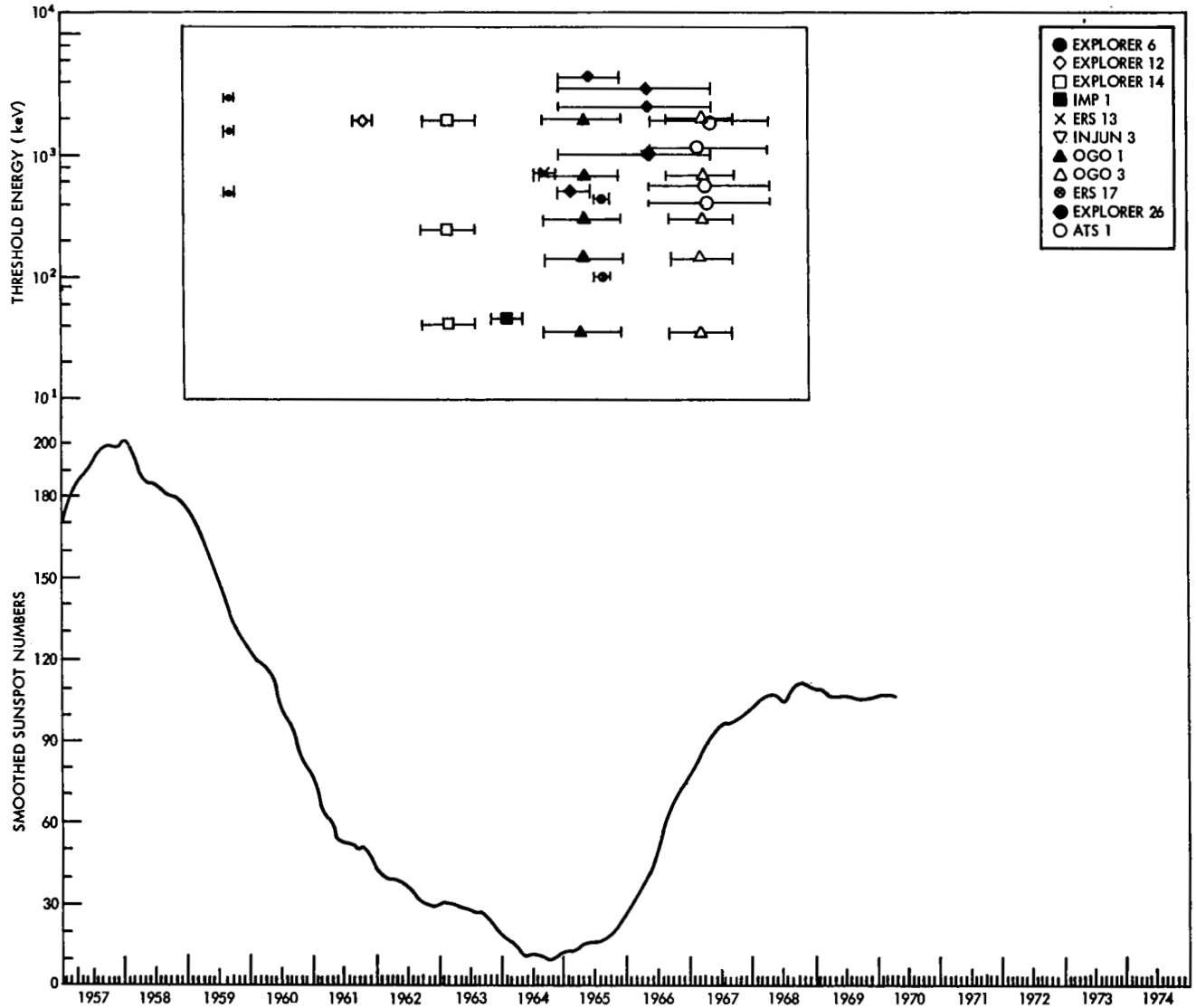

Figure 12. Smoothed Sunspot Number vs Time Indicates Solar Cycle; Time Spans Are Indicated for the Various Data Sets Used

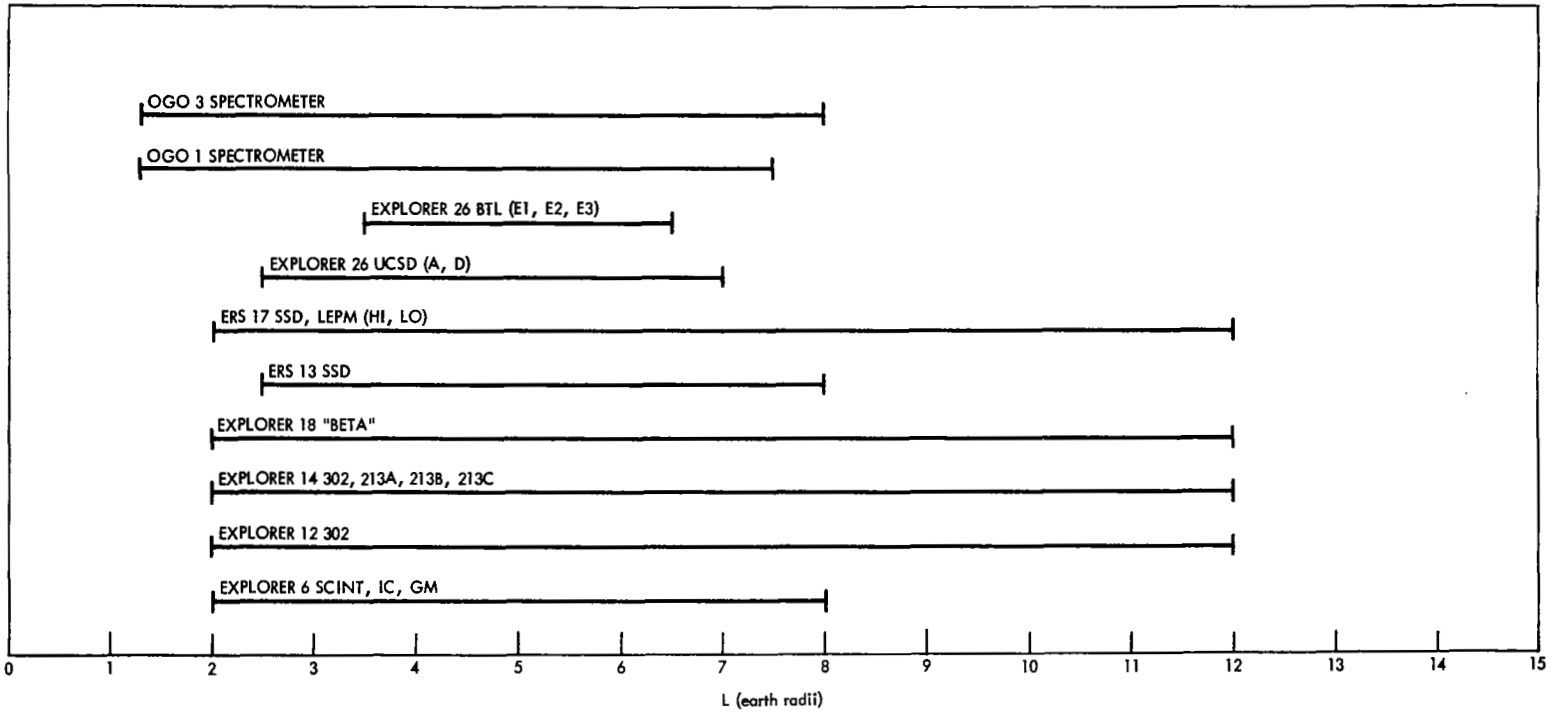

Figure 13. L-Ranges of Data Analyzed for AE-4

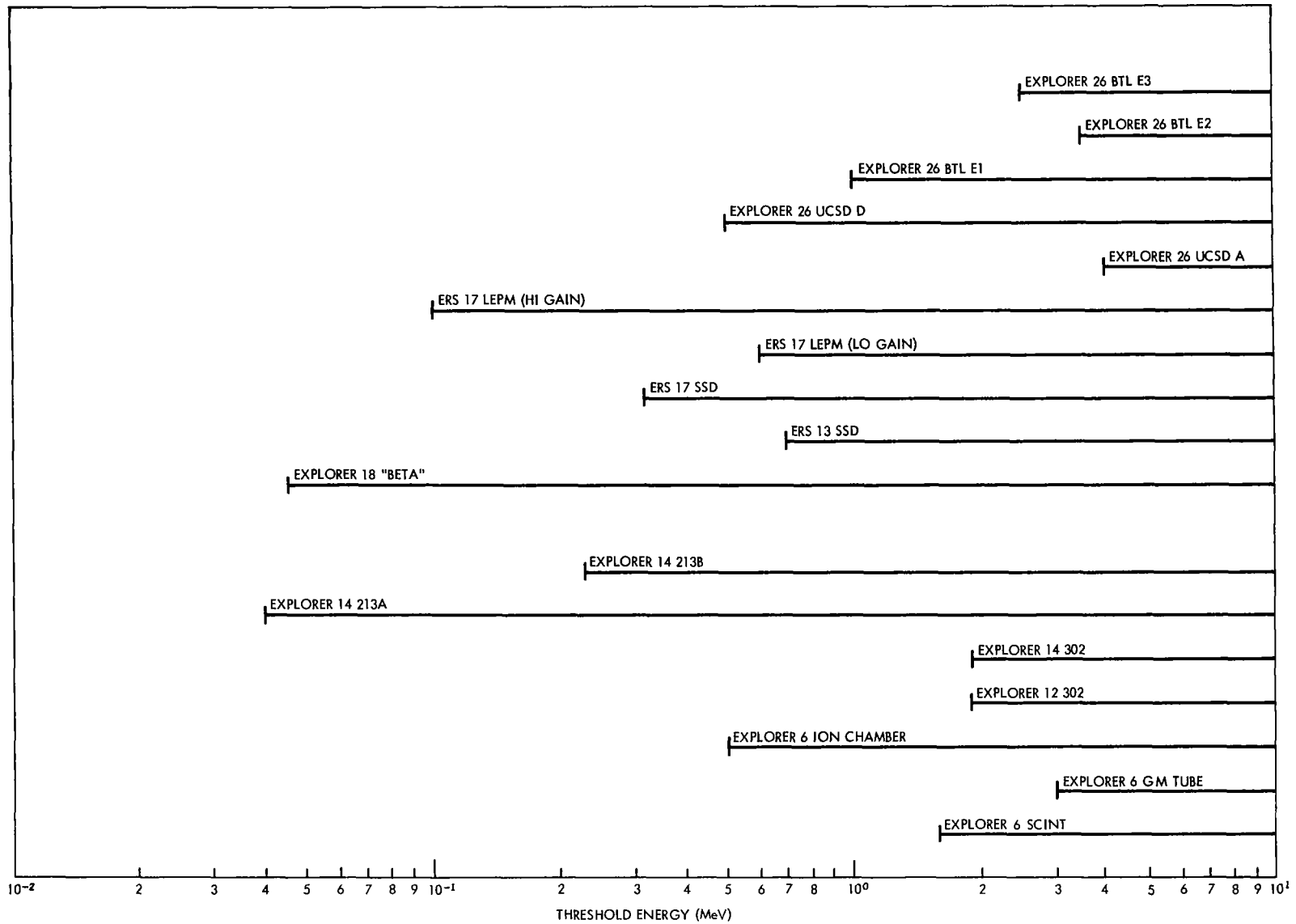

Figure 14. Energy Response of Detectors Used for AE-4

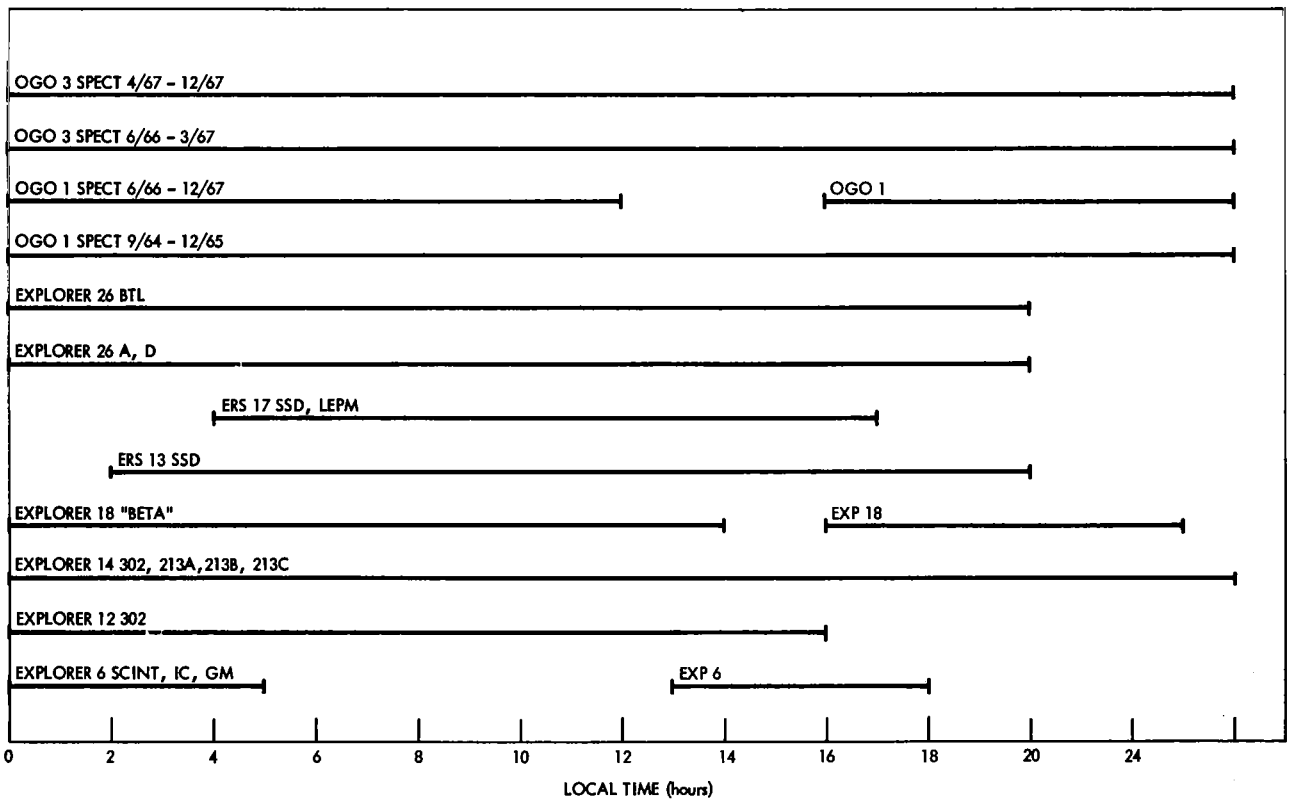

Figure 15. Local Time Coverage of Data Analyzed for AE-4

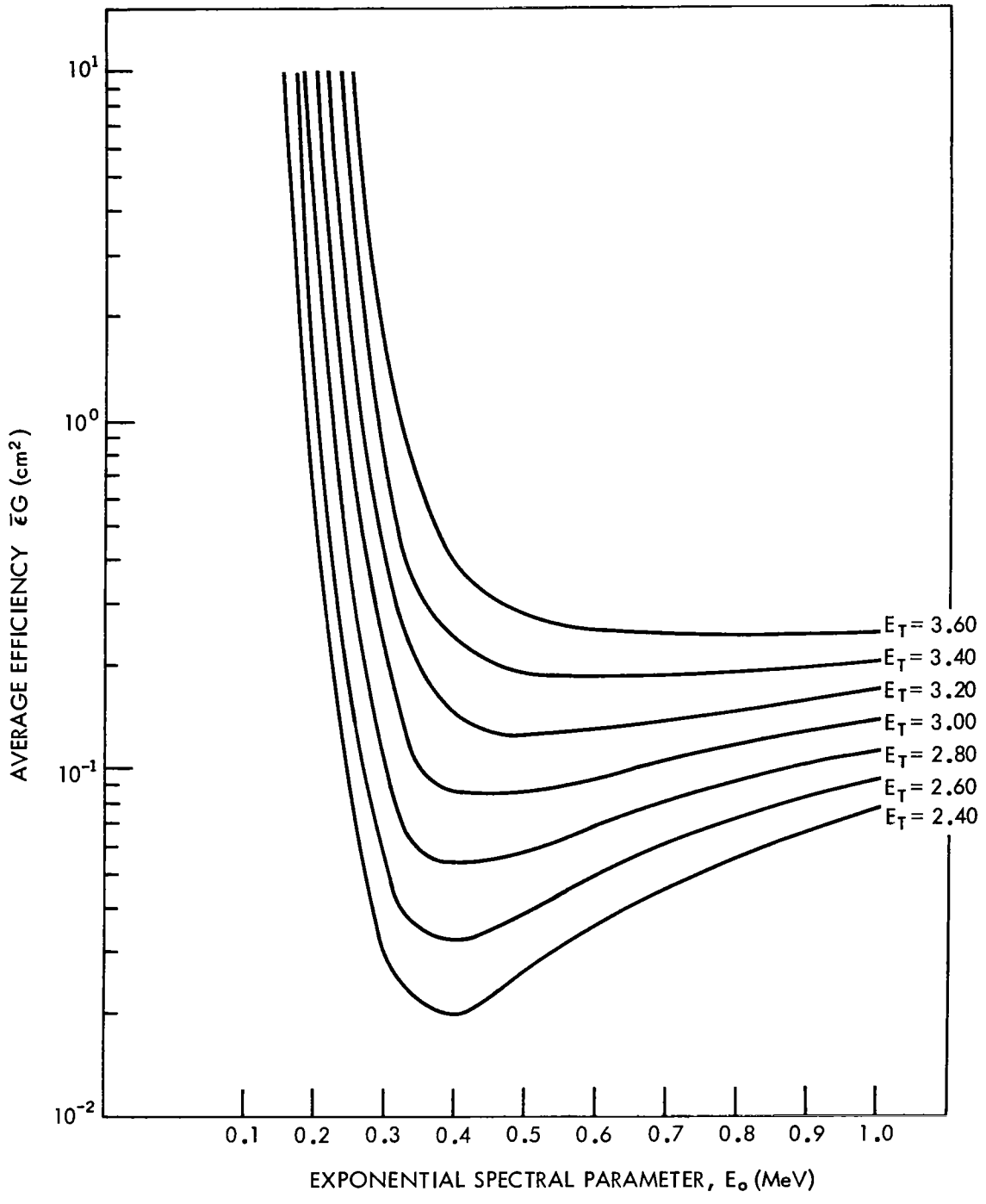

Figure 16. Average Efficiency vs Spectral Parameter for Several Threshold Energies for Explorer 6 GM Counter

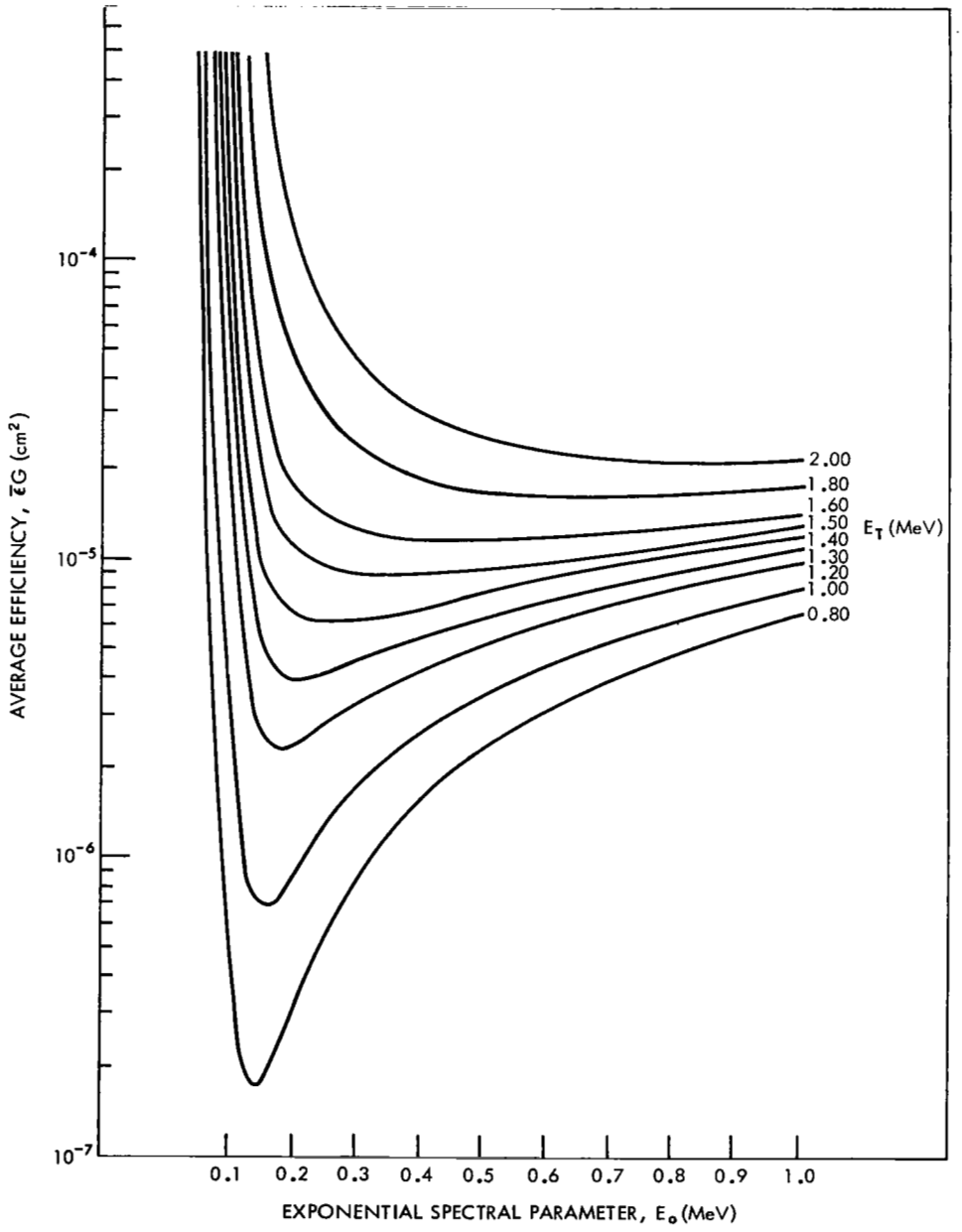

Figure 17. Average Efficiency vs Spectral Parameter for Several Threshold Energies for Explorer 6 Ion Chamber

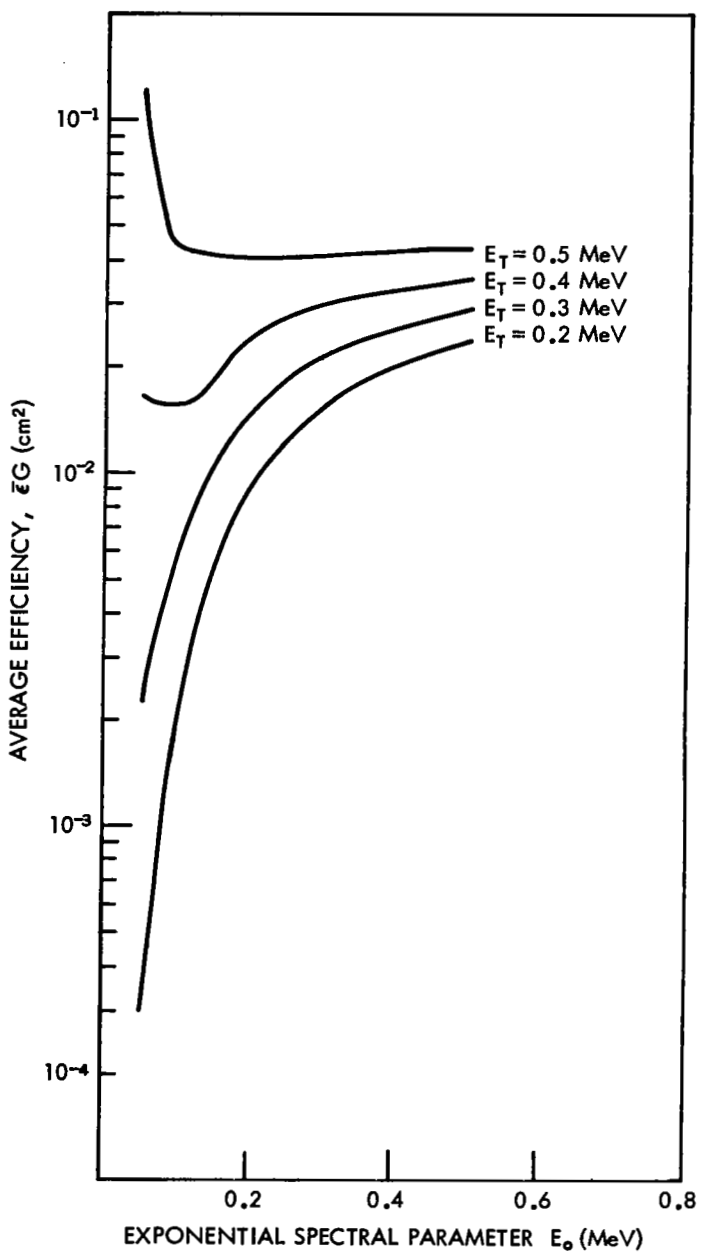

Figure 18. Average Efficiency vs Spectral Parameter for Several Threshold Energies for Explorer 6 Scintillation Counter

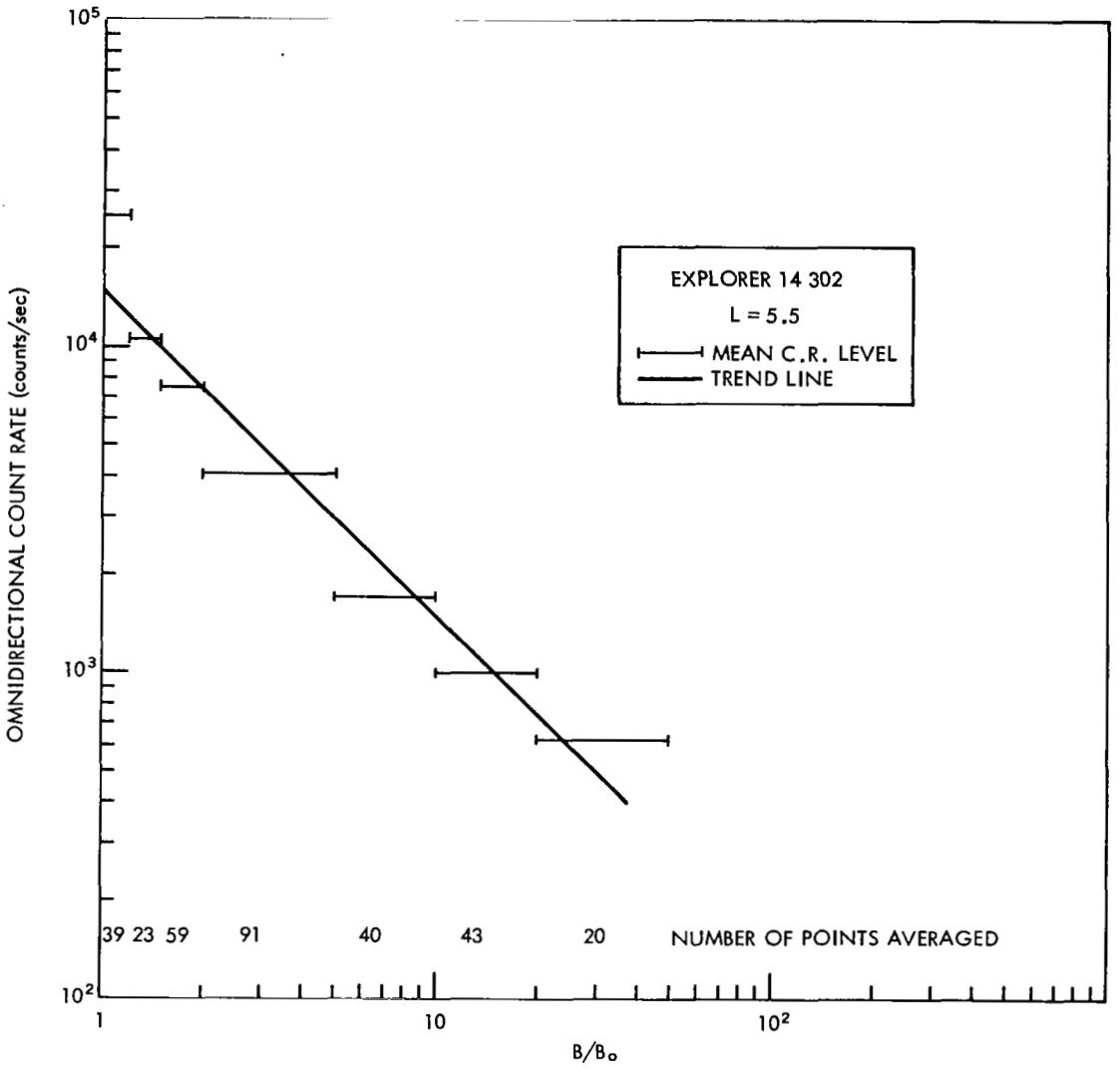

Figure 19. Analysis of B/B_0 Dependence of Omnidirectional Count Rate, Explorer 14 302 GM Counter Data at L = 5.5

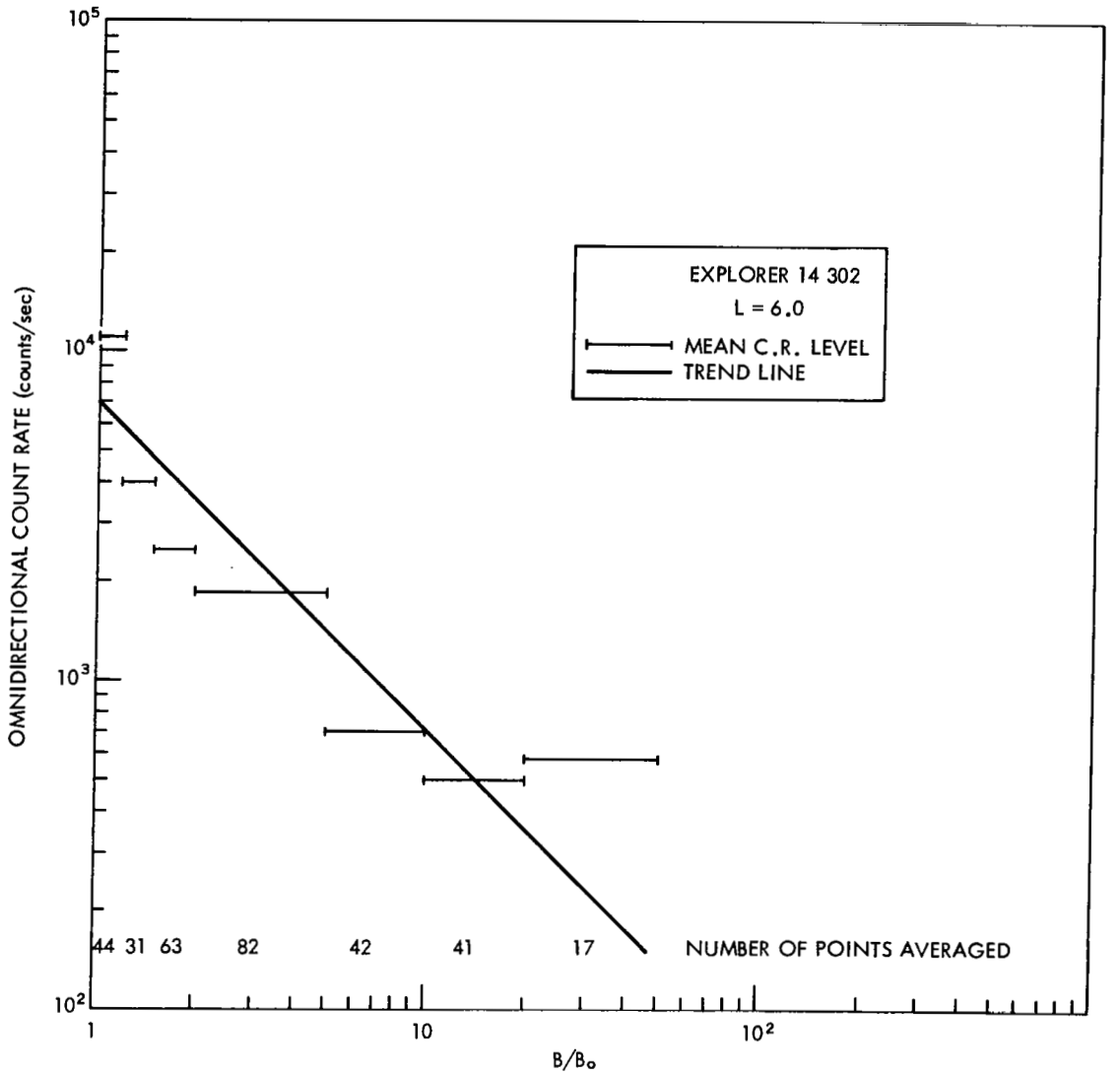

Figure 20. Analysis of B/B_0 Dependence of Omnidirectional Count Rate, Explorer 14 302 GM Counter Data at L = 6.0

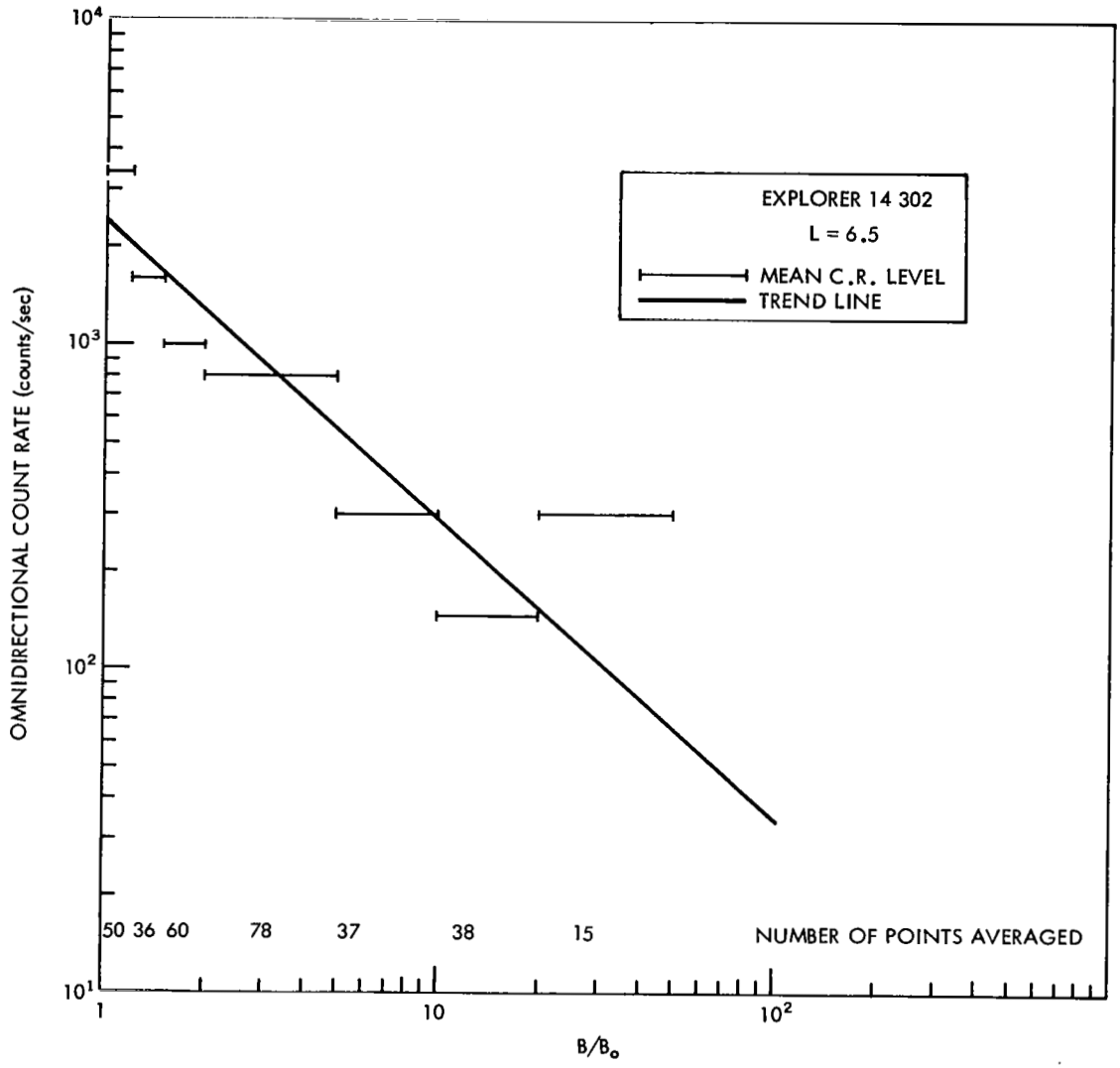

Figure 21. Analysis of B/B_0 Dependence of Omnidirectional Count Rate, Explorer 14 302 GM Counter Data at L = 6.5

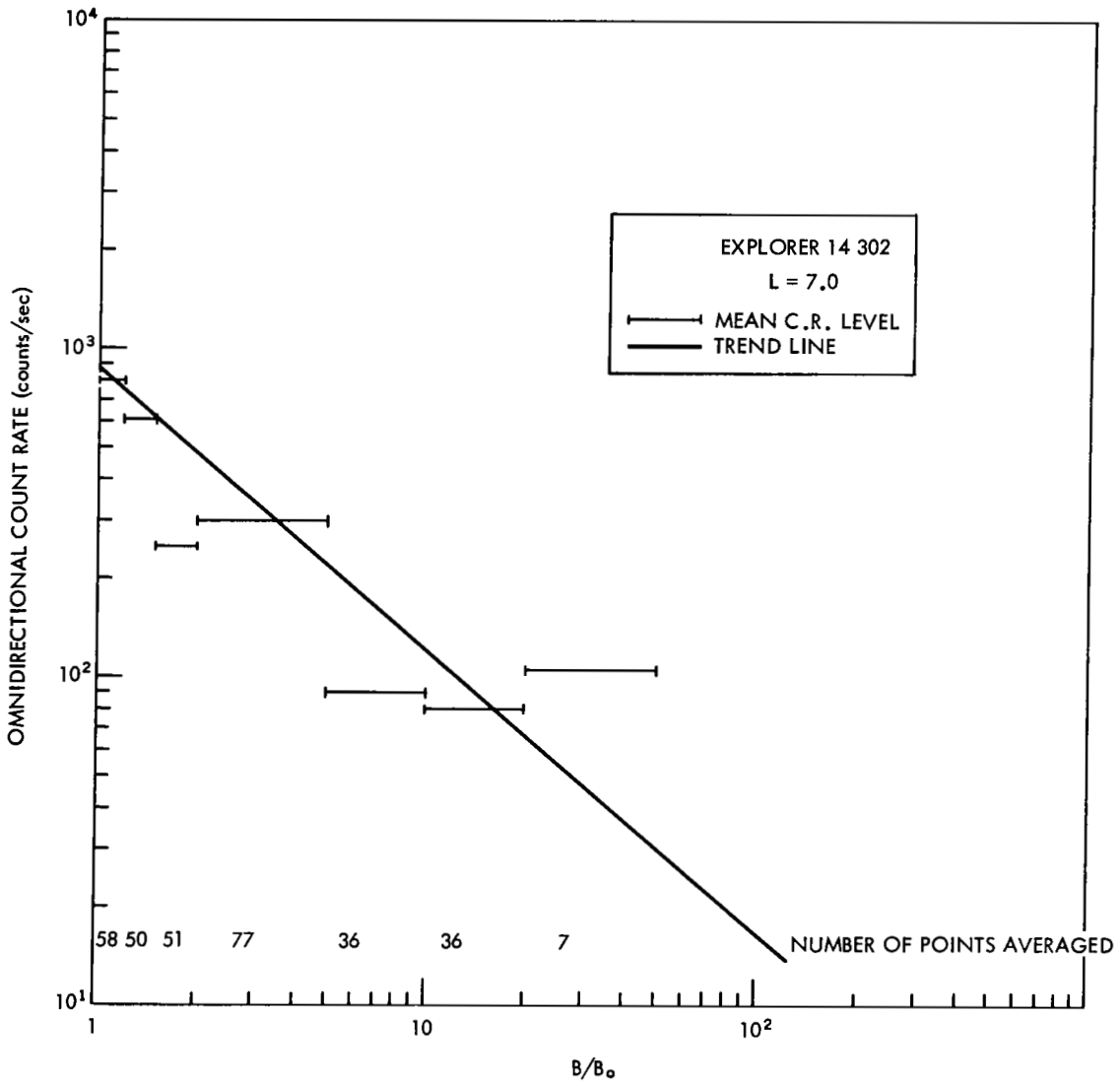

Figure 22. Analysis of B/B_0 Dependence of Omnidirectional Count Rate, Explorer 14 302 GM Counter Data at L = 7.0

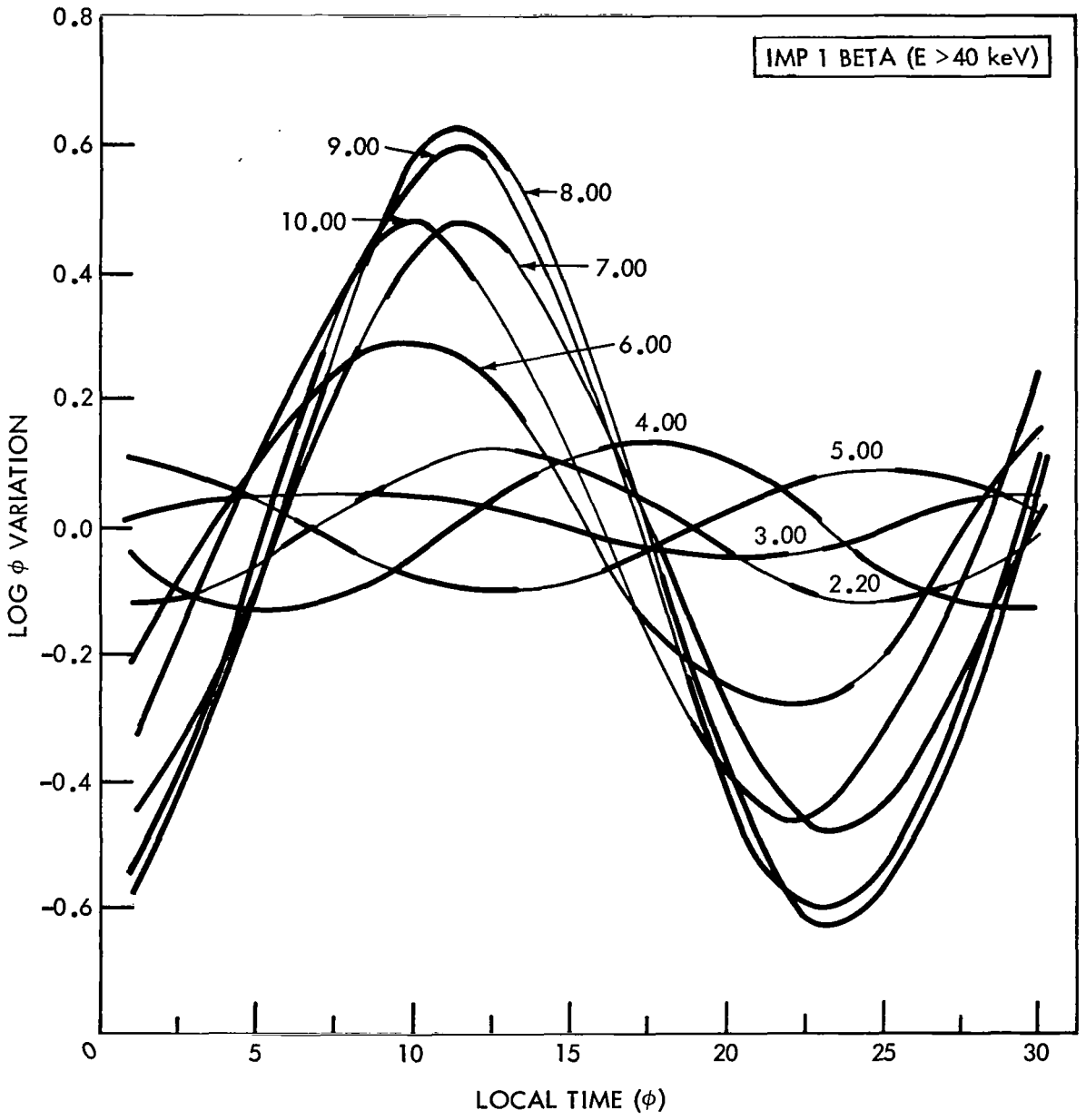

Figure 23. Local Time Variation at the Equator Showing Systematic Behavior Above L = 5; IMP 1, E > 40 keV

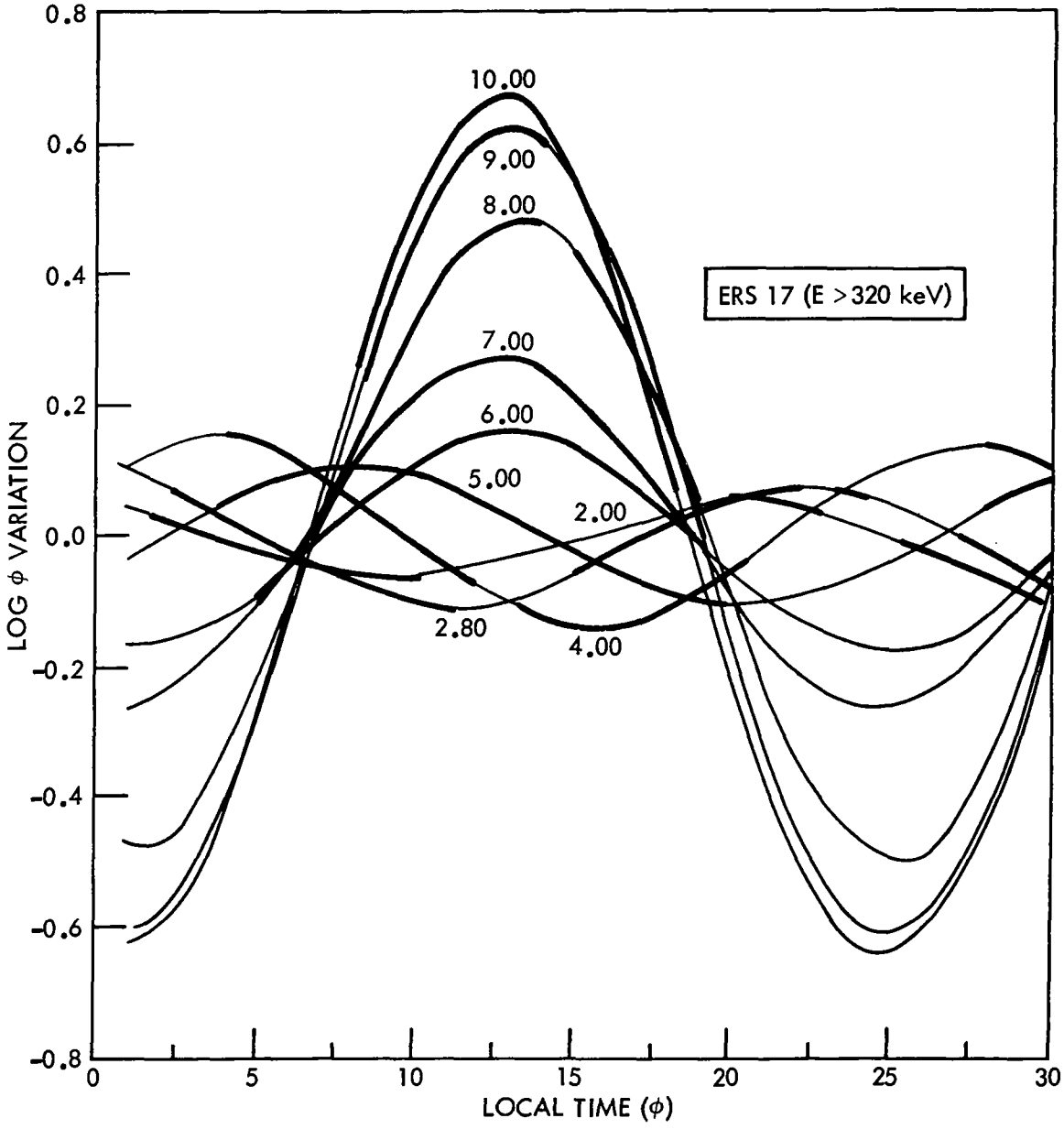

Figure 24. Local Time Variation at the Equator
Showing Systematic Behavior Above L = 5;
ERS 17, E > 320 keV

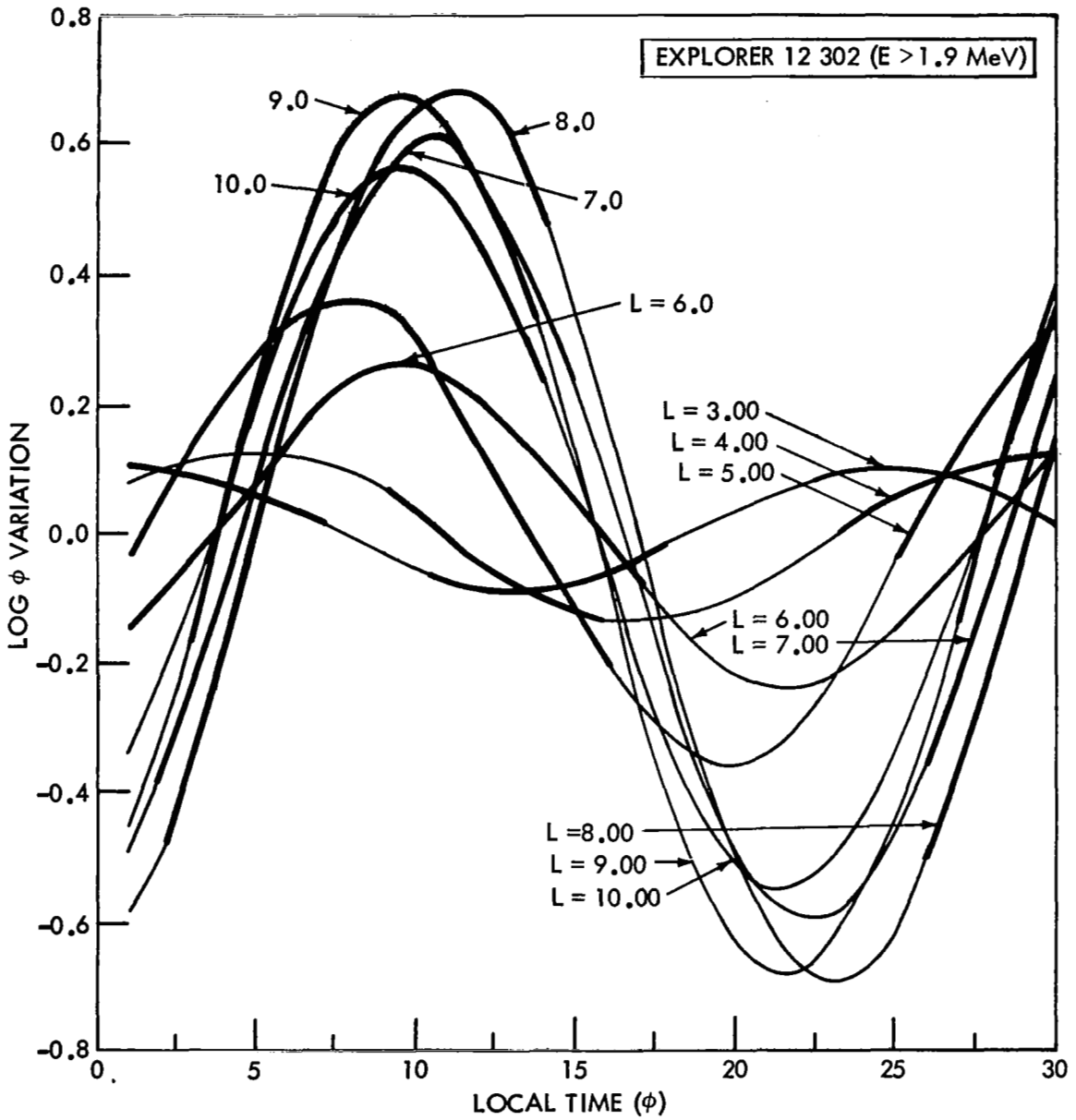

Figure 25. Local Time Variation at the Equator Showing Systematic Behavior Above L = 5; Explorer 12, E > 1.9 MeV

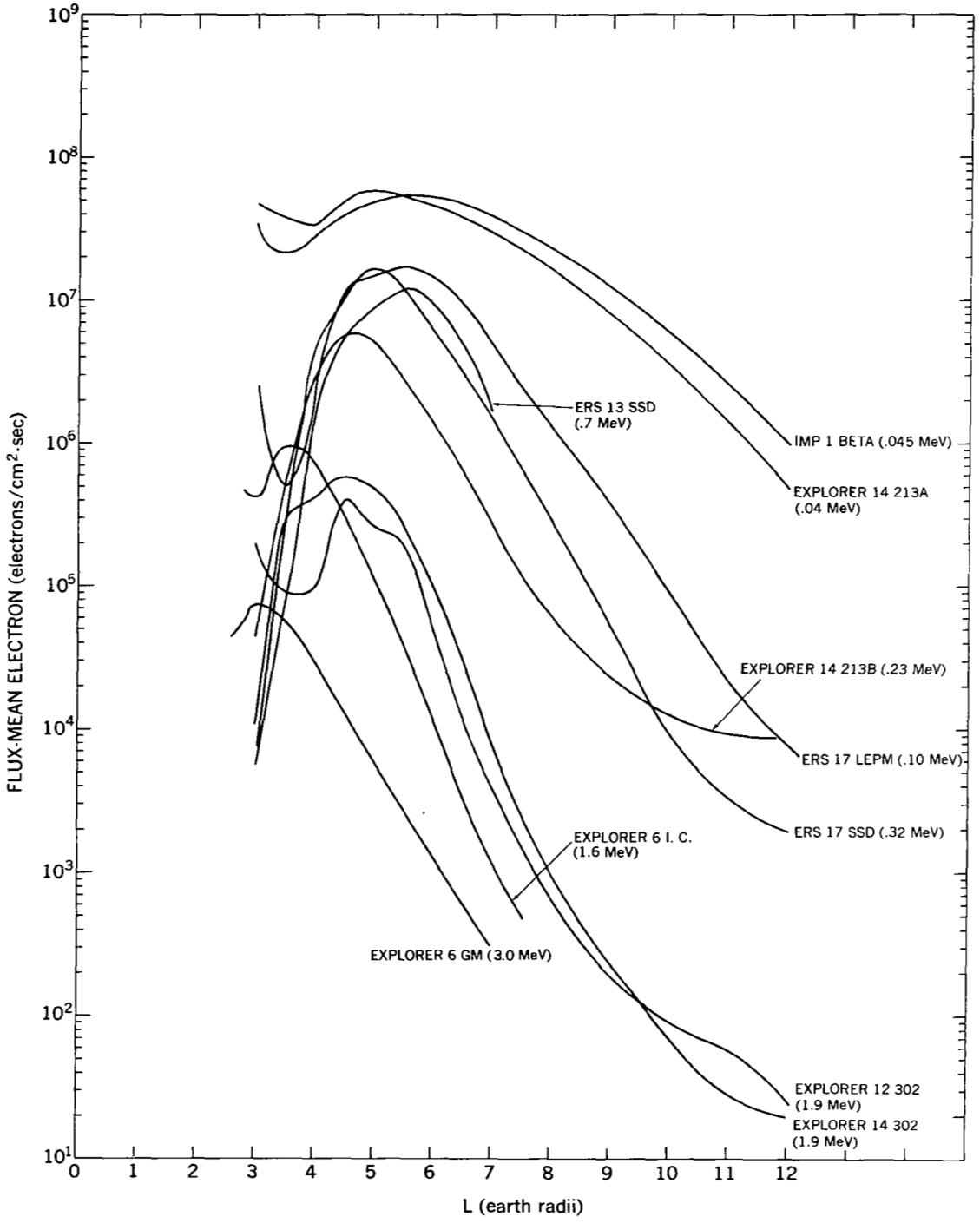

Figure 26. Equatorial Radial Profiles Obtained from Averages of Data Taken Near the Equator

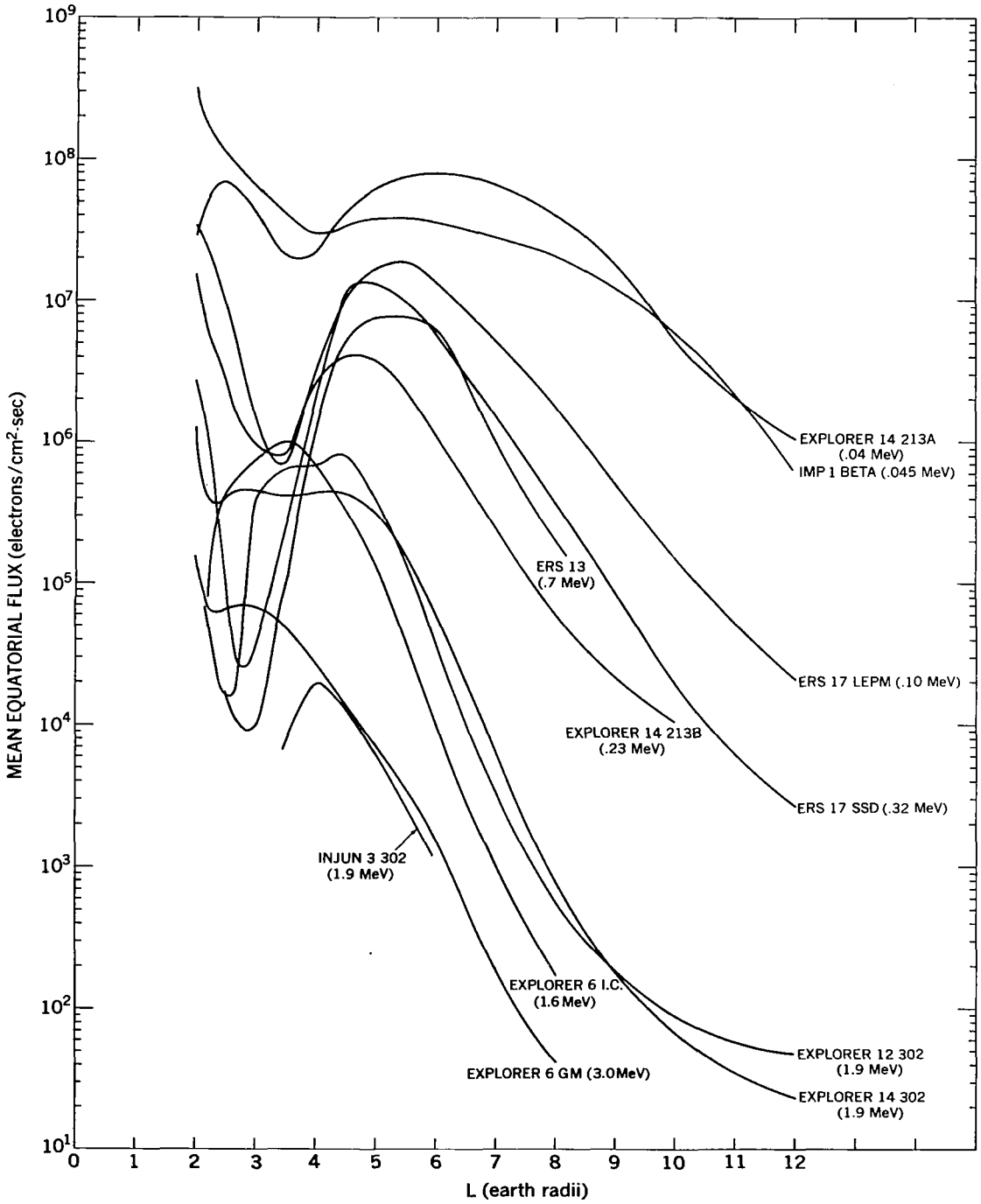

Figure 27. Equatorial Radial Profiles Obtained from the Equatorial Intersection of B/B_0 Trend Lines (see Figures 23, 24, and 25)

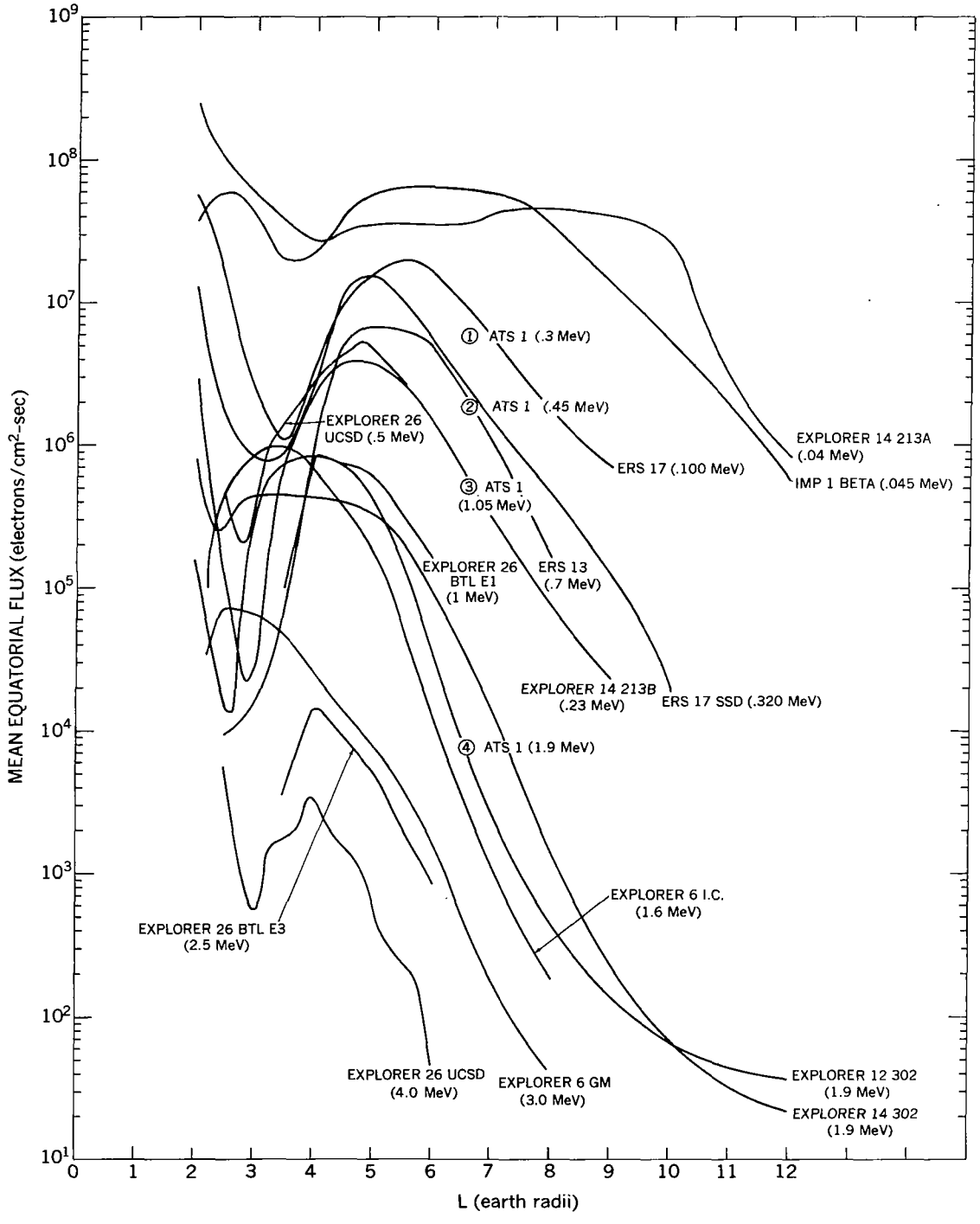

Figure 28. Equatorial Radial Profiles Obtained with Two-Dimensional Fits to Flux Data as a Function of Local Time and Magnetic Field

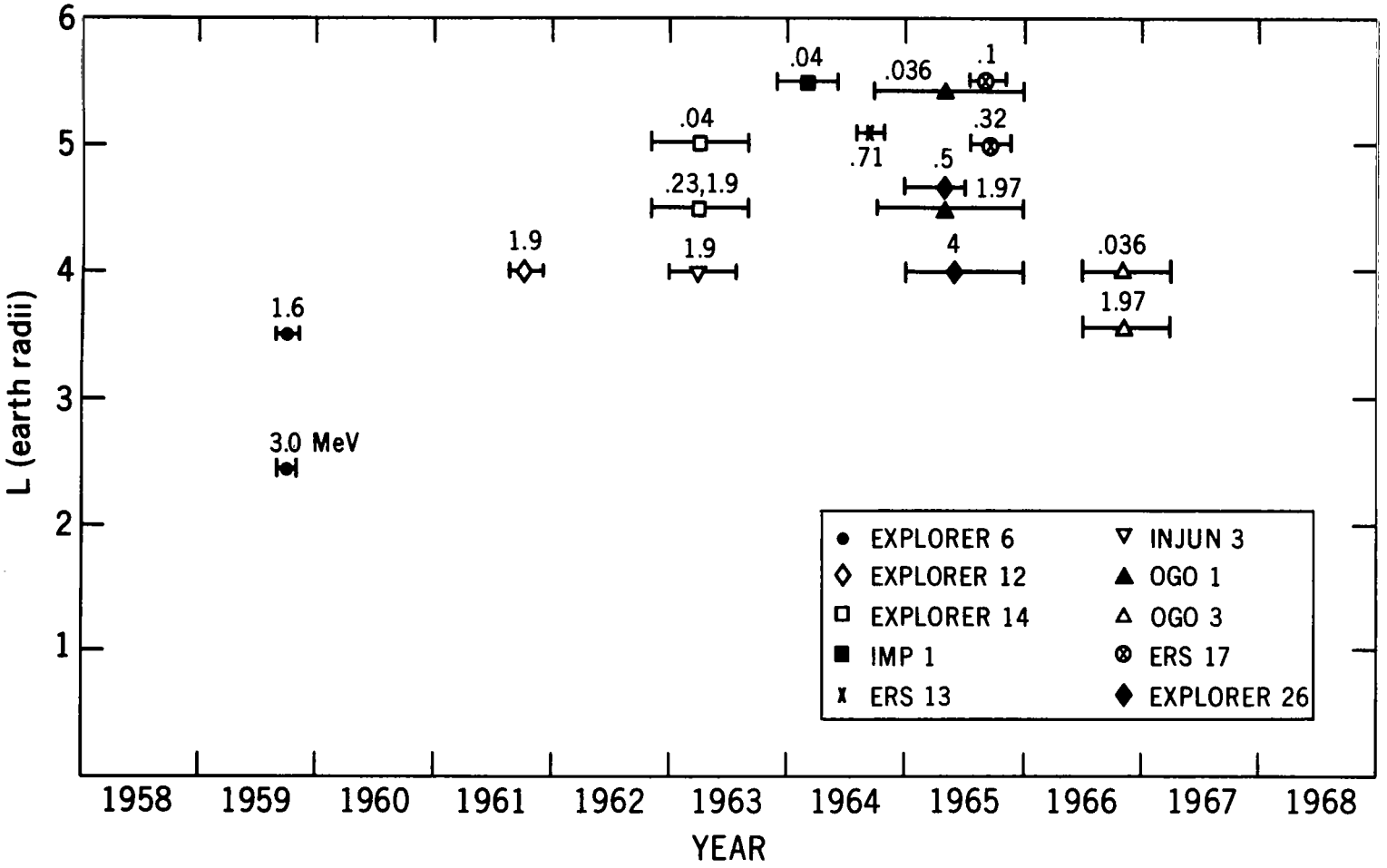

Figure 29. L Position of Outer Zone Maximum as a Function of Time

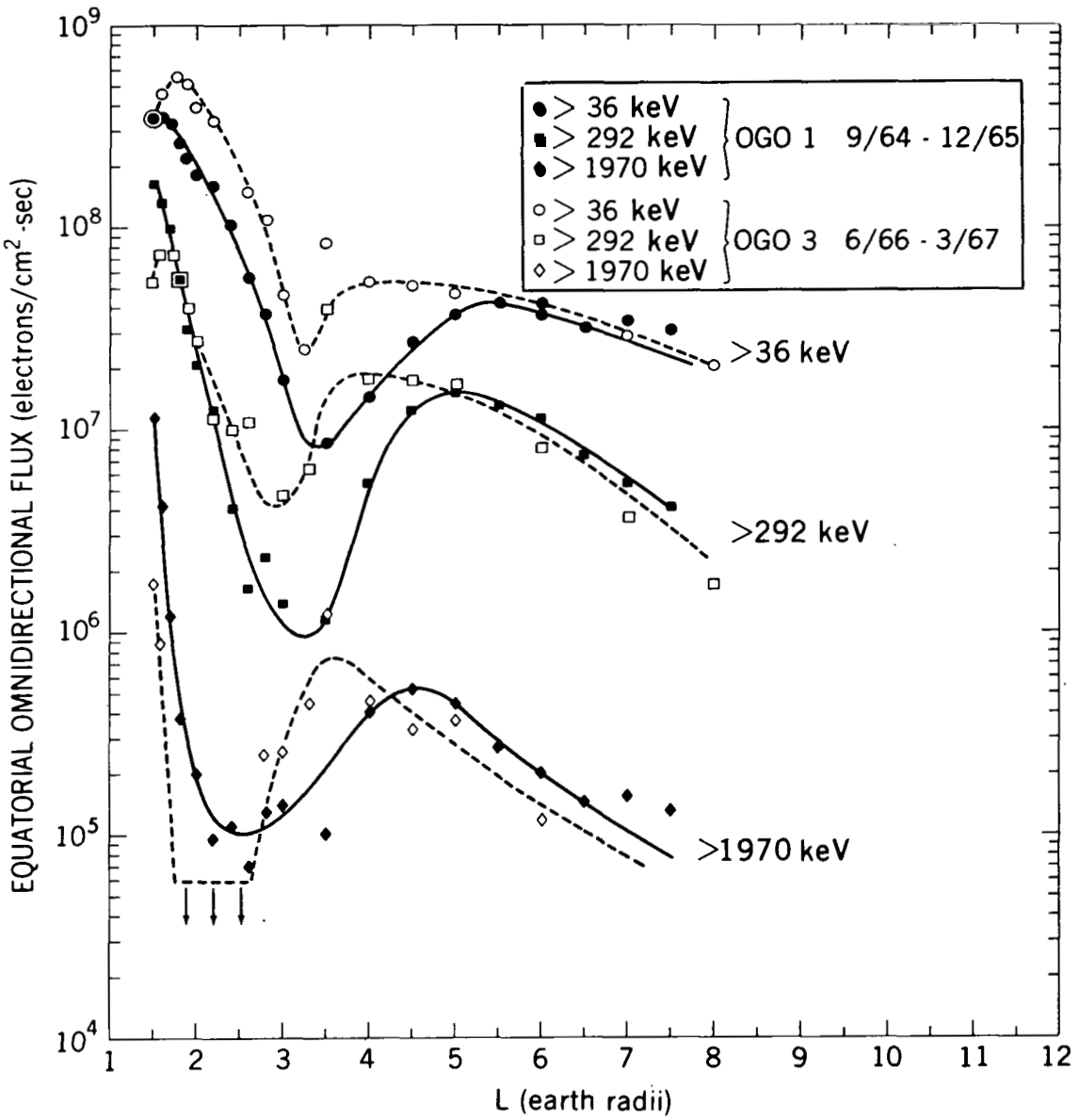

Figure 30. Equatorial Radial Profiles Obtained from OGO Data, Showing Solar Cycle Effects

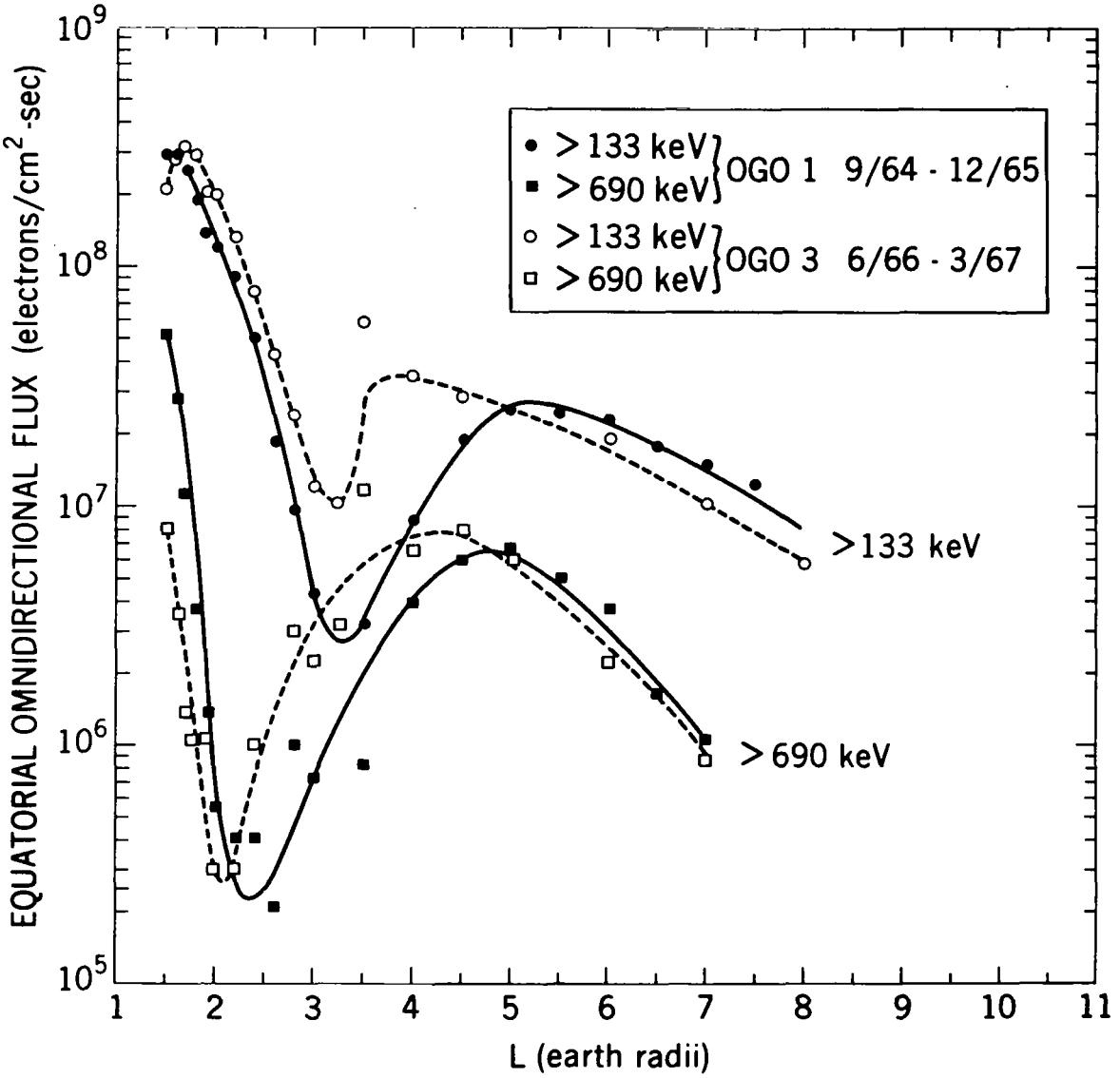

Figure 31. Equatorial Radial Profiles Obtained from OGO Data, Showing Solar Cycle Effects

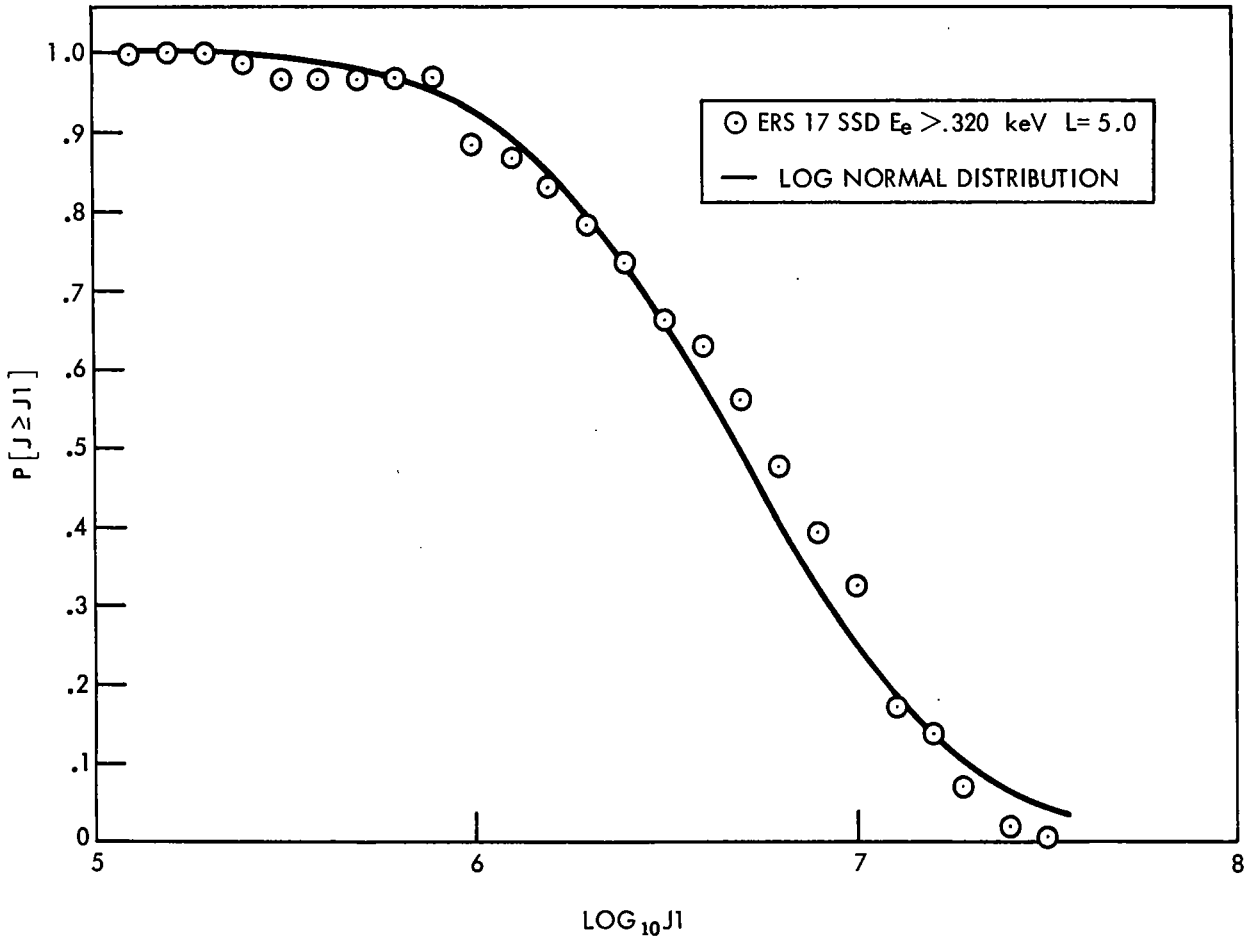

Figure 32. Comparison of Log Normal Distribution and Data from ERS 13, L = 5.0, E_e > 320 keV

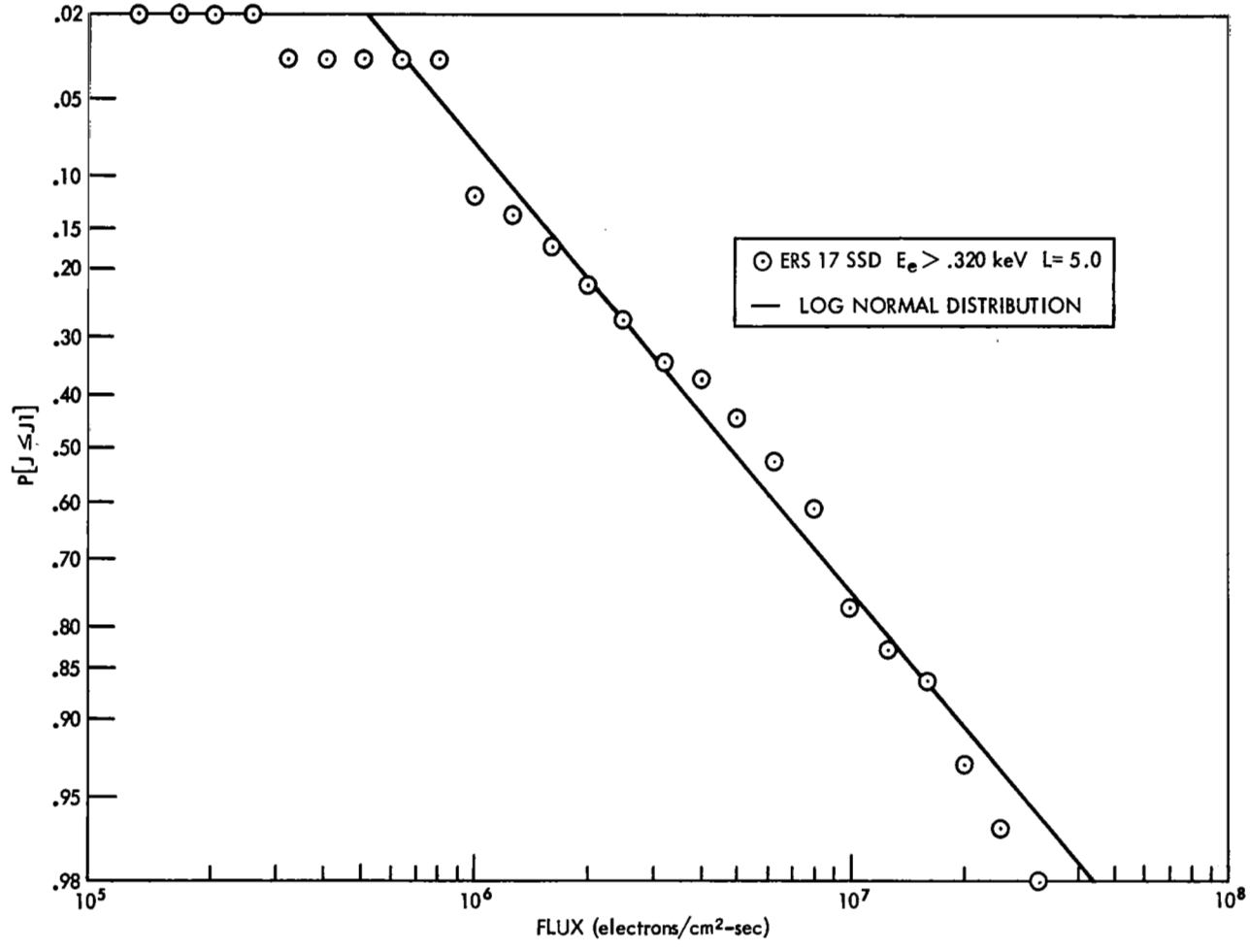

Figure 33. Comparison of Log Normal Distribution and Data from ERS 13, L = 5.0, E_e > 320 keV

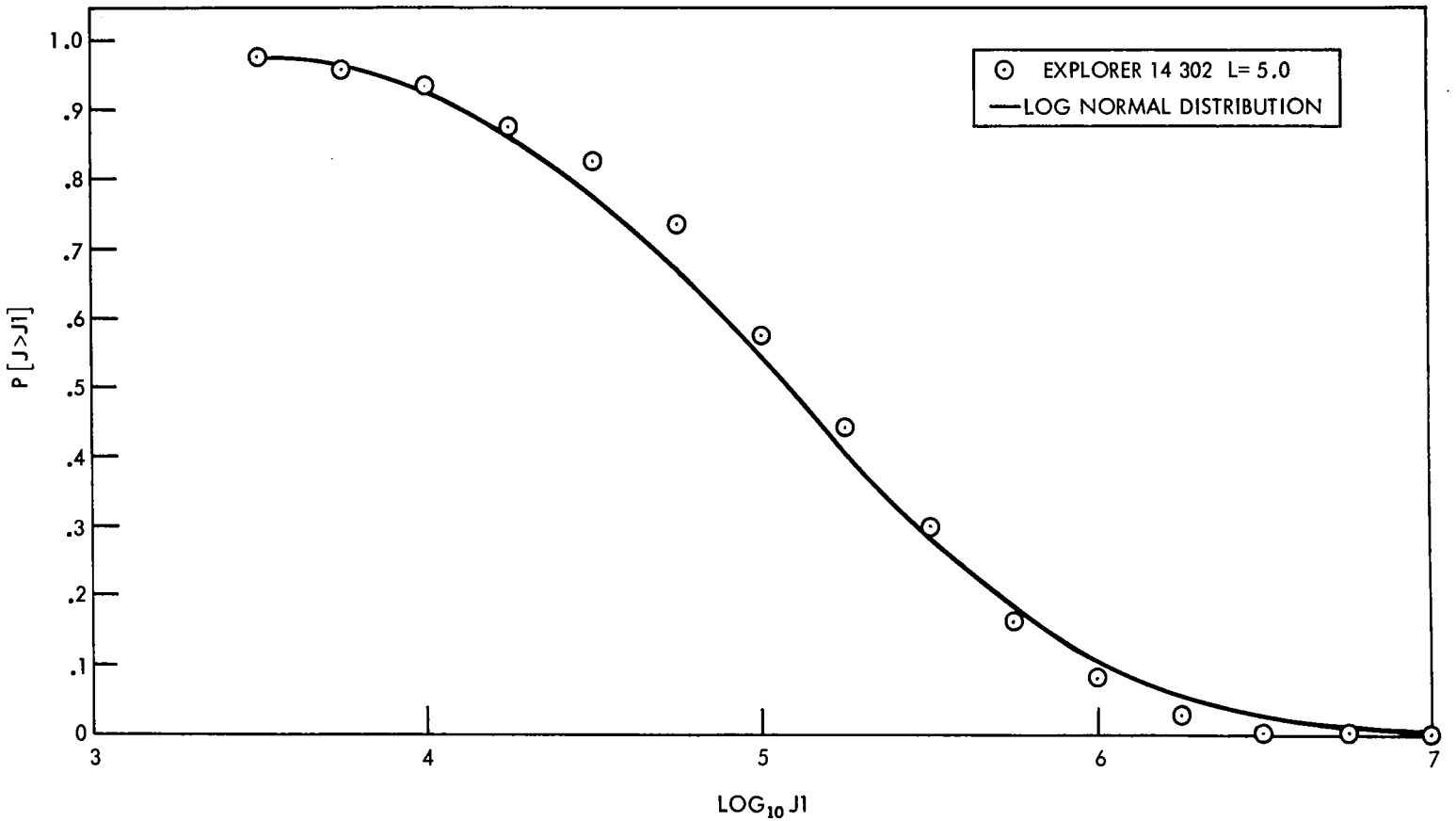

Figure 34. Comparison of Log Normal Distribution and Data from Explorer 14, $L = 5.0$, $E_e > 1.9$ MeV

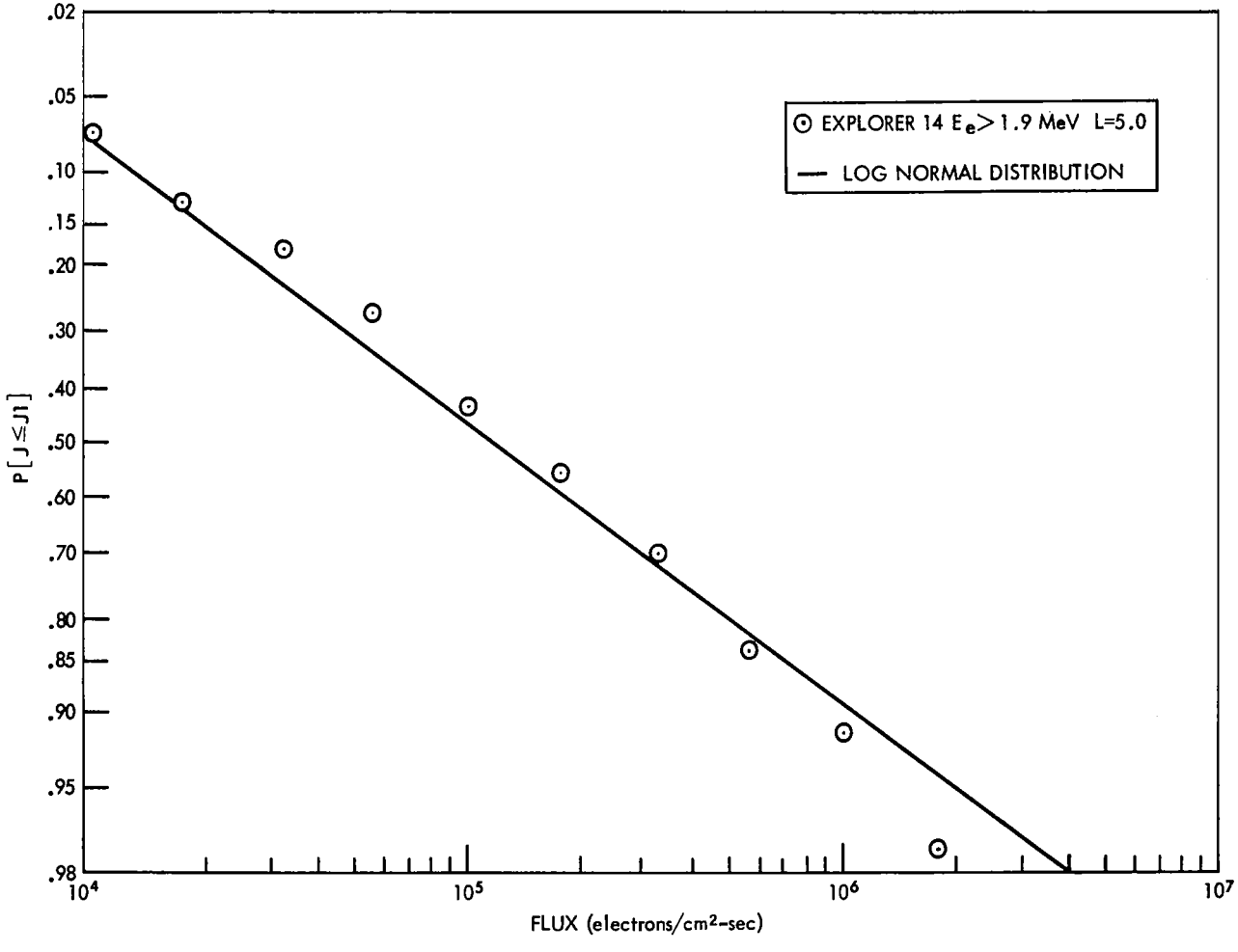

Figure 35. Comparison of Log Normal Distribution and Data from Explorer 14, L = 5.0, E_e > 1.9 MeV

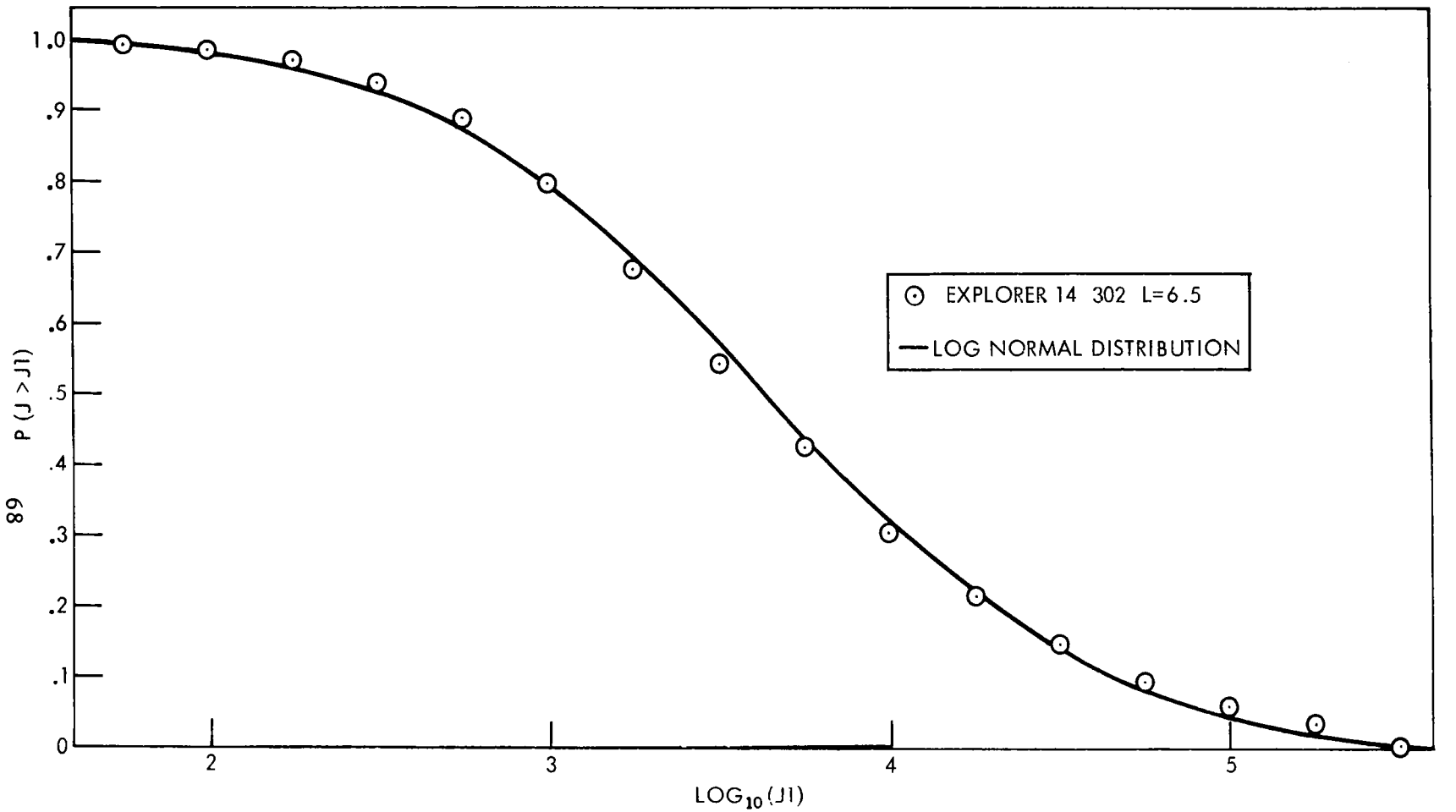

Figure 36. Comparison of Log Normal Distribution and Data from Explorer 14, $L = 6.5$, $E_e > 1.9$ MeV

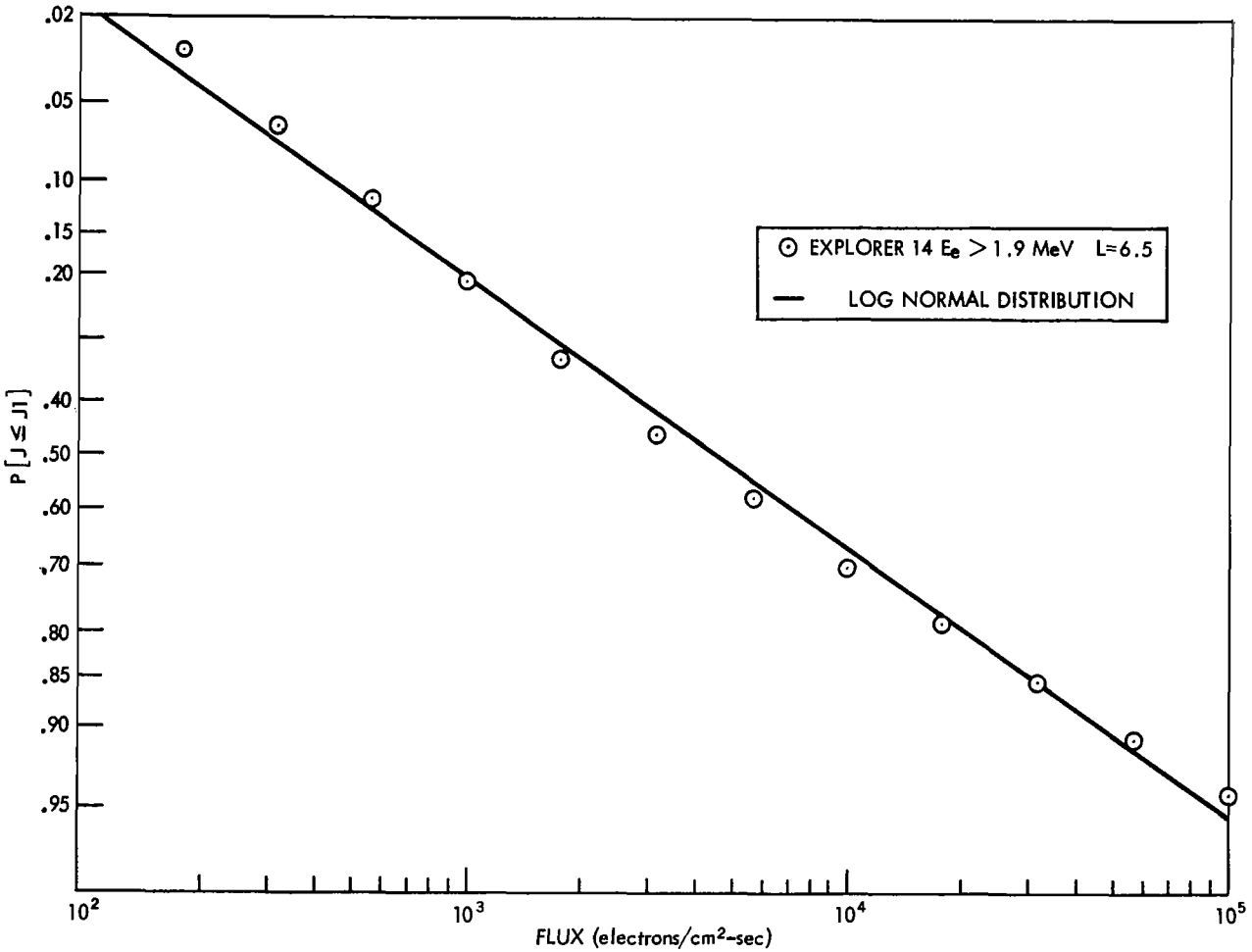

Figure 37. Comparison of Log Normal Distribution and Data from Explorer 14, L = 6.5, E_e > 1.9 MeV

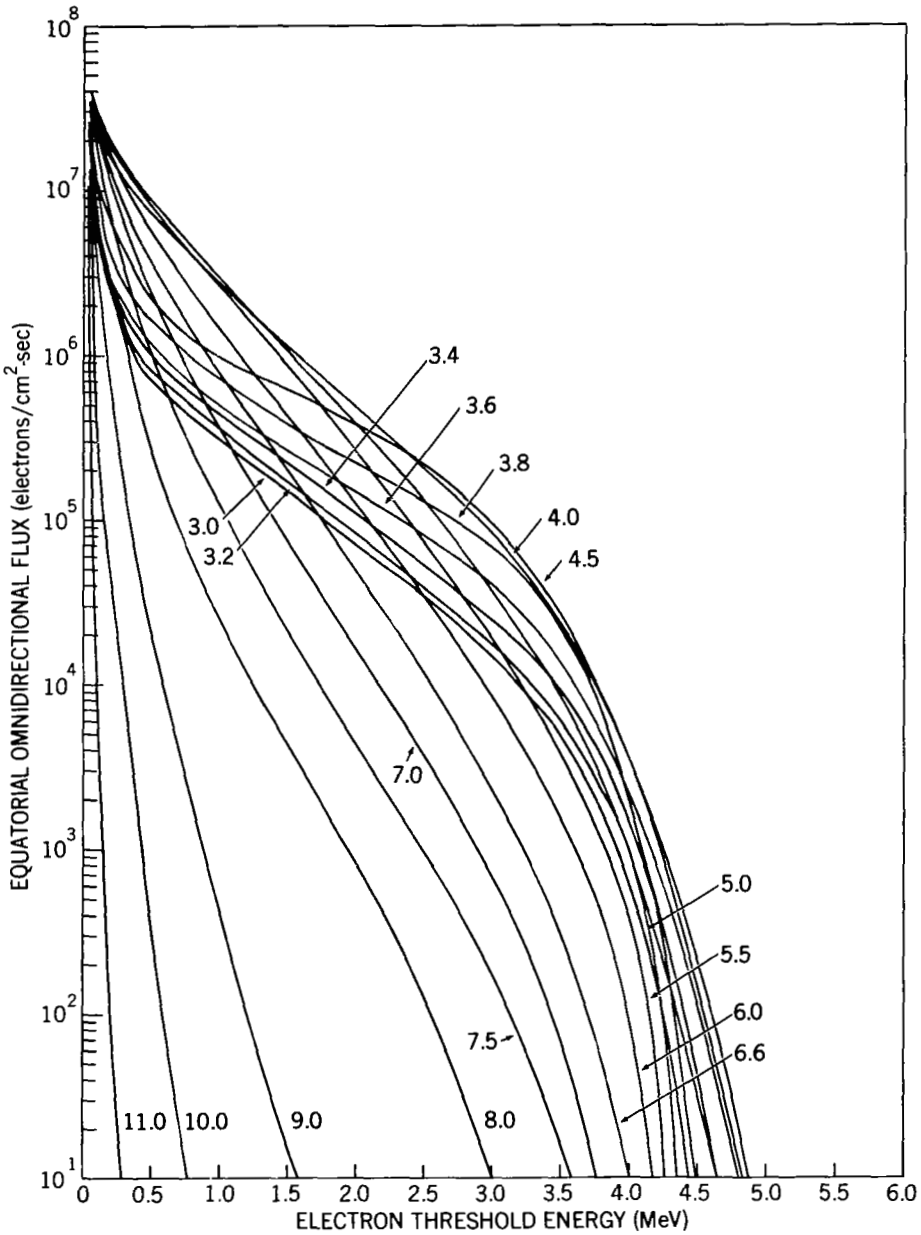

Figure 38. AE-4 Integral Electron Spectra for Various L Values, Epoch 1964

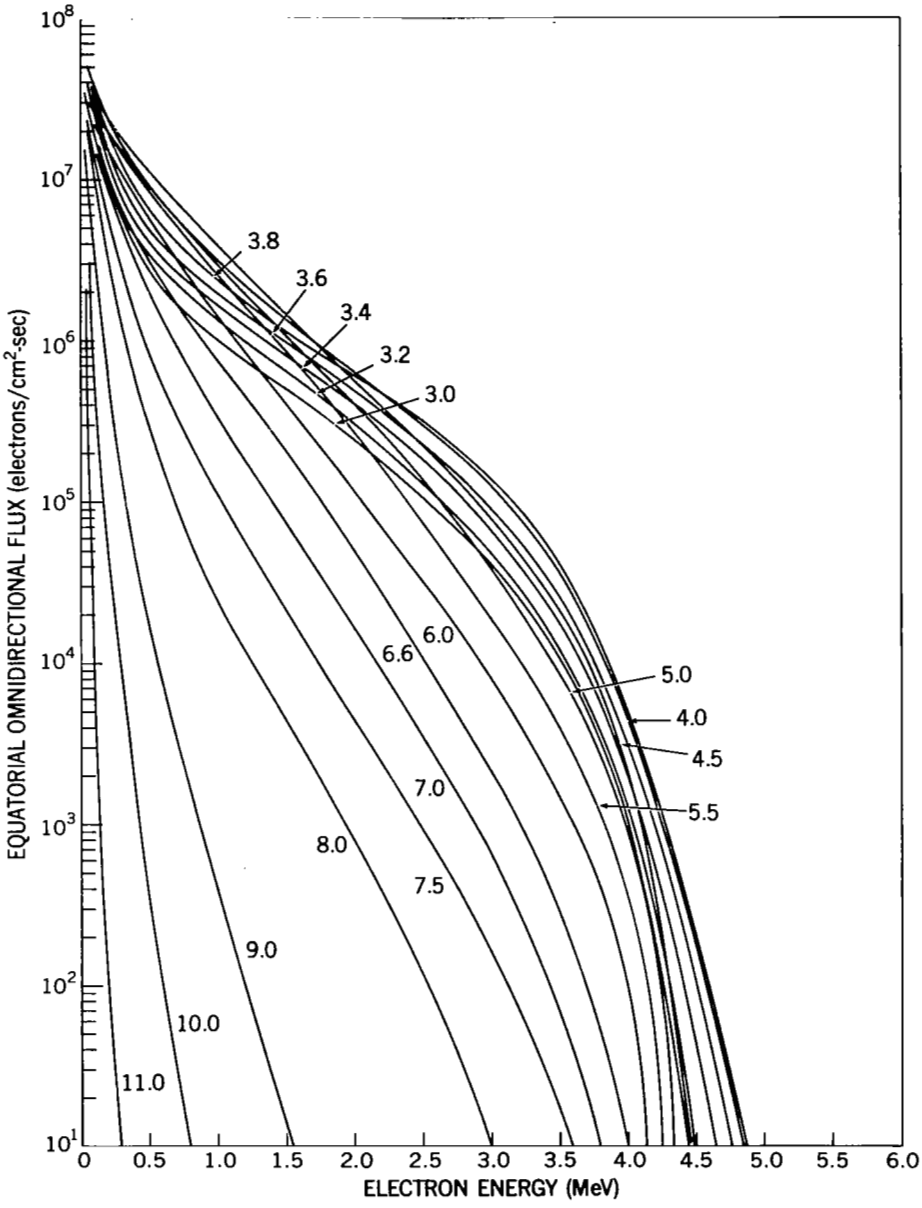

Figure 39. AE-4 Integral Electron Spectra for Various L Values, Epoch 1967

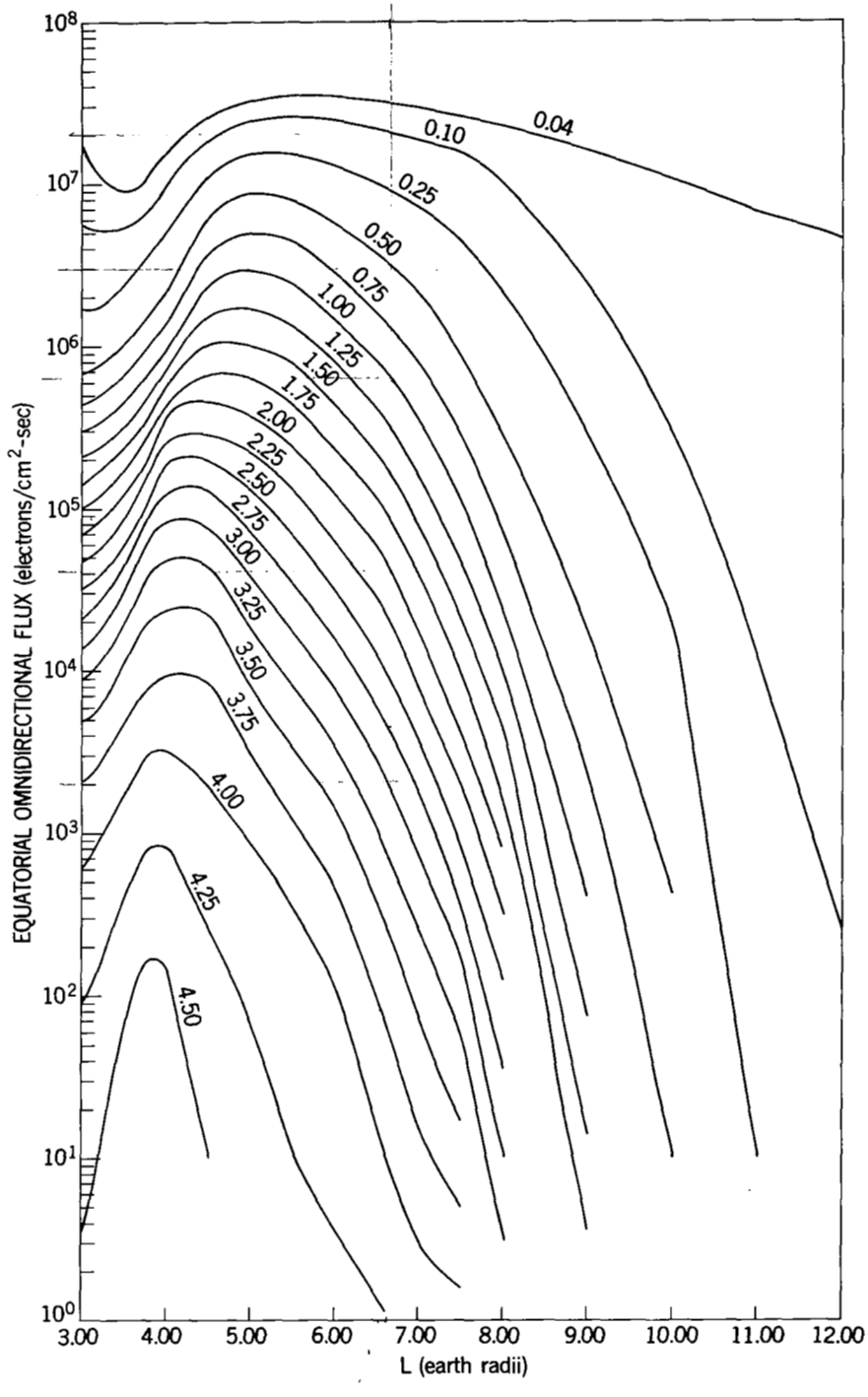

Figure 40. AE-4 Radial Profile of Equatorial Omnidirectional Flux for Various Energy Thresholds, Epoch 1964

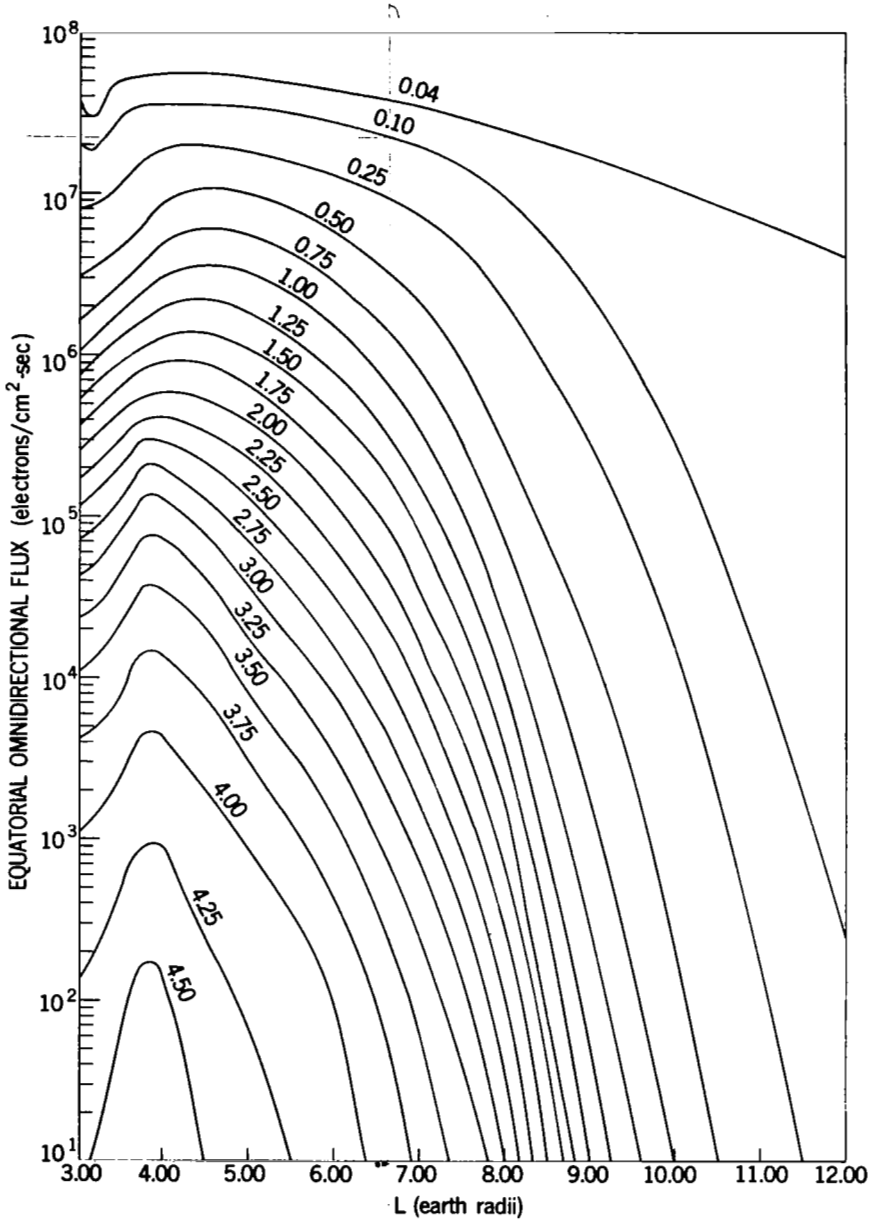

Figure 41. AE-4 Radial Profile of Equatorial Omnidirectional Flux for Various Energy Thresholds, Epoch 1967

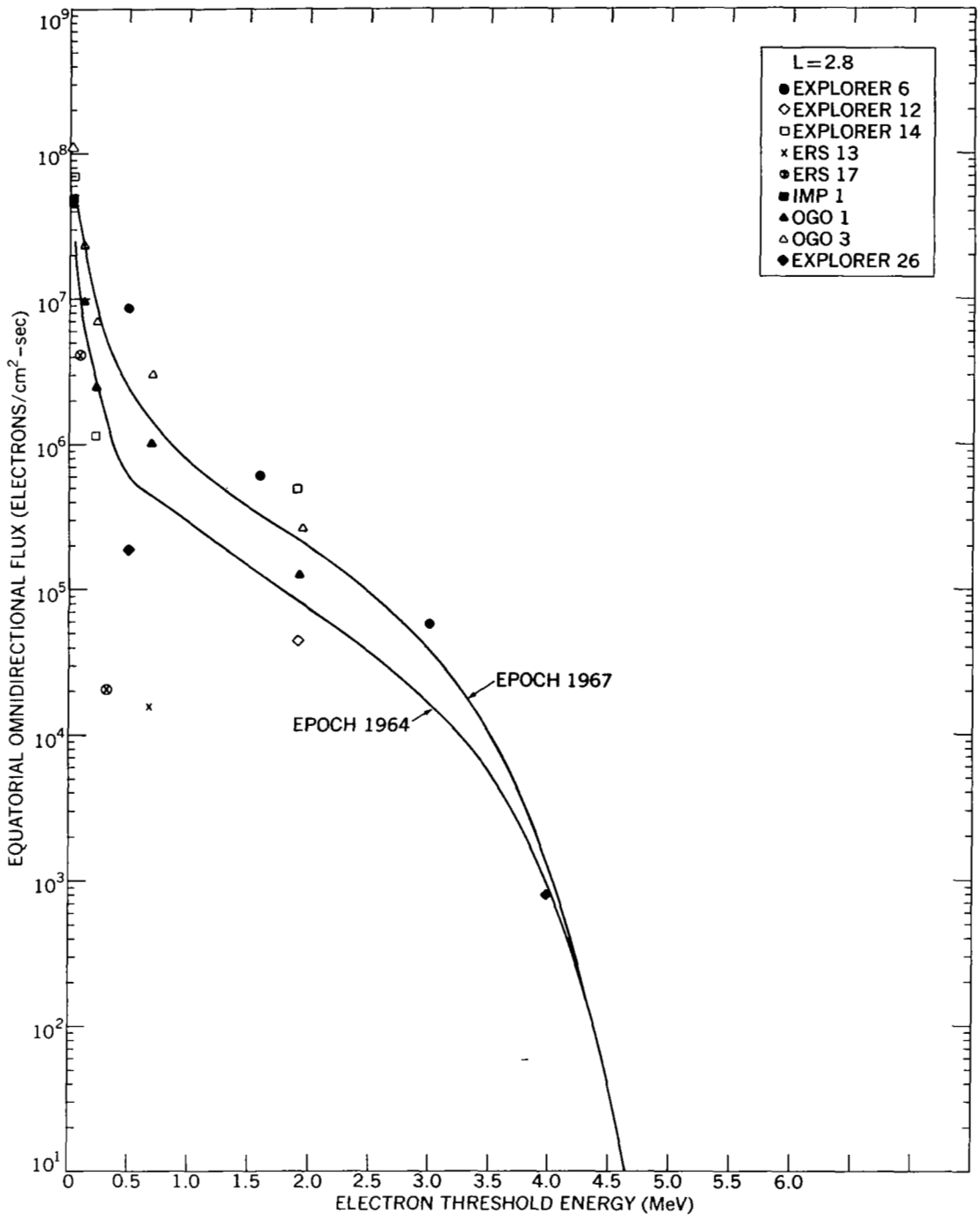

Figure 42. Comparison of AE-4 Model Spectrum with Data at L = 2.8

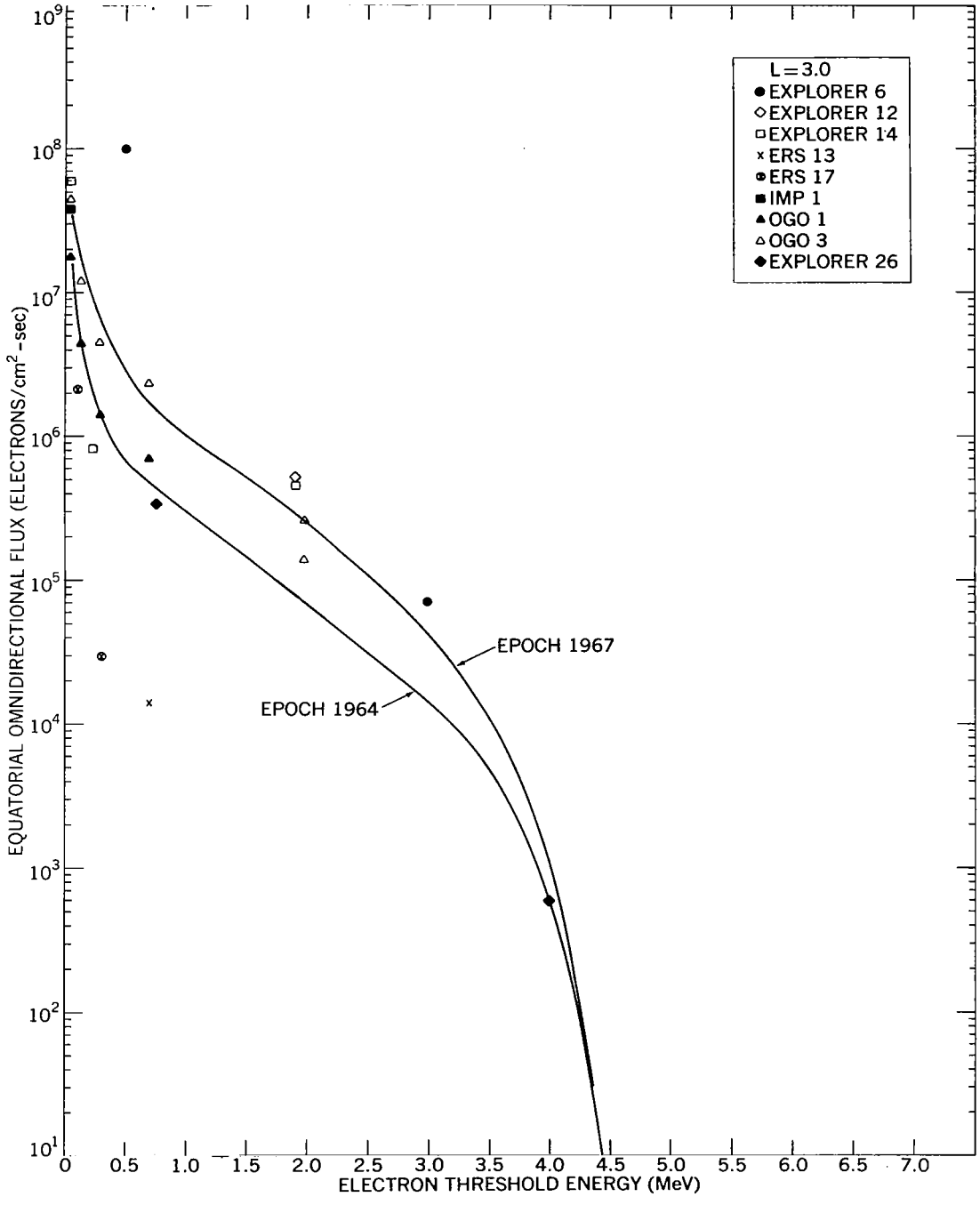

Figure 43. Comparison of AE-4 Model Spectrum with Data at L = 3.0

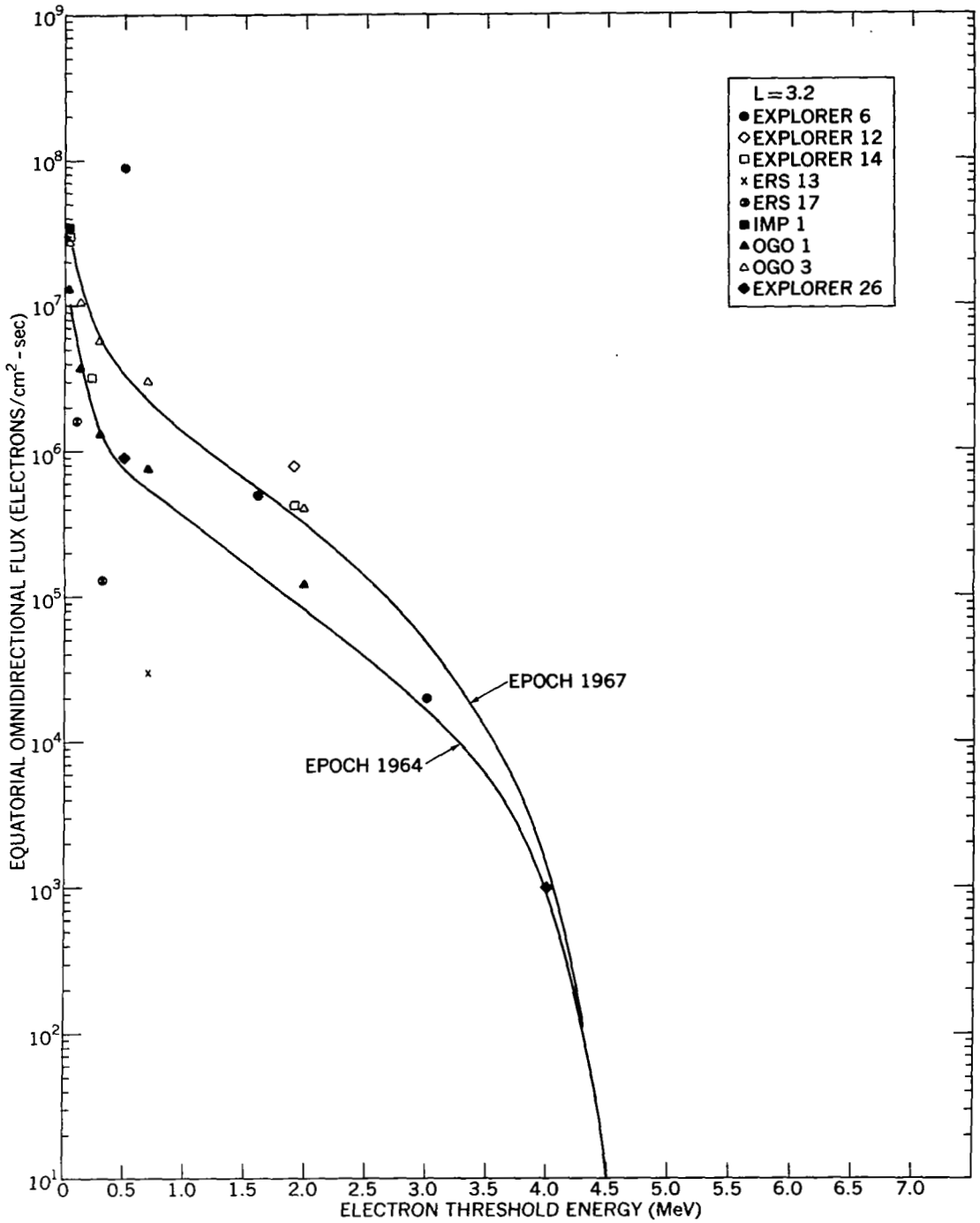

Figure 44. Comparison of AE-4 Model Spectrum with Data at L = 3.2

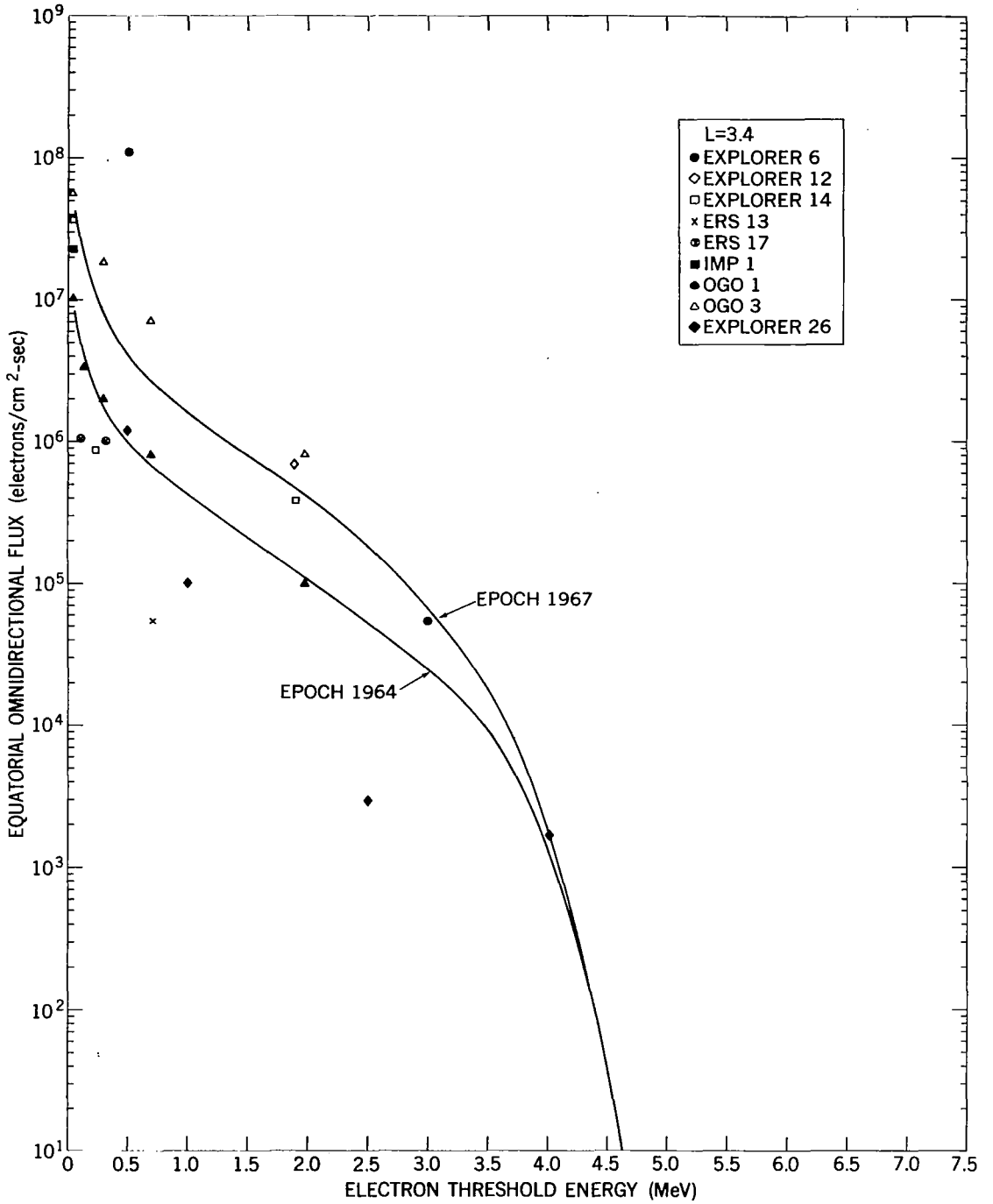

Figure 45. Comparison of AE-4 Model Spectrum with Data at L = 3.4

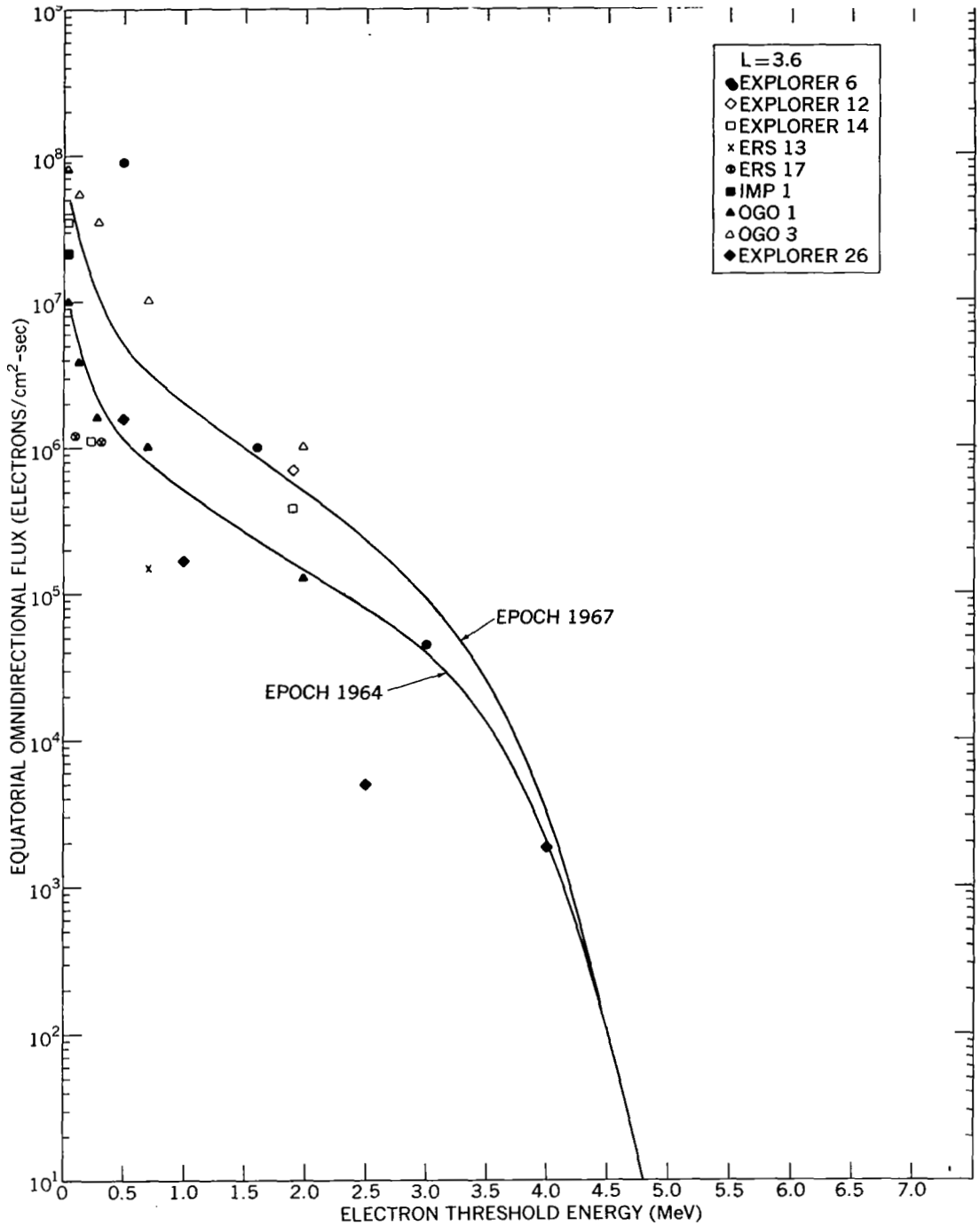

Figure 46. Comparison of AE-4 Model Spectrum with Data at L = 3.6

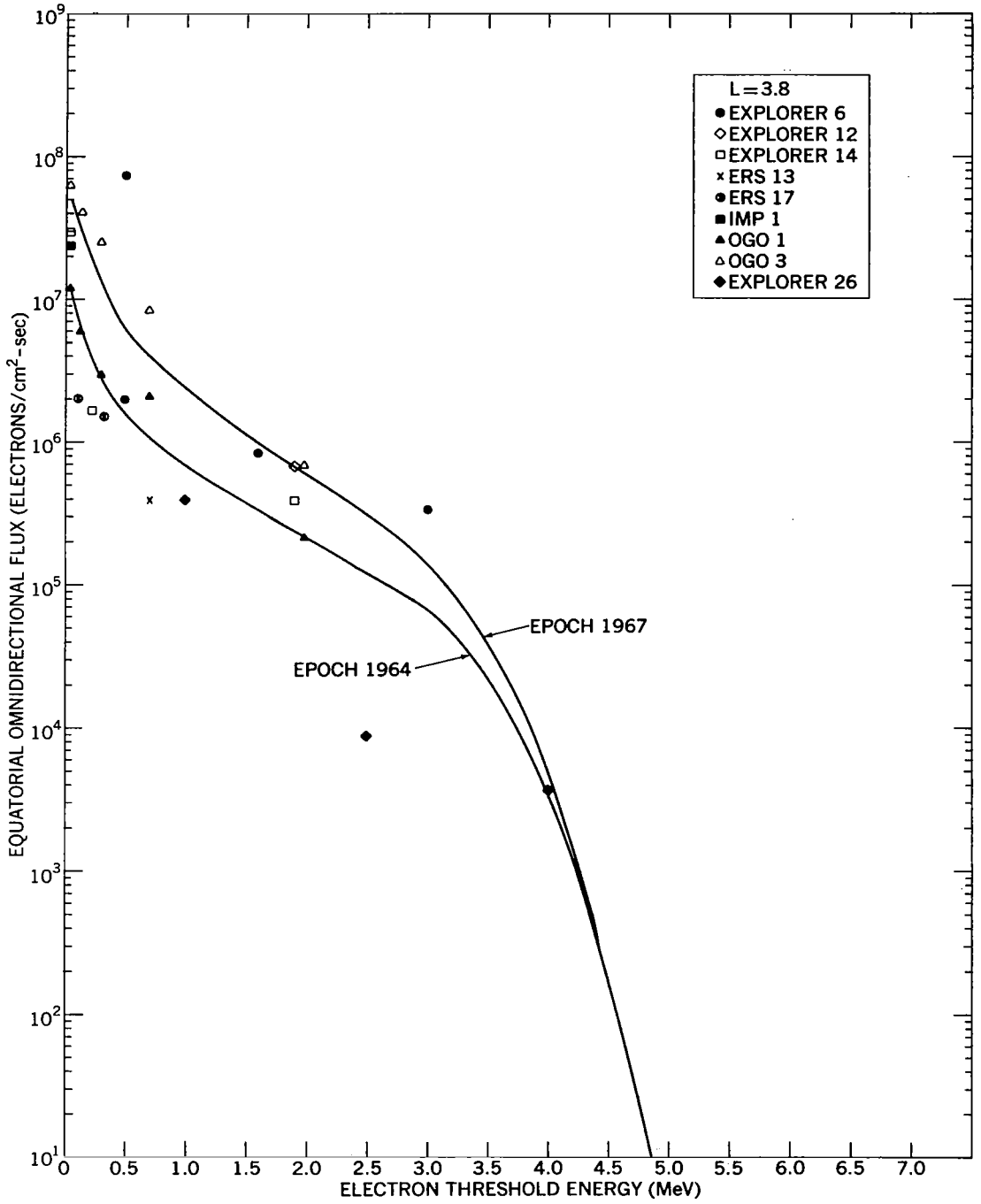

Figure 47. Comparison of AE-4 Model Spectrum with Data at L = 3.8

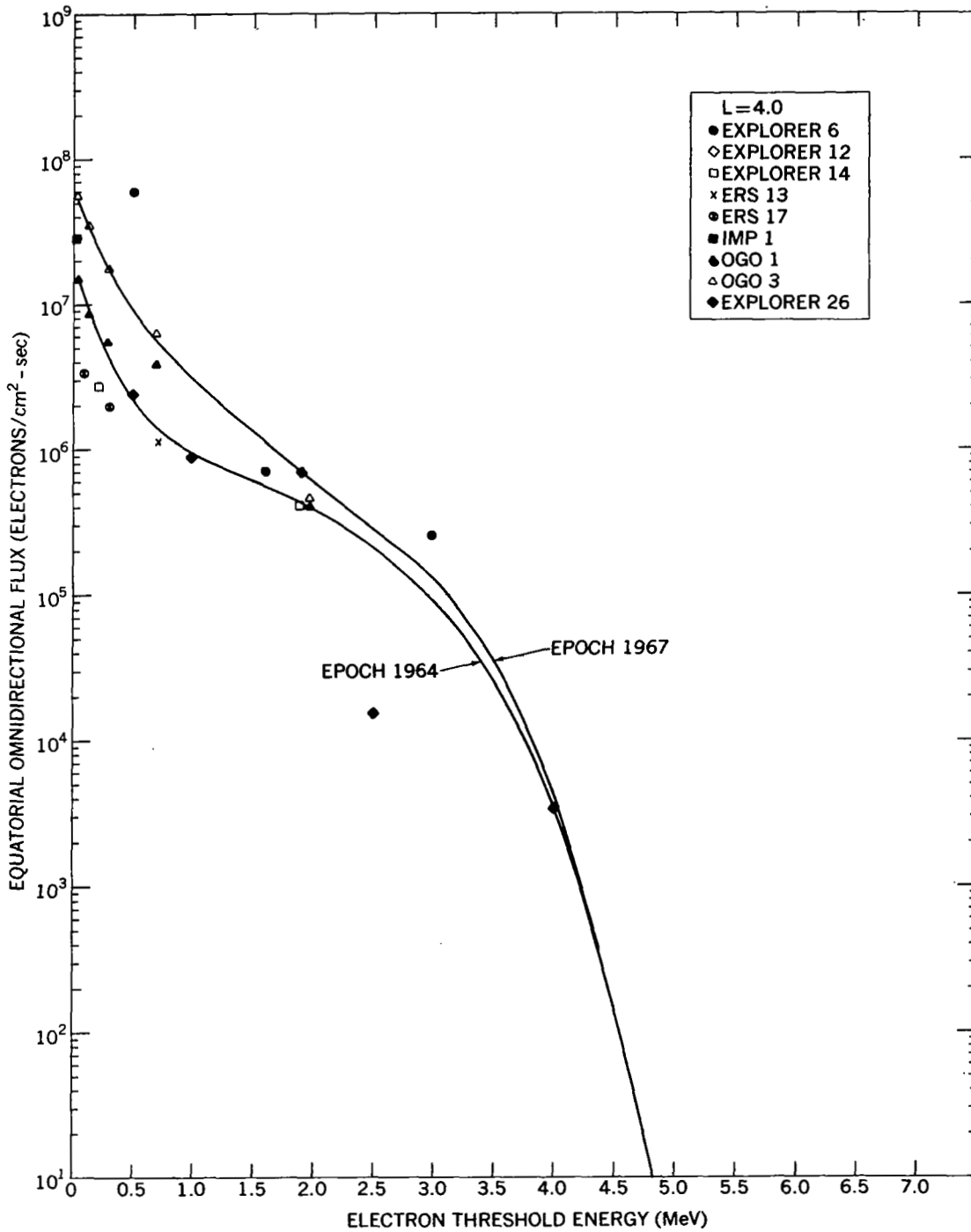

Figure 48. Comparison of AE-4 Model Spectrum with Data at L = 4.0

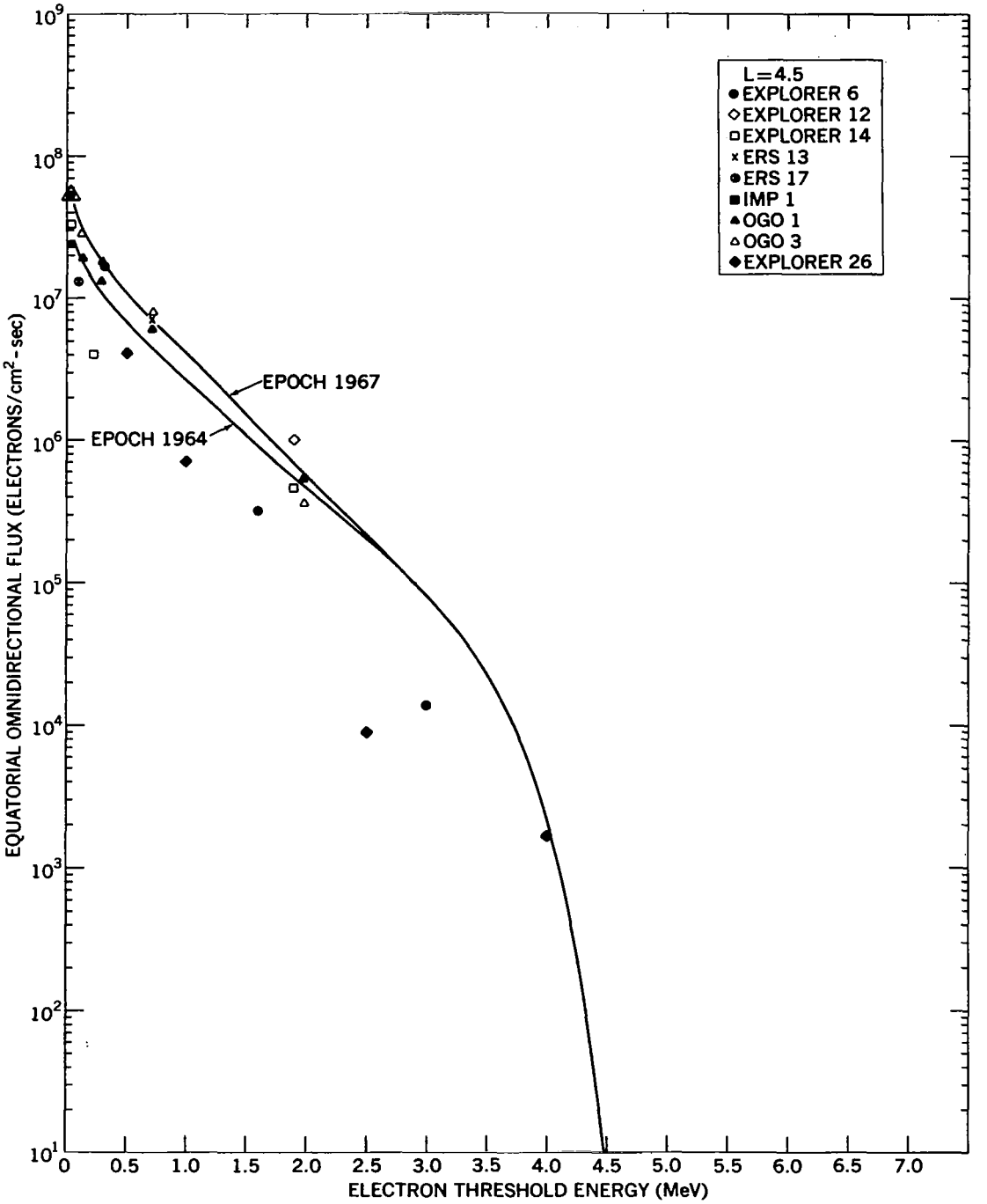

Figure 49. Comparison of AE-4 Model Spectrum with Data at L = 4.5

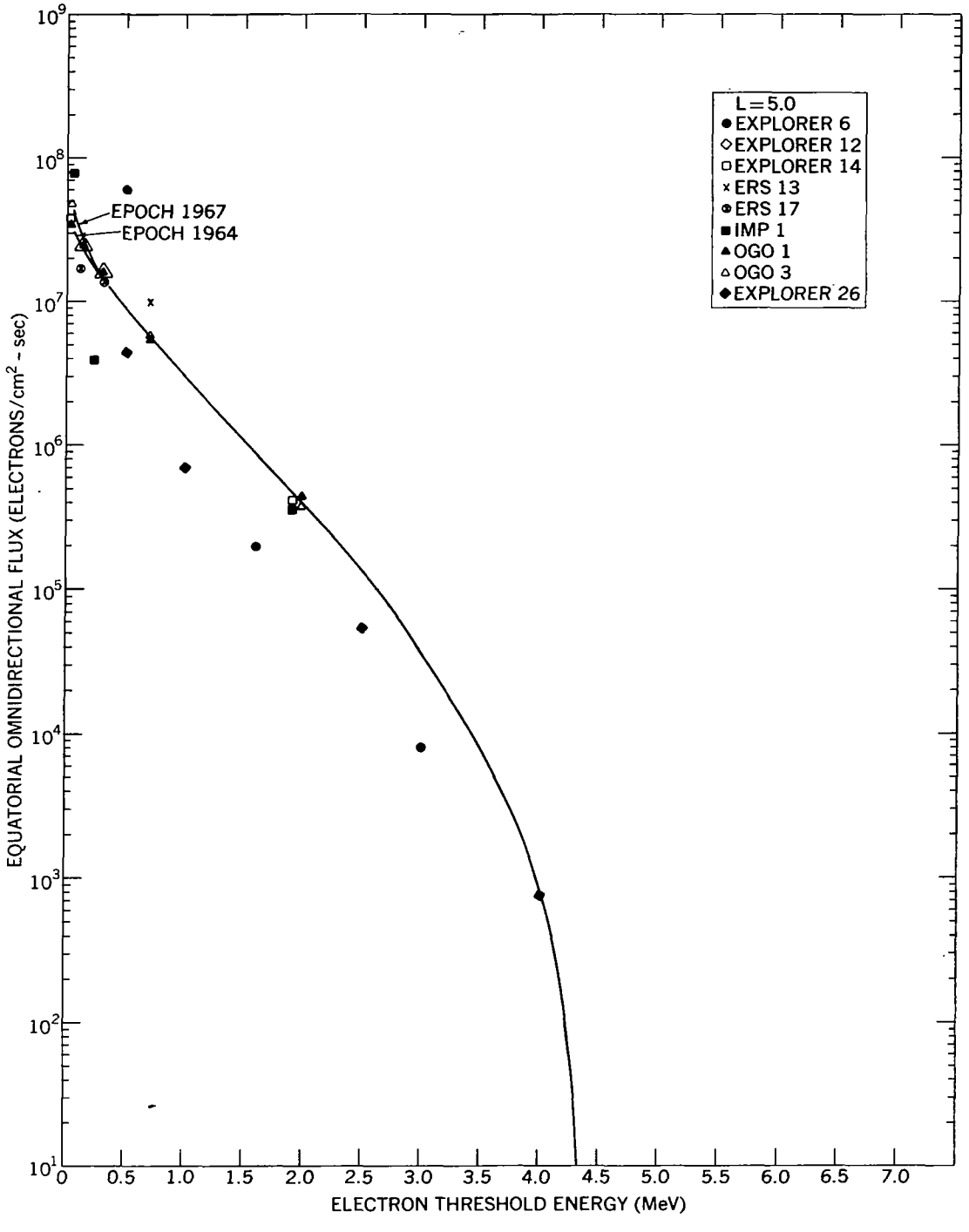

Figure 50. Comparison of AE-4 Model Spectrum with Data at L = 5.0

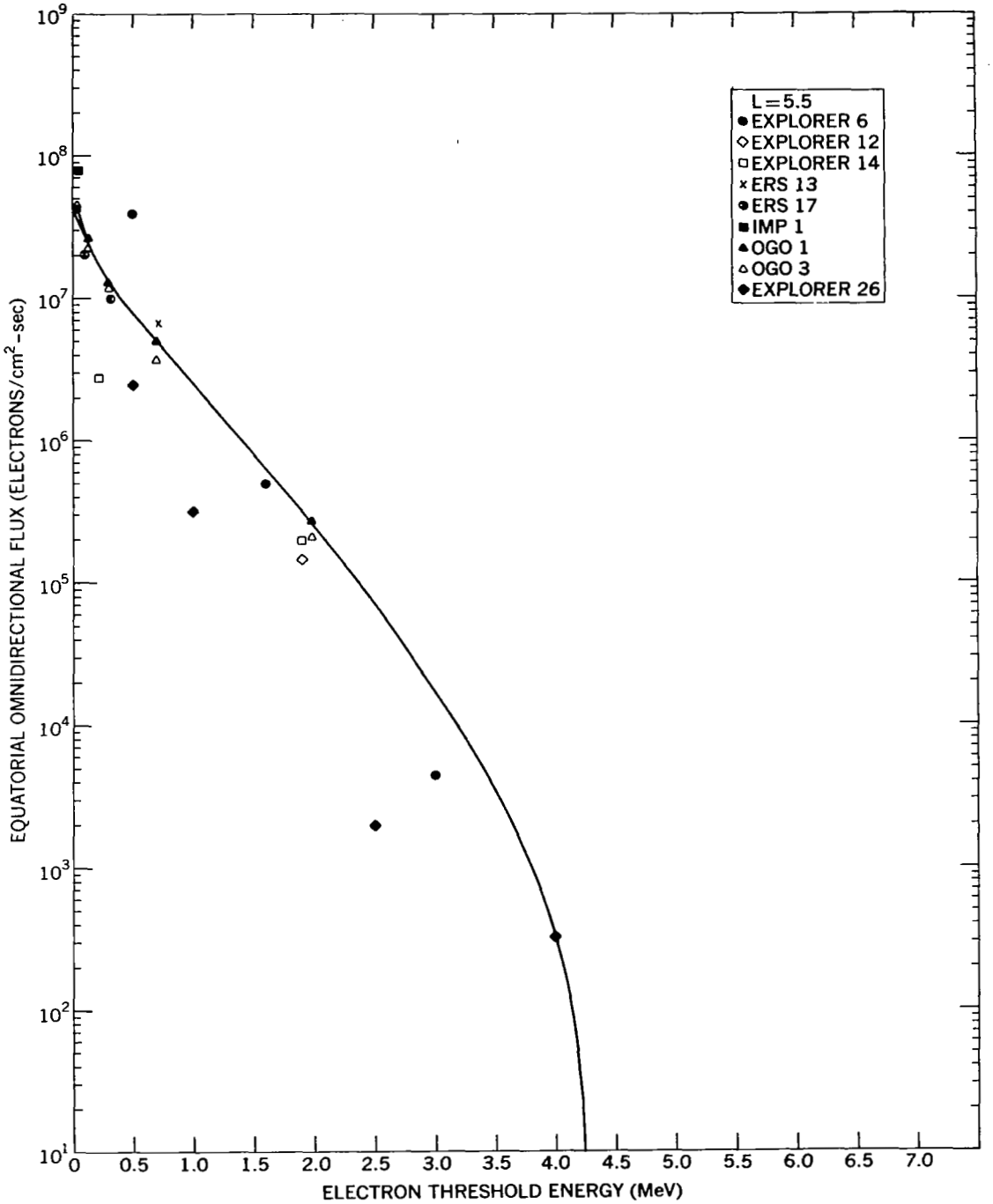

Figure 51. Comparison of AE-4 Model Spectrum with Data at L = 5.5

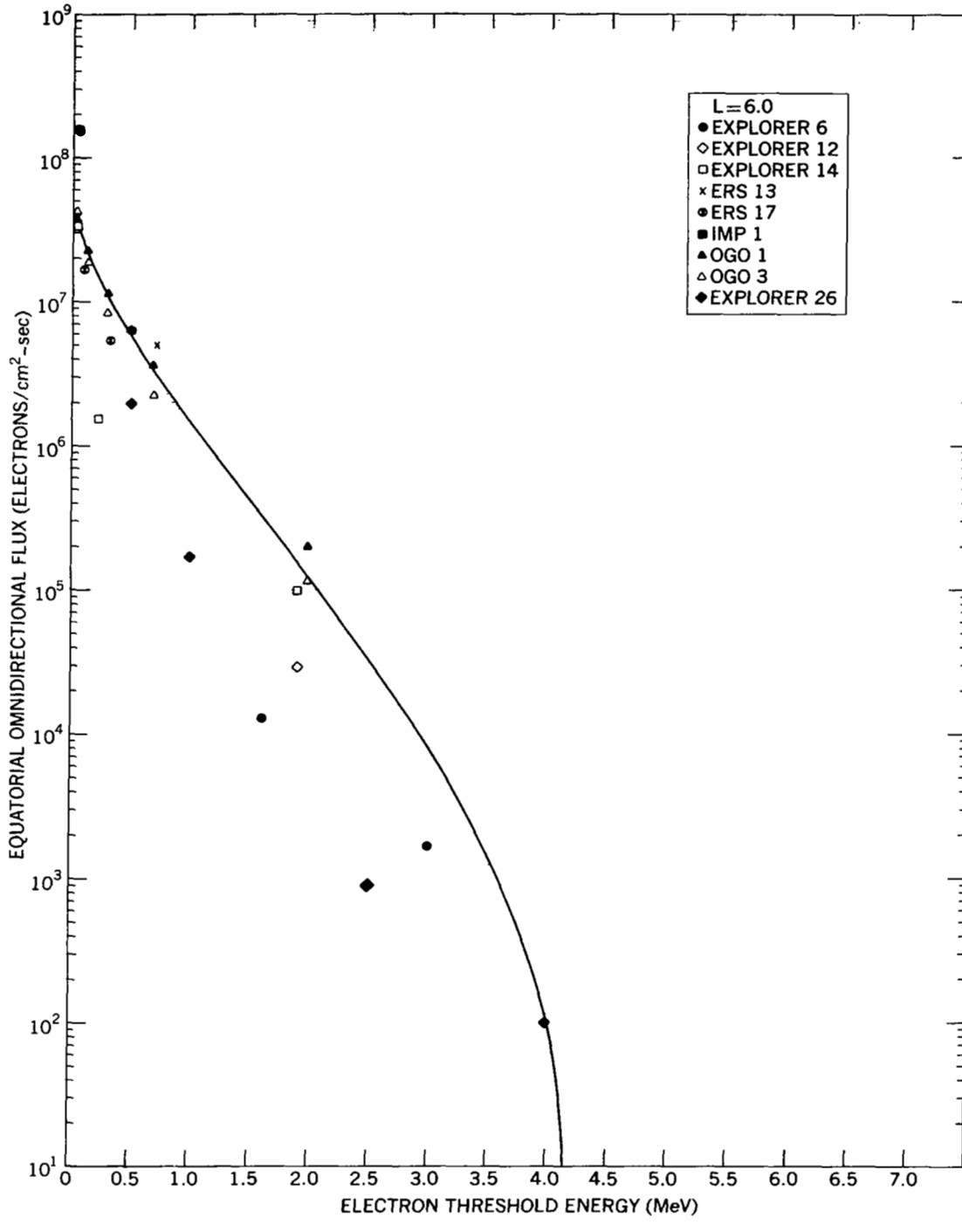

Figure 52. Comparison of AE-4 Model Spectrum with Data at L = 6.0

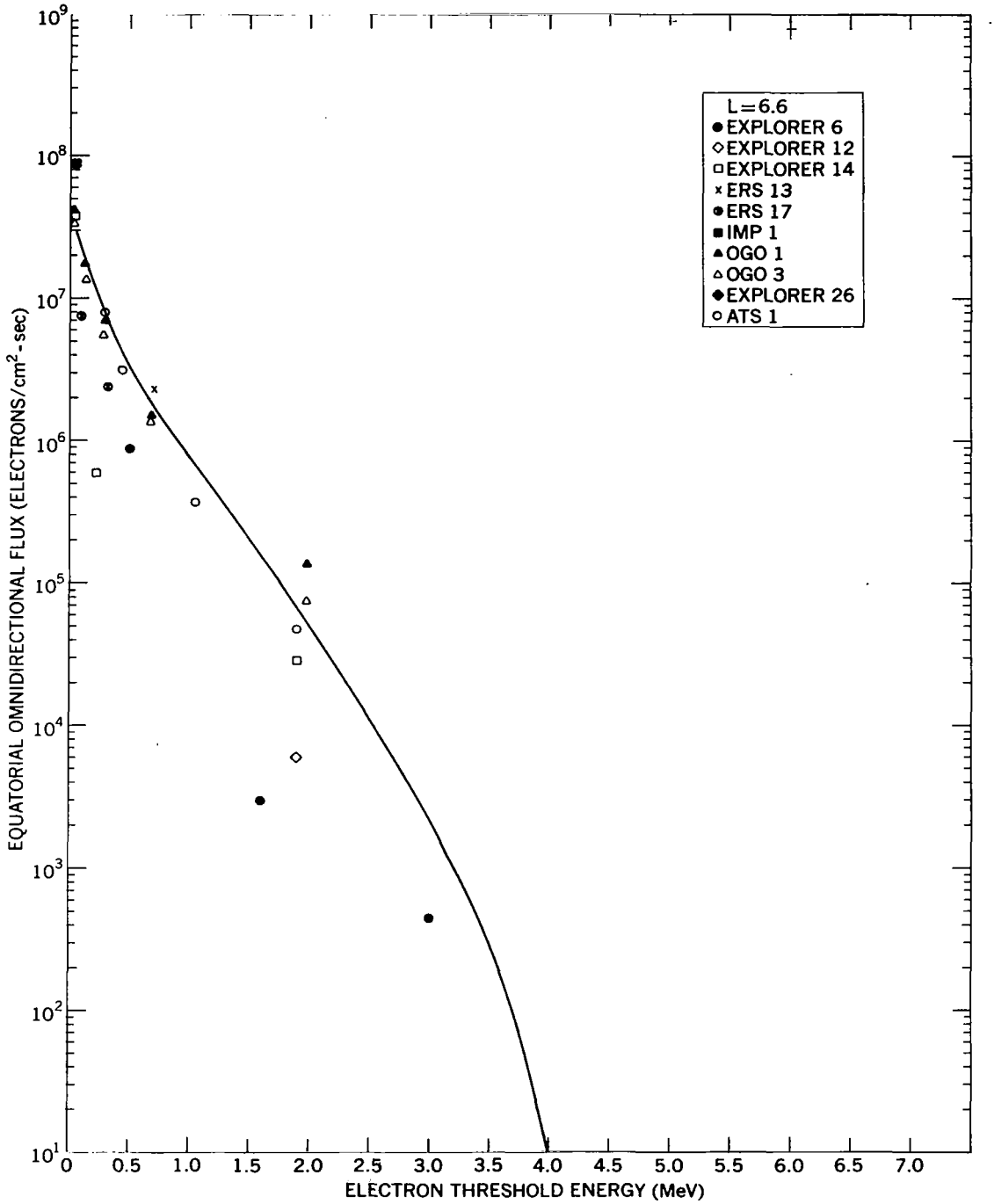

Figure 53. Comparison of AE-4 Model Spectrum with Data at L = 6.6

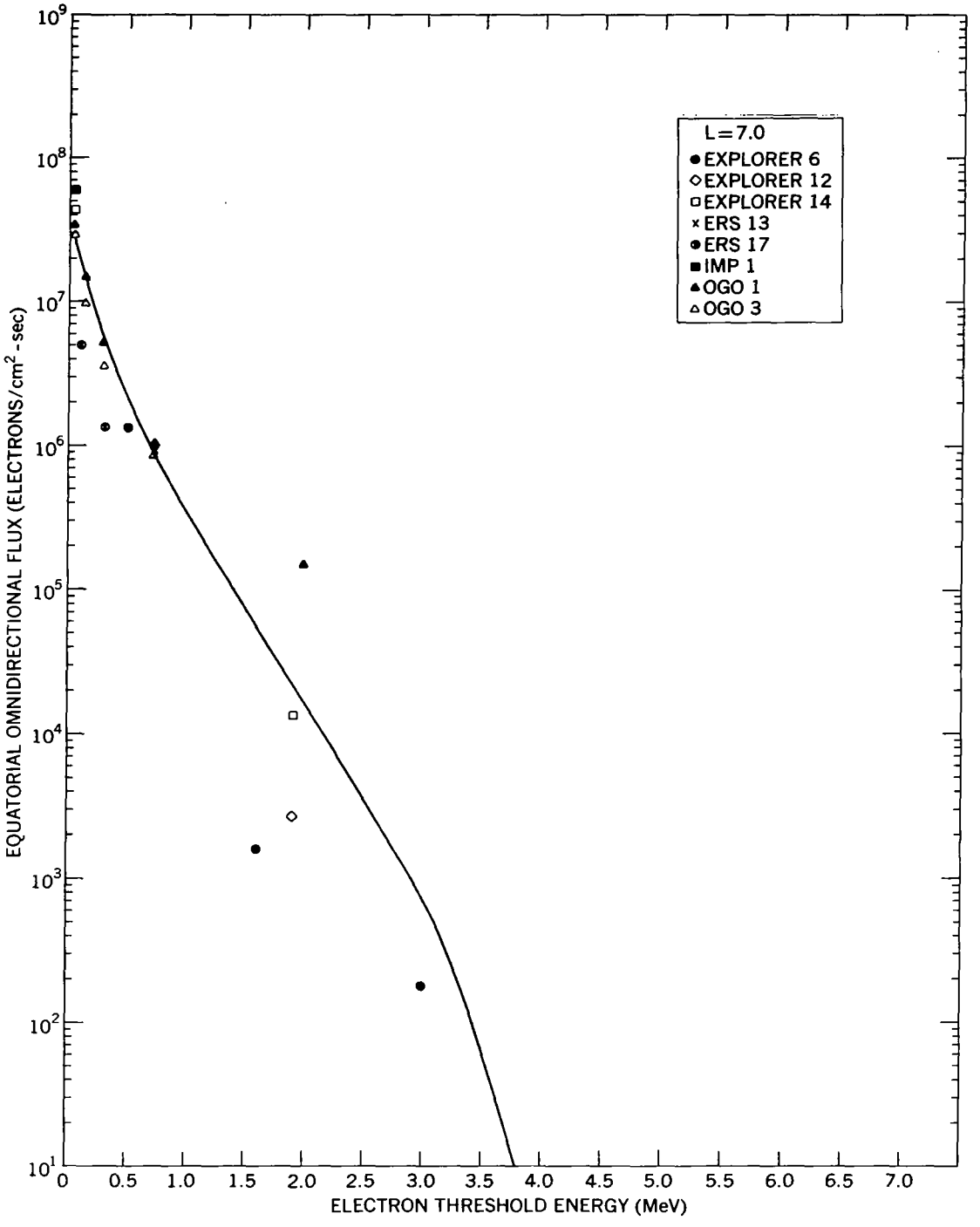

Figure 54. Comparison of AE-4 Model Spectrum with Data at L = 7.0

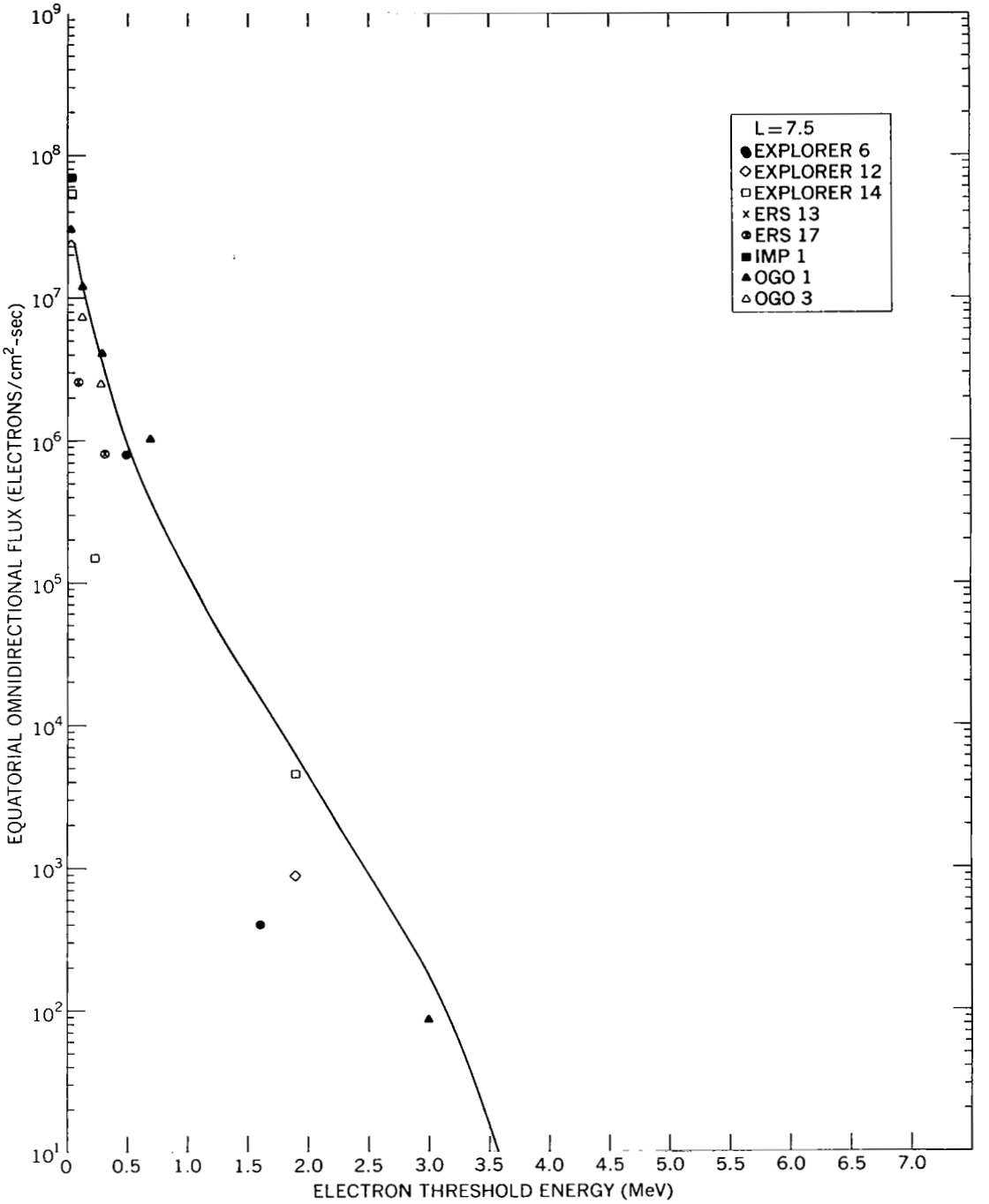

Figure 55. Comparison of AE-4 Model Spectrum with Data at L = 7.5

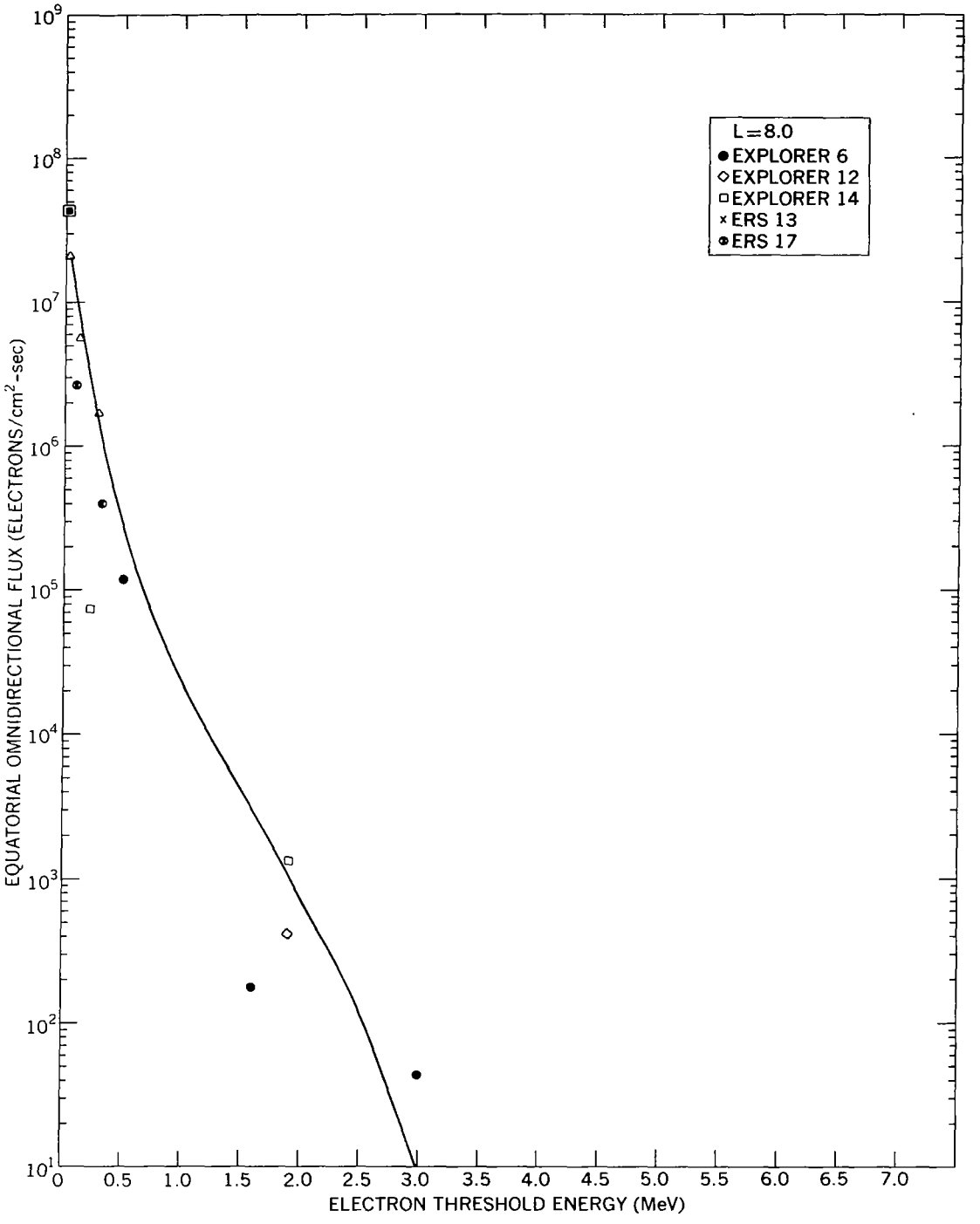

Figure 56. Comparison of AE-4 Model Spectrum with Data at L = 8.0

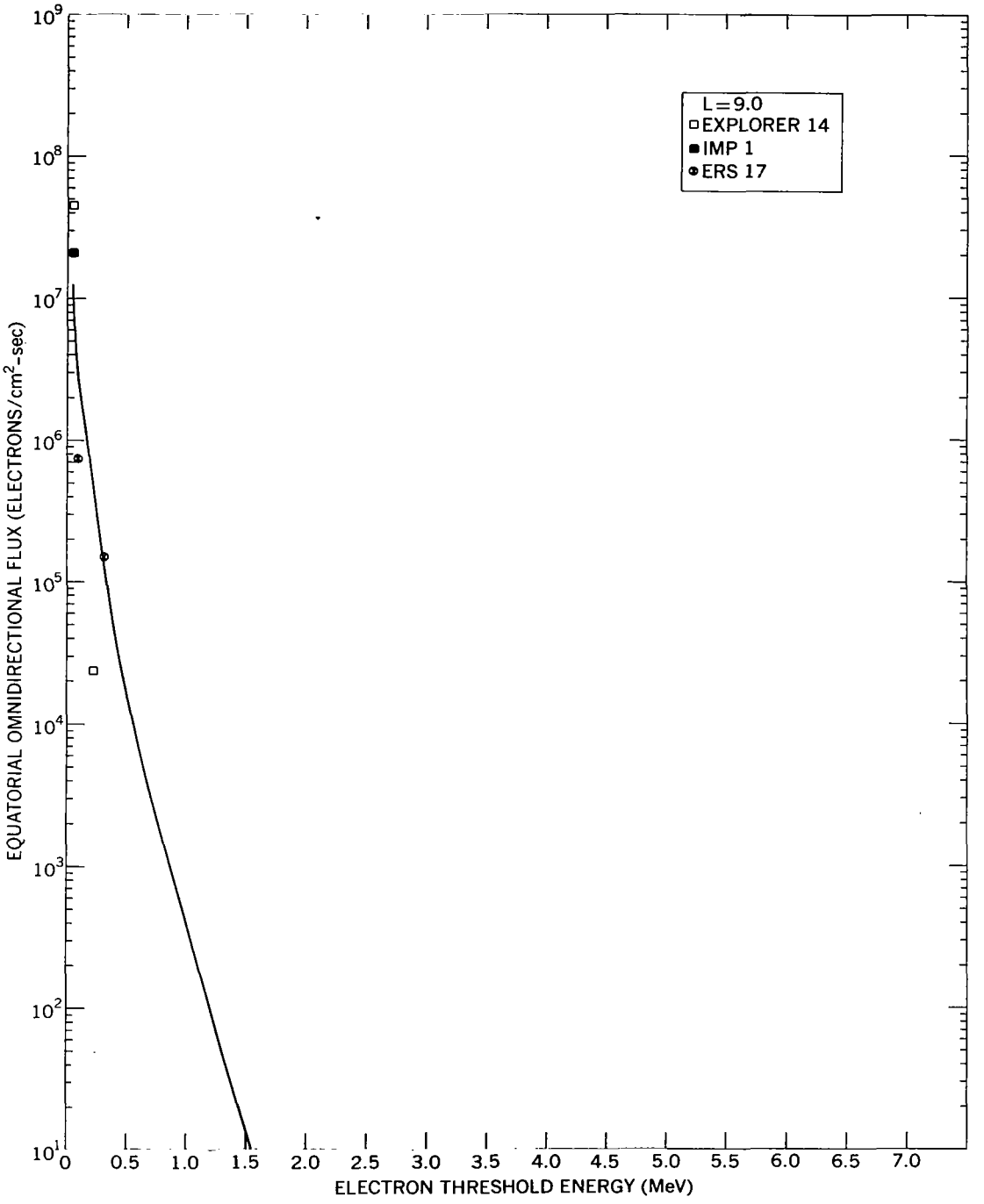

Figure 57. Comparison of AE-4 Model Spectrum with Data at L = 9.0

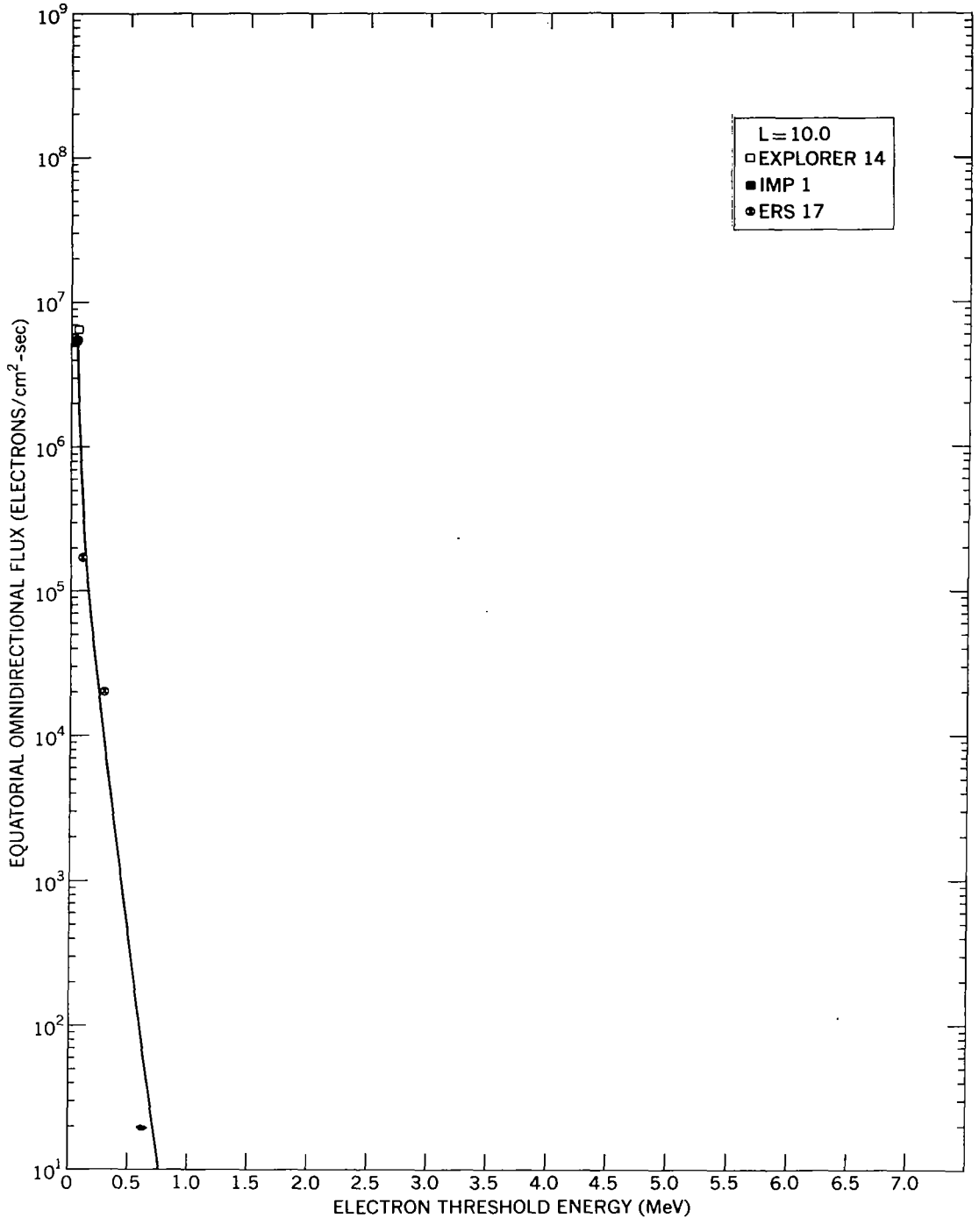

Figure 58. Comparison of AE-4 Model Spectrum with Data at L = 10.0

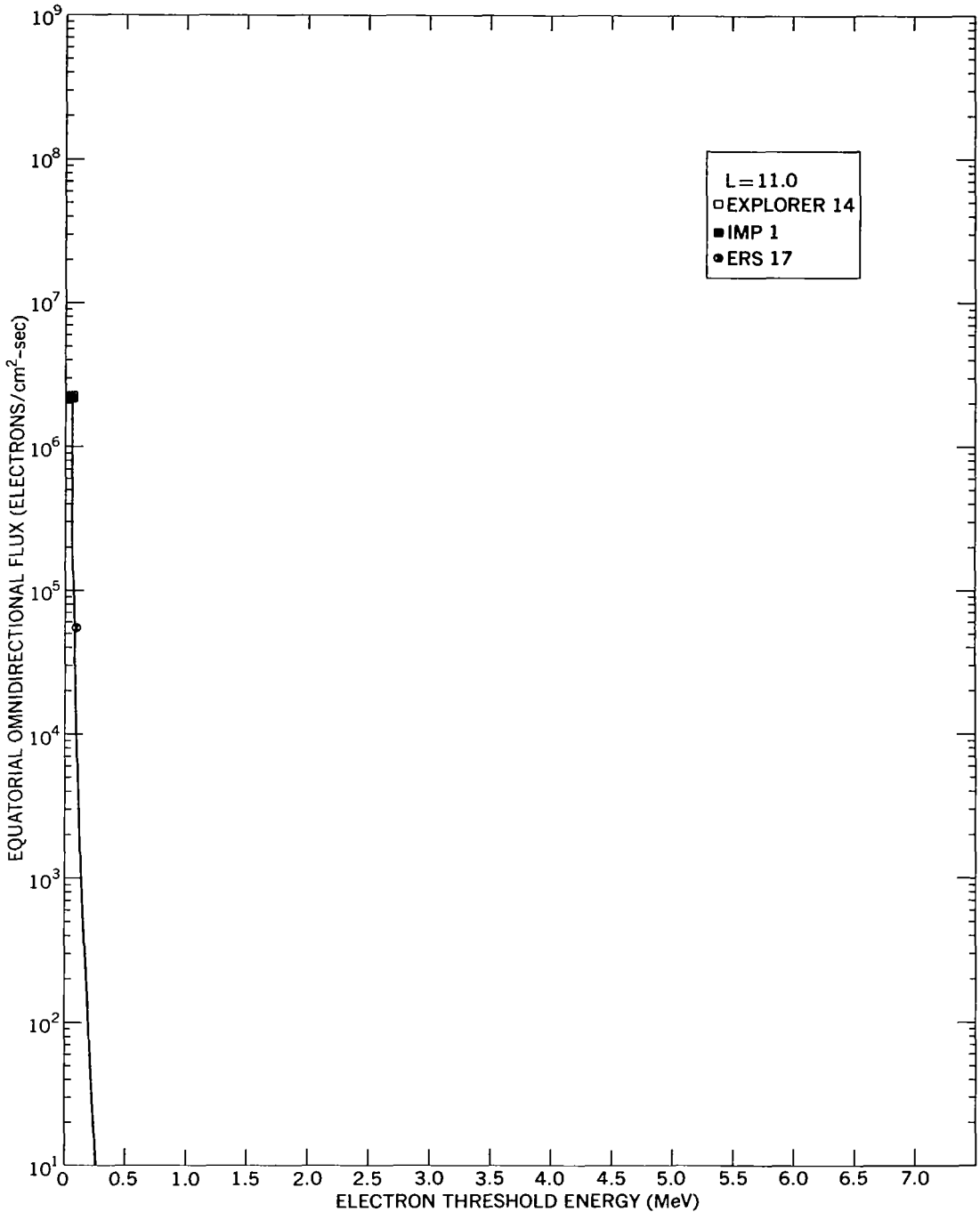

Figure 59. Comparison of AE-4 Model Spectrum with Data at L = 11.0

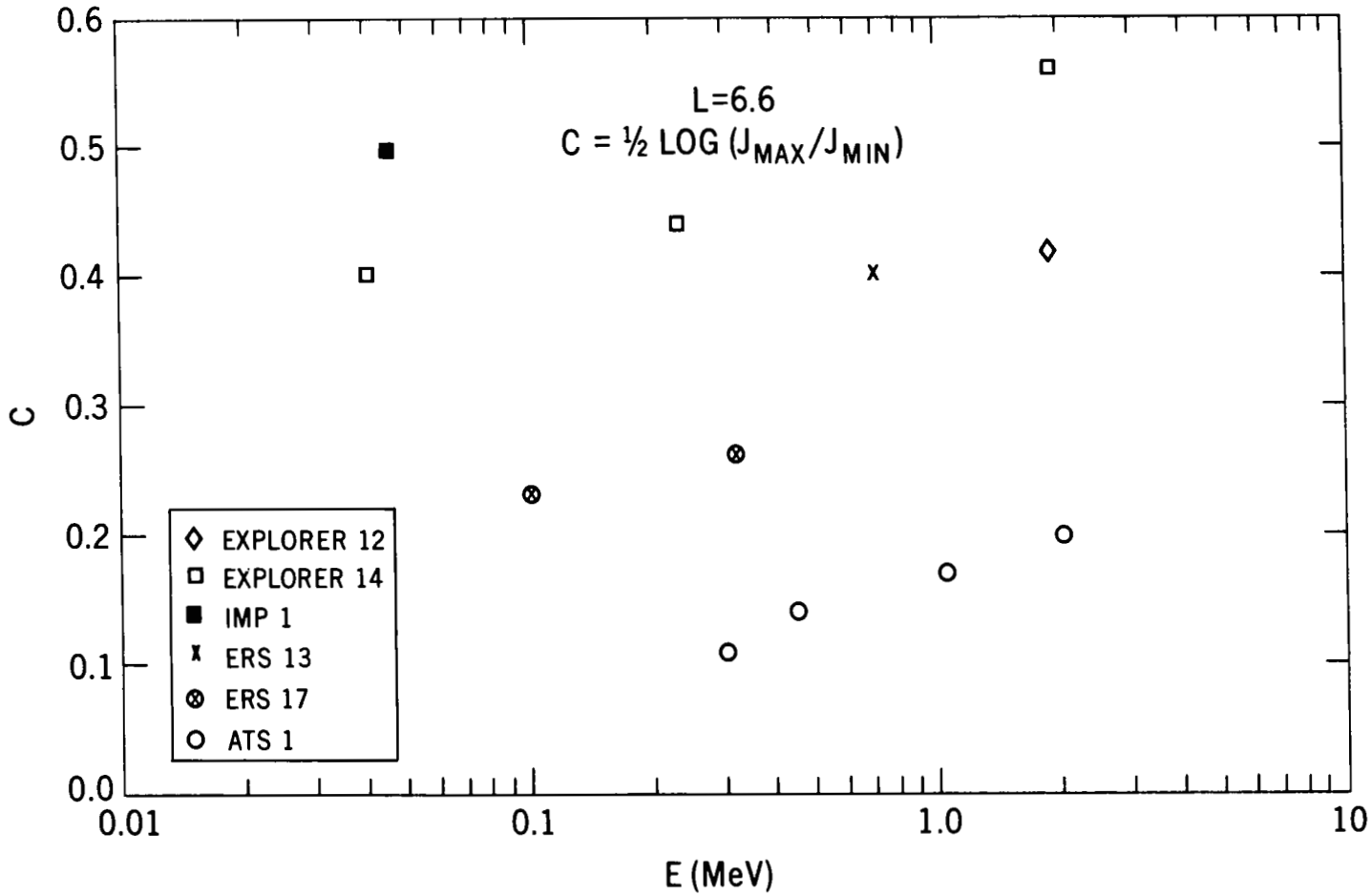

Figure 60. Amplitude of Local Time Variation for Data Near Solar Minimum and for ATS 1 Data from Near Solar Maximum

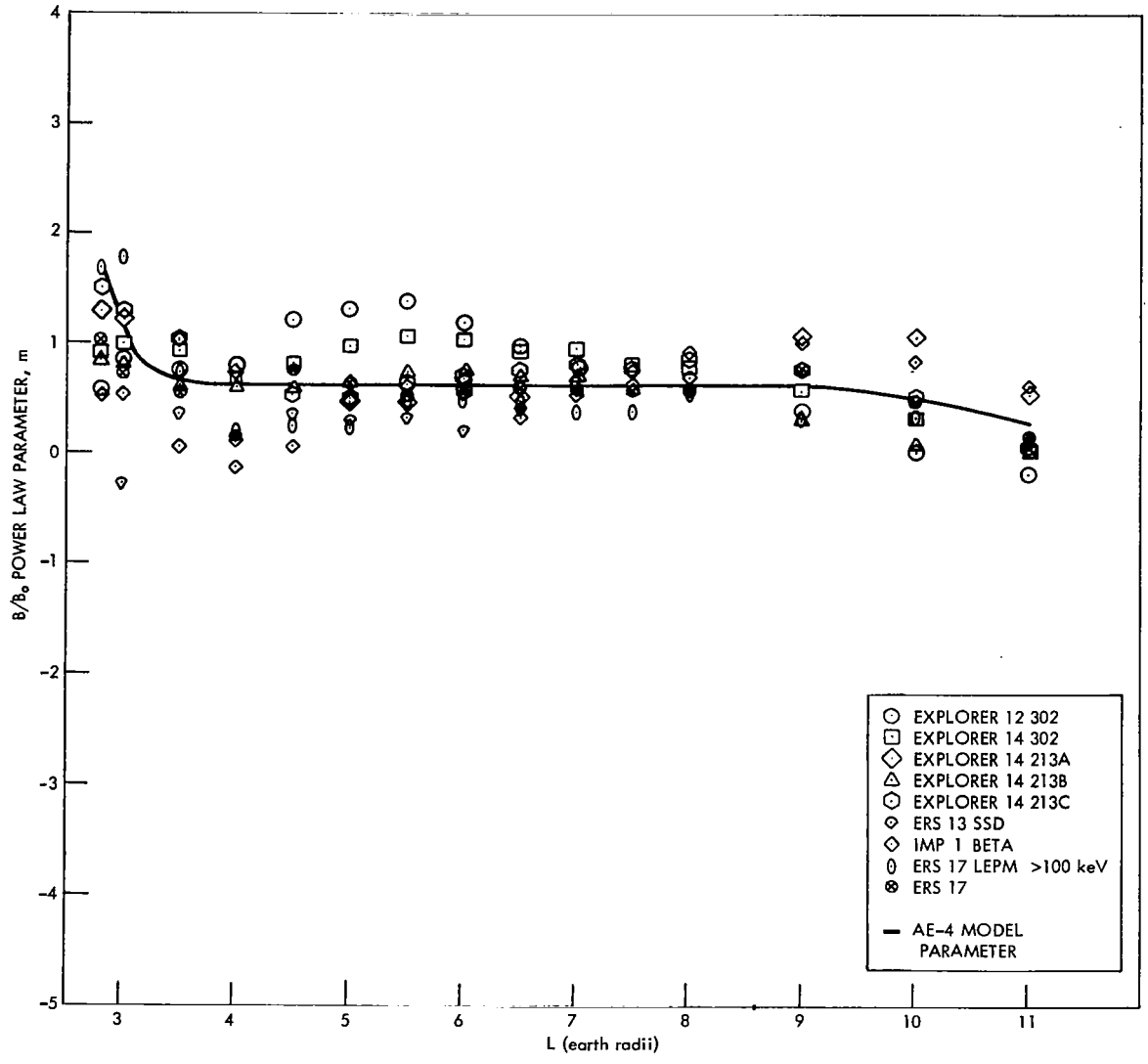

Figure 61. Comparison of Model Power Law Parameter for B/B_0 Dependence with the Calculated Parameter from Various Data Sets

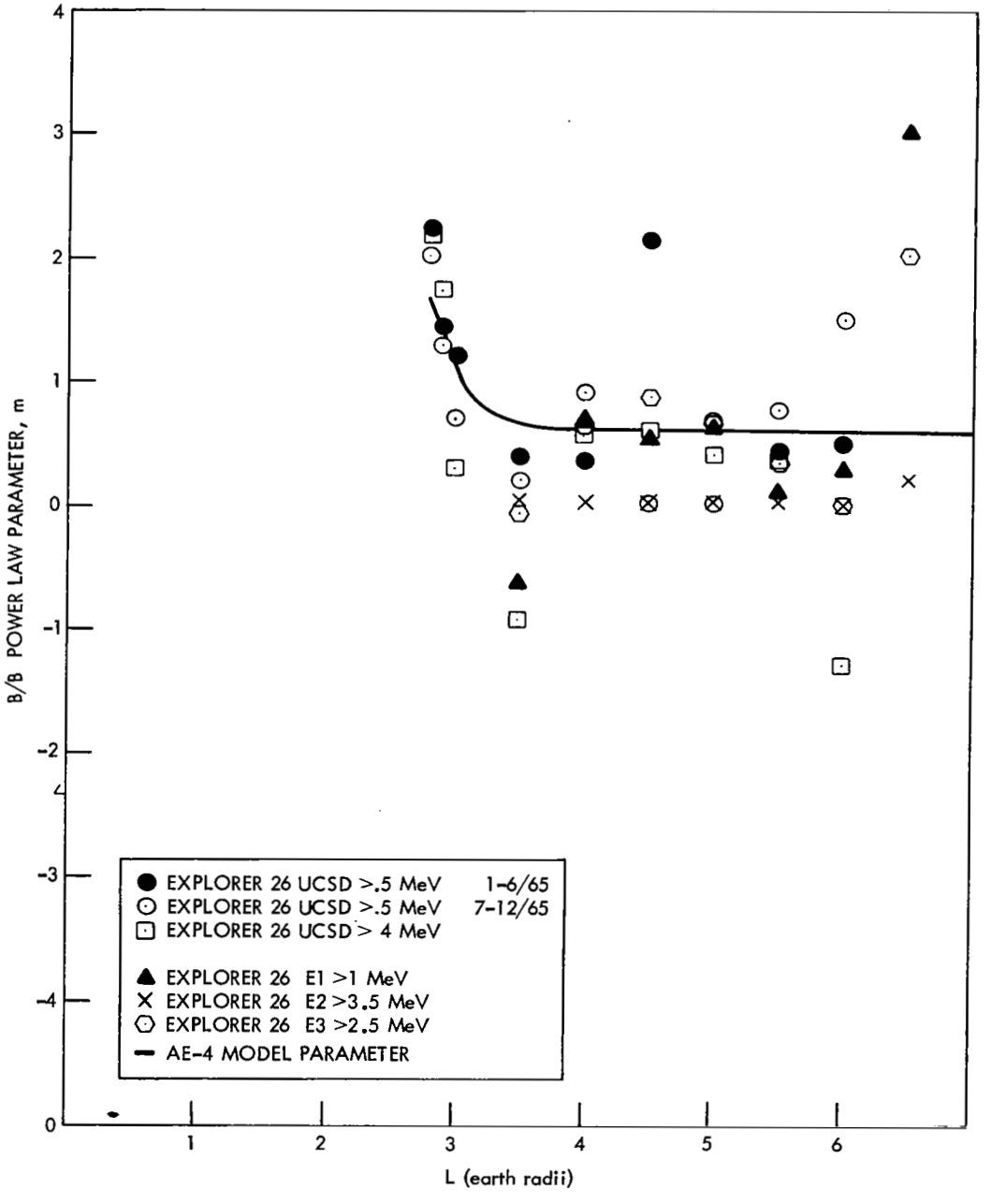

Figure 62. Comparison of Model Power Law Parameter for B/B_0 Dependence with the Calculated Parameter from Explorer 26 Data Sets

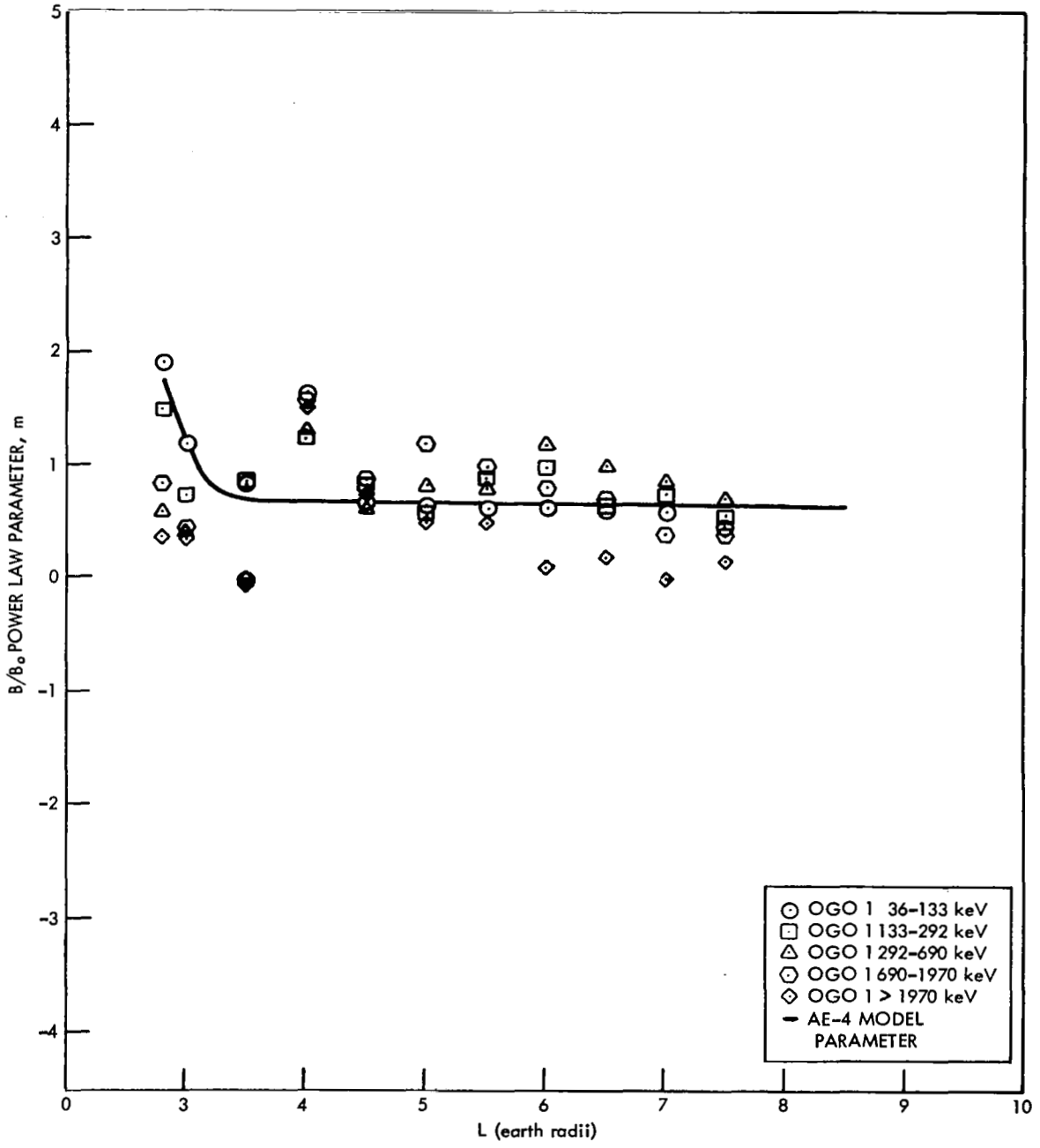

Figure 63. Comparison of Model Power Law Parameter for B/B_0 Dependence with the Calculated Parameter from OGO 1 Data Sets

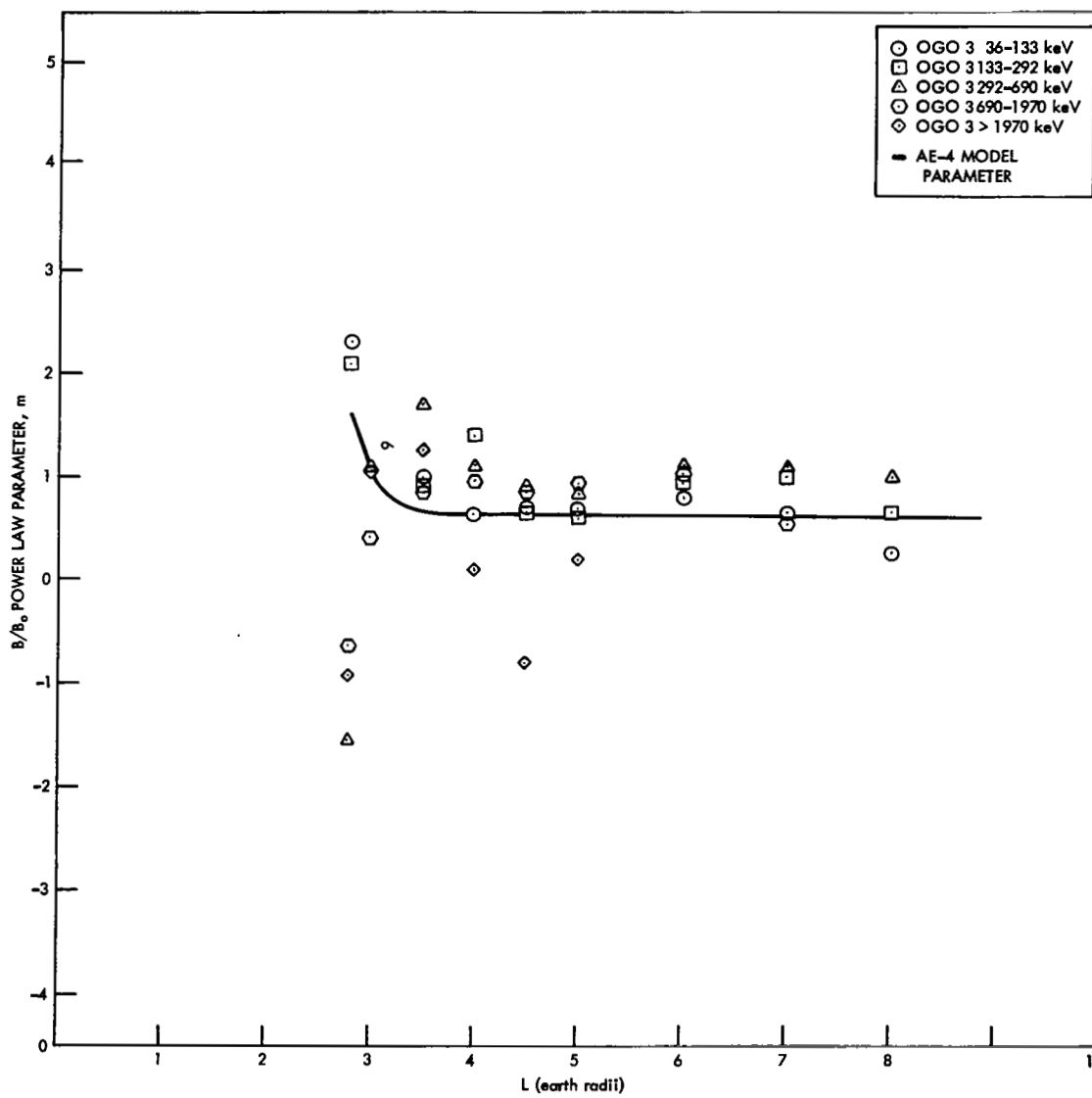

Figure 64. Comparison of Model Power Law Parameter for B/B_0 Dependence with the Calculated Parameter from OGO 3 Data Sets

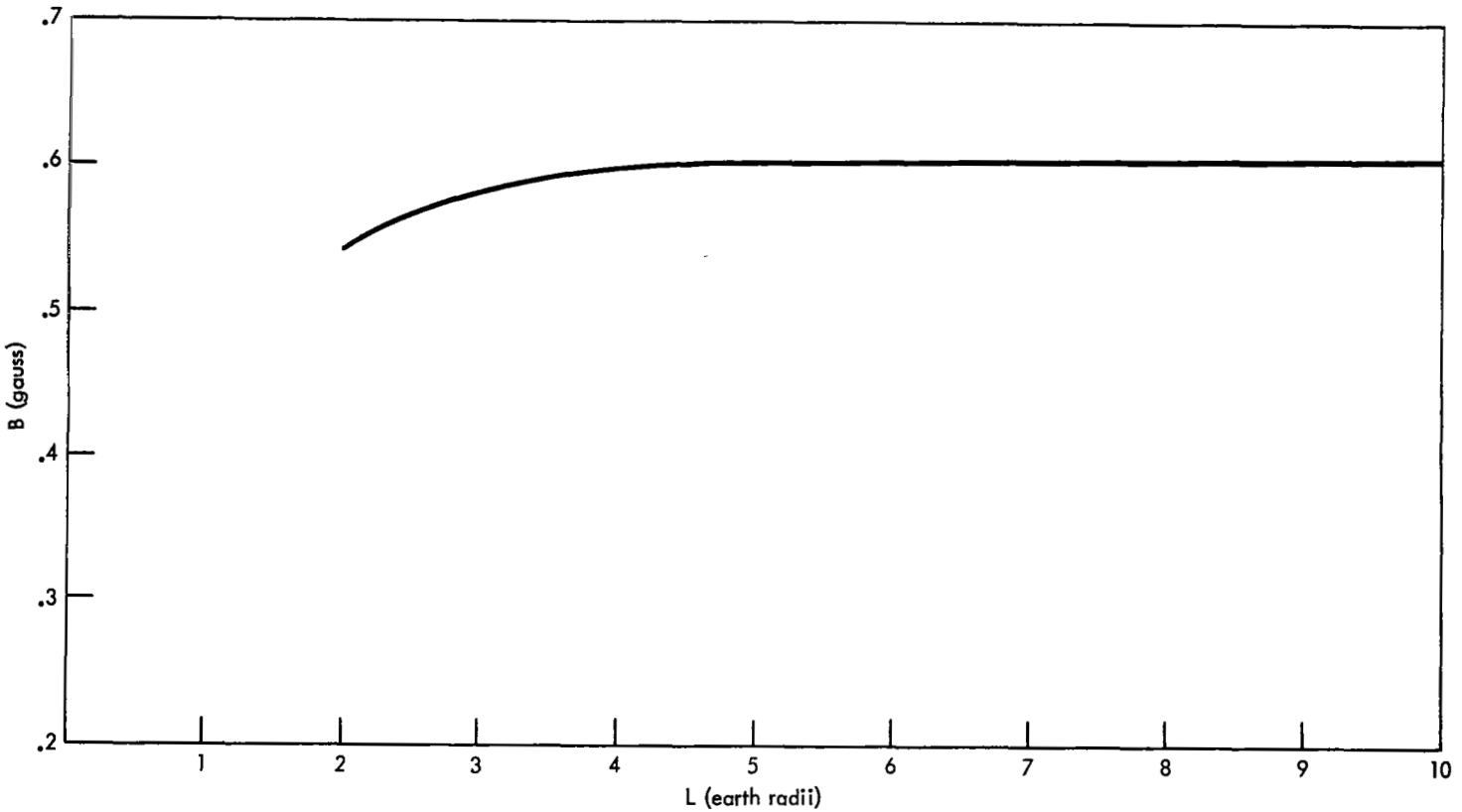

Figure 65. B Curve Chosen as Cutoff B-Values for the AE-4 Model

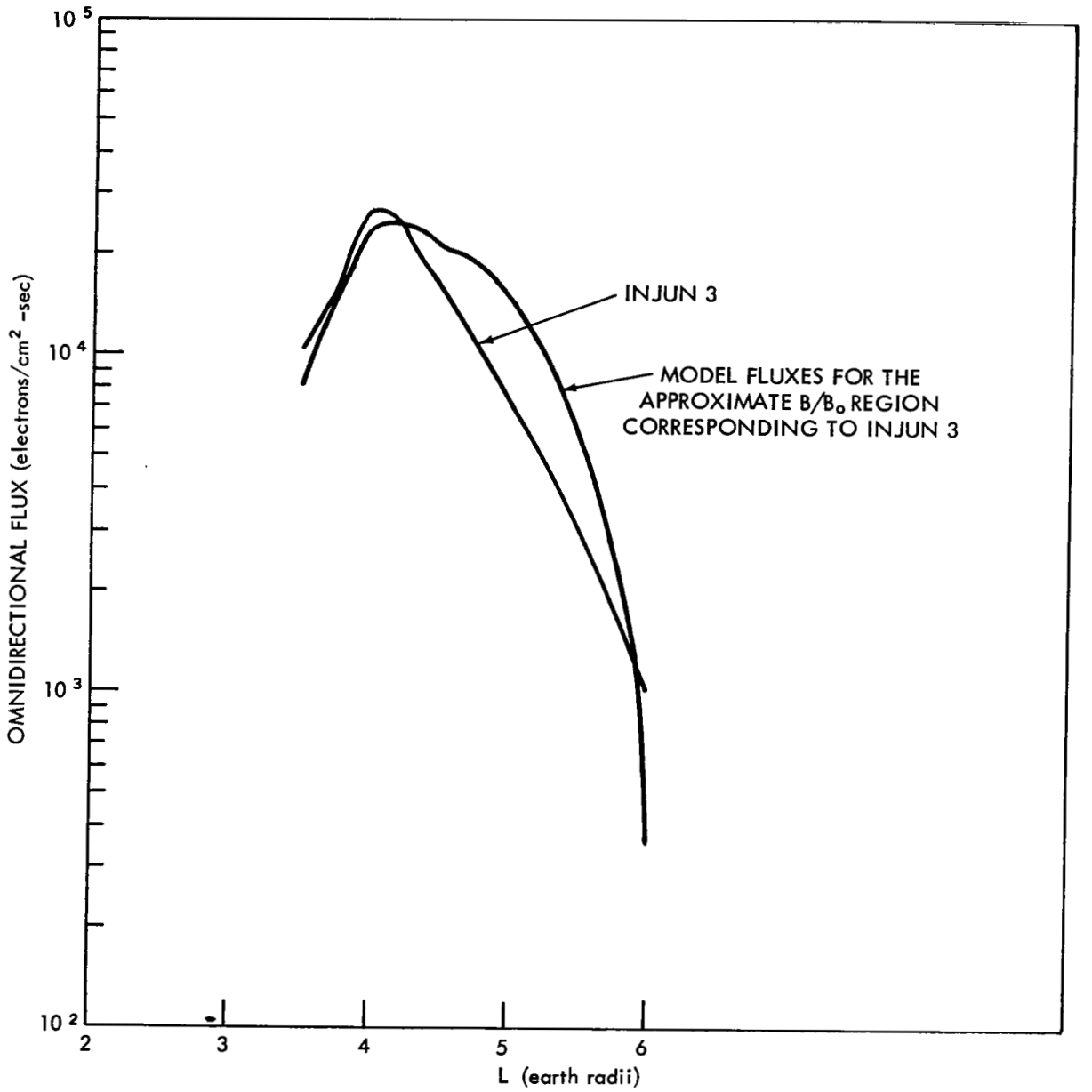

Figure 66. Comparison of Low-Altitude Injun 3 Data and AE-4 Model Flux

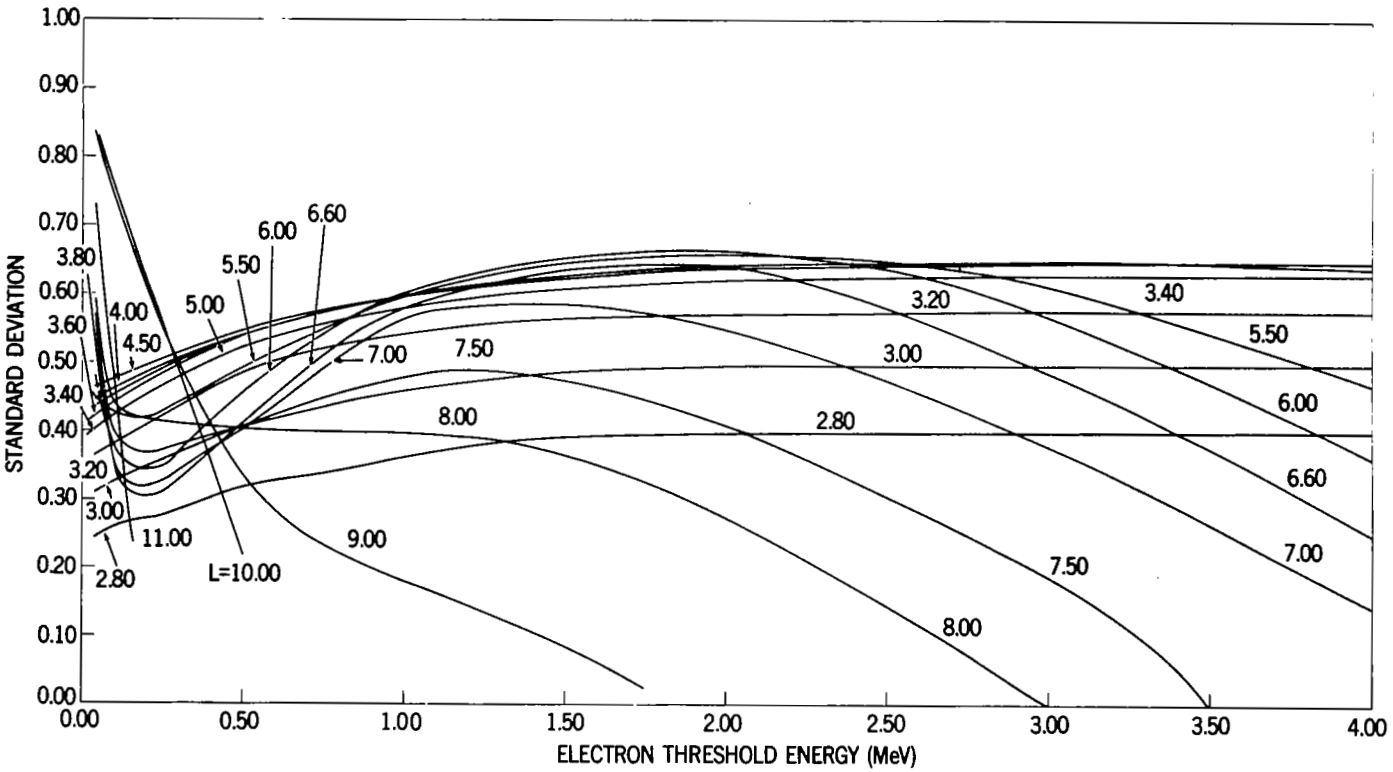

Figure 67. AE-4 Standard Deviation vs Energy for Constant L

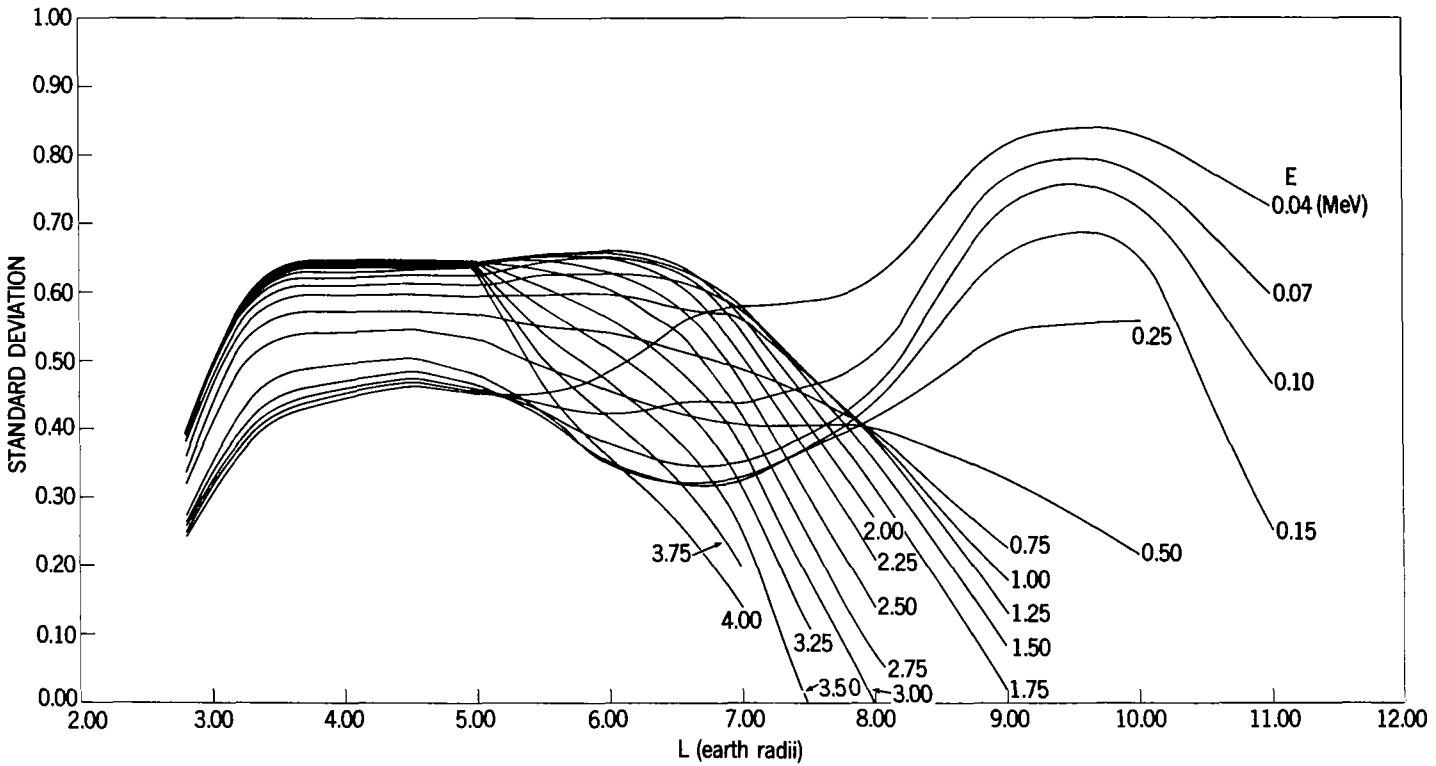

Figure 68. AE-4 Standard Deviation vs L for Constant Energy

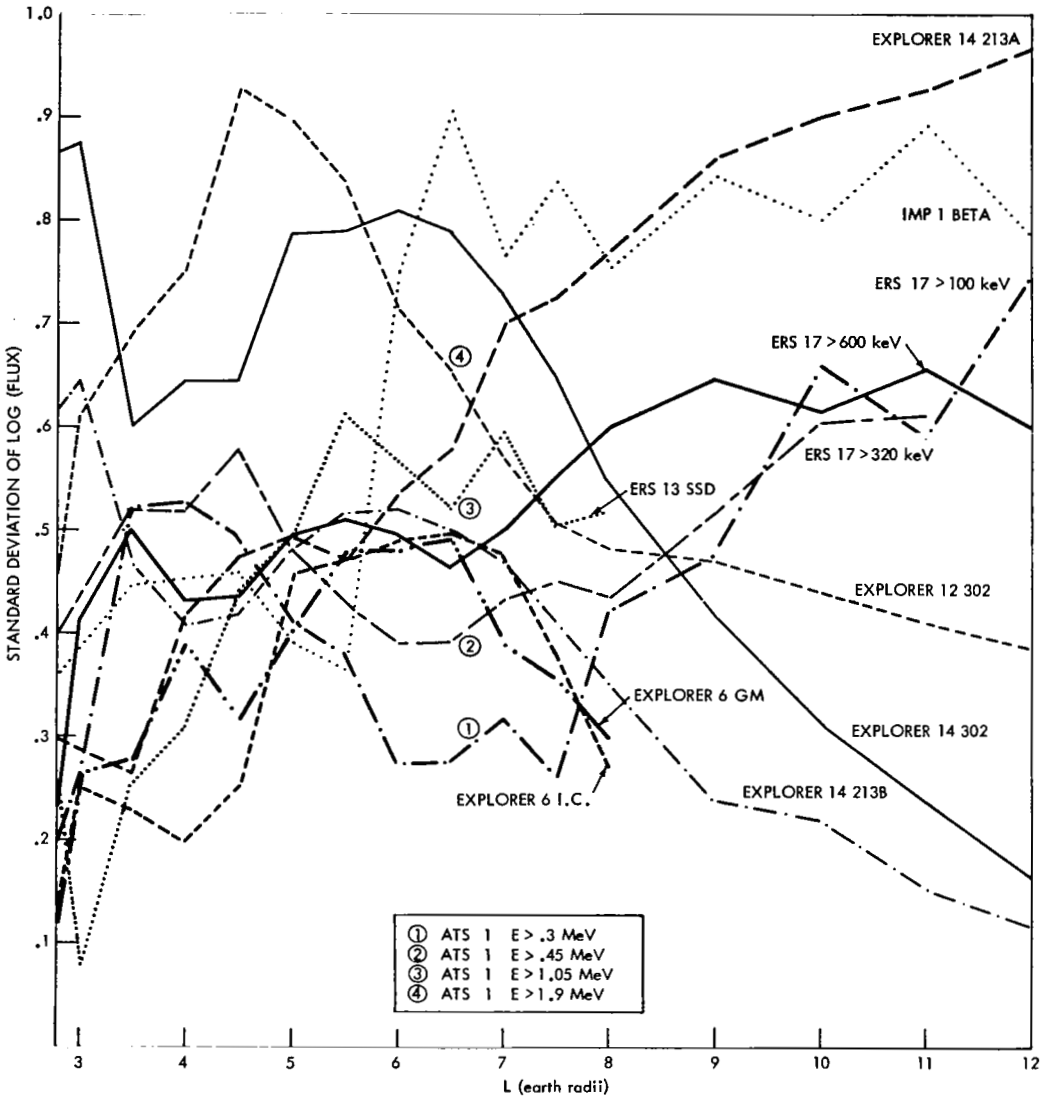

Figure 69. Standard Deviation of the Logarithm of the Flux from Several Detectors

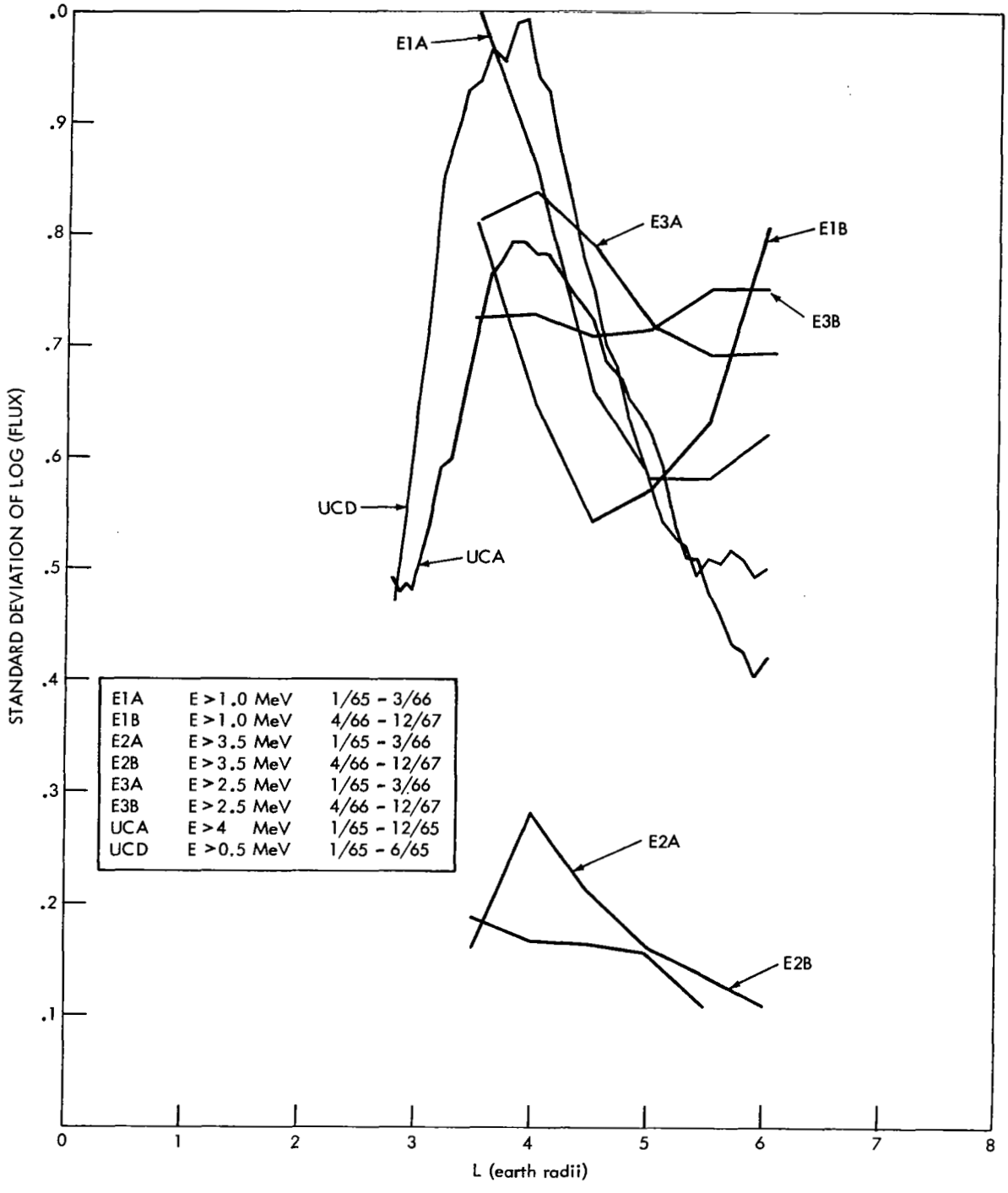

Figure 70. Standard Deviation of the Logarithm of the Flux from Explorer 26 Detectors

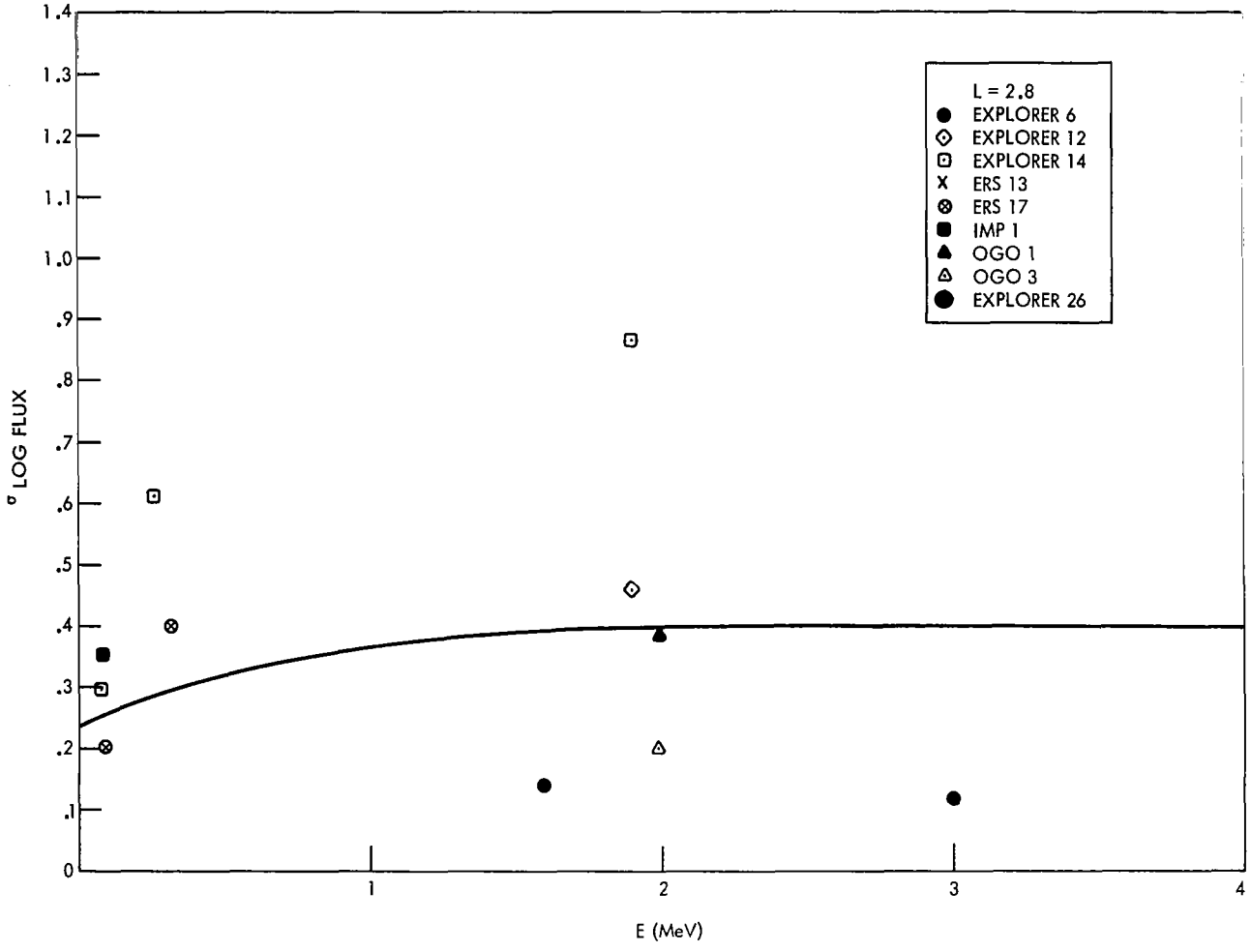

Figure 71. Comparison of AE-4 Model Standard Deviation with Standard Deviation from Data Sets, L = 2.8

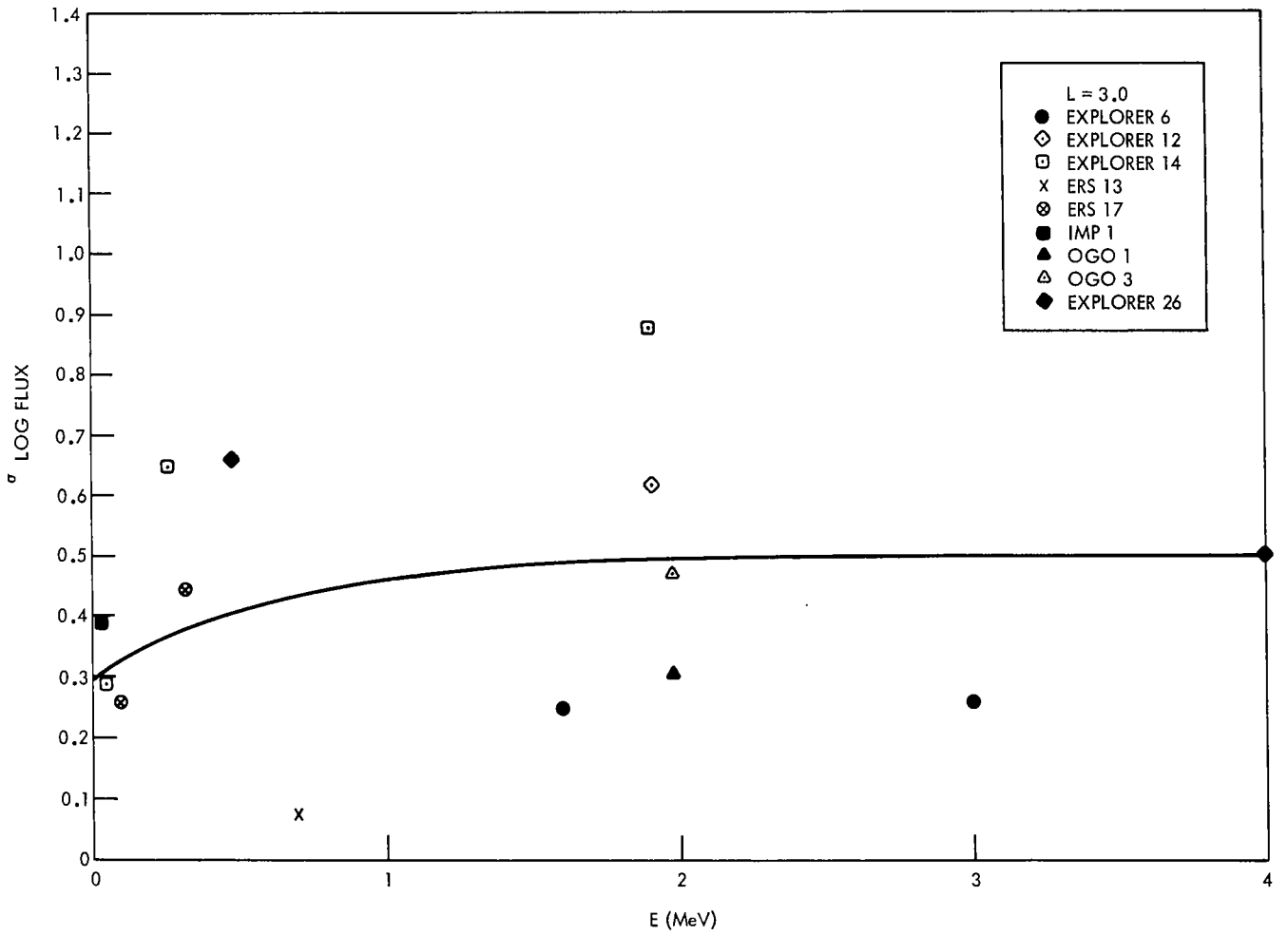

Figure 72. Comparison of AE-4 Model Standard Deviation with Standard Deviation from Data Sets, L = 3.0

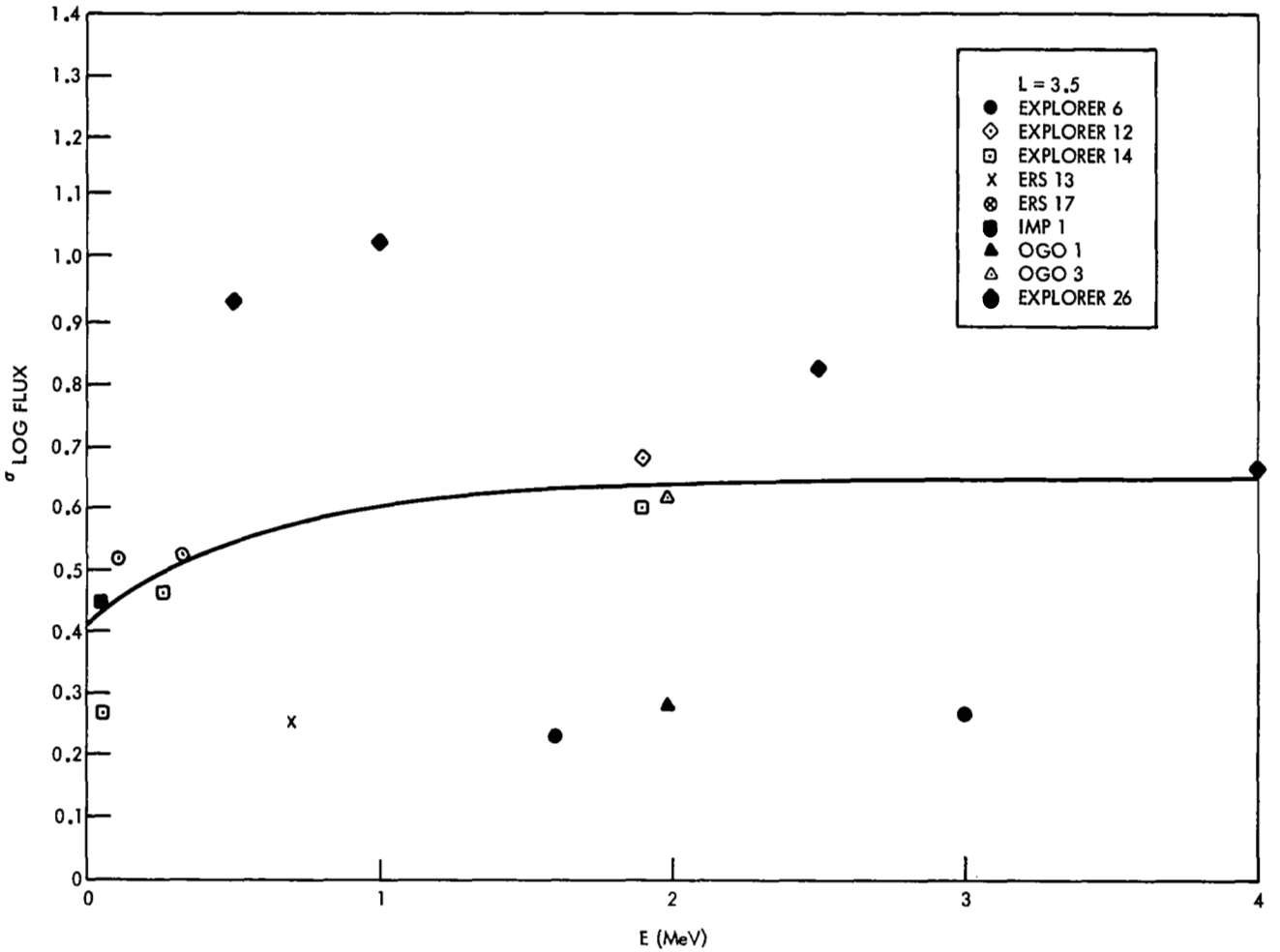

Figure 73. Comparison of AE-4 Model Standard Deviation with Standard Deviation from Data Sets, L = 3.5

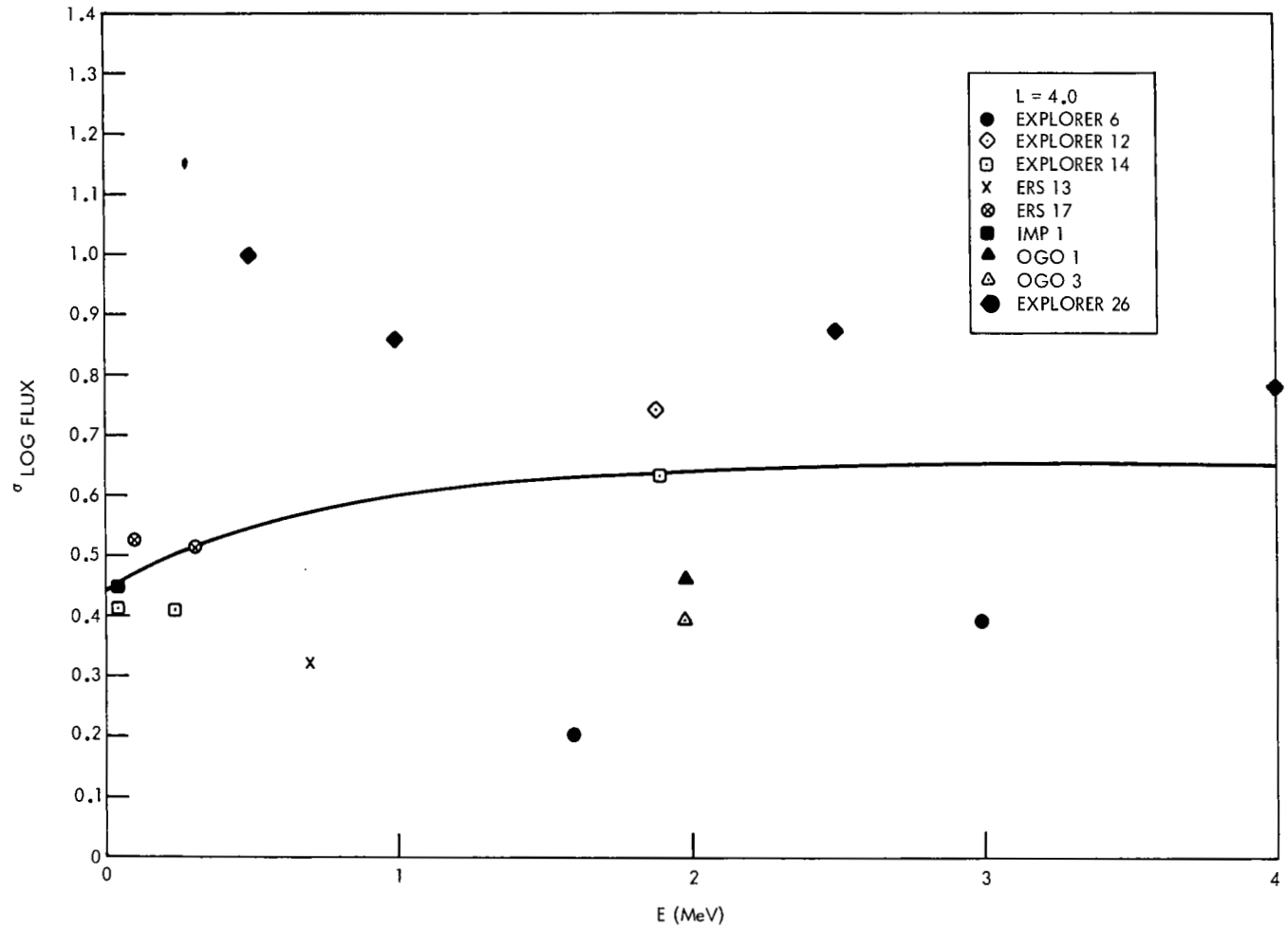

Figure 74. Comparison of AE-4 Model Standard Deviation with Standard Deviation from Data Sets, L = 4.0

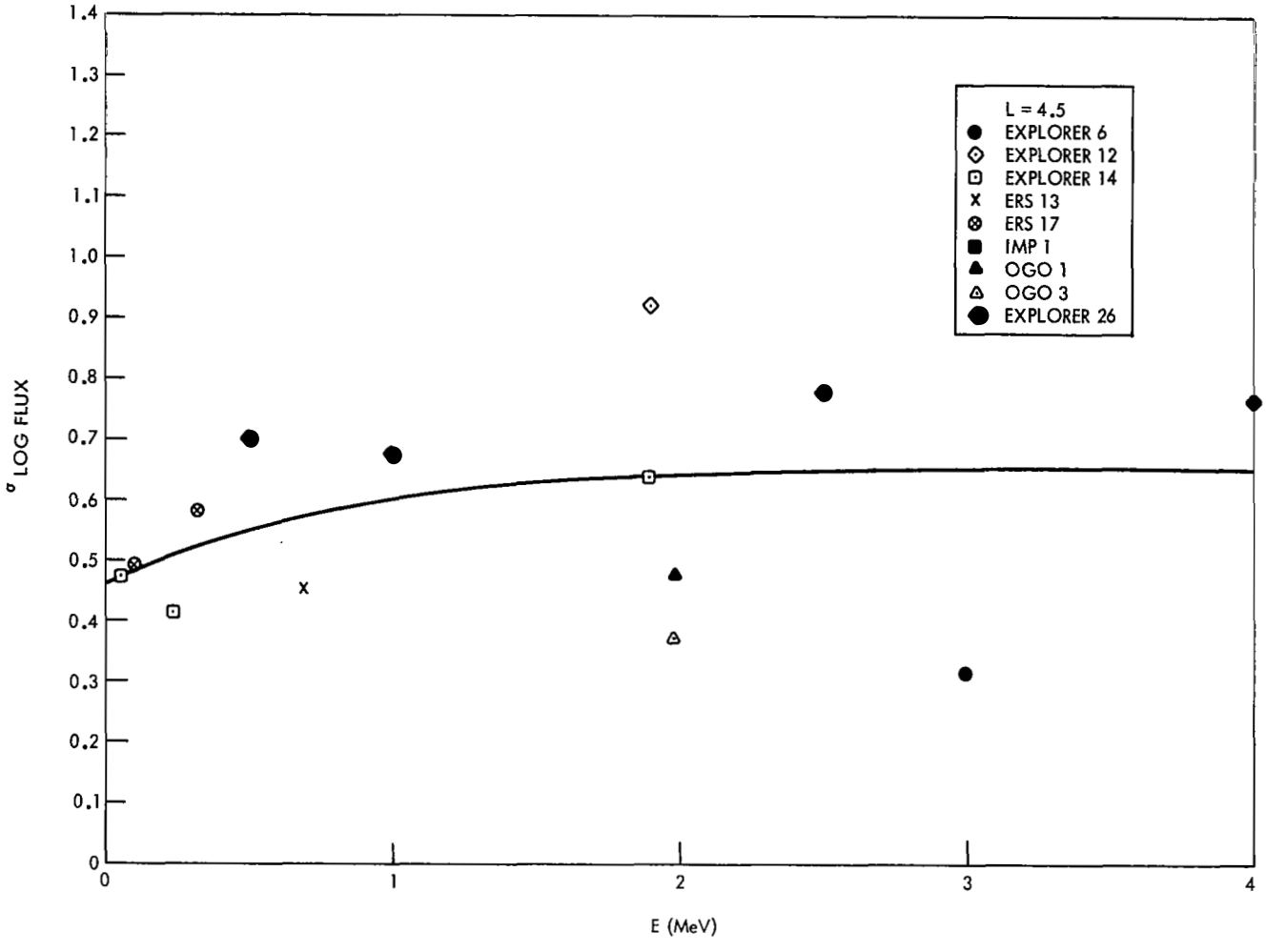

Figure 75. Comparison of AE-4 Model Standard Deviation with Standard Deviation from Data Sets, L = 4.5

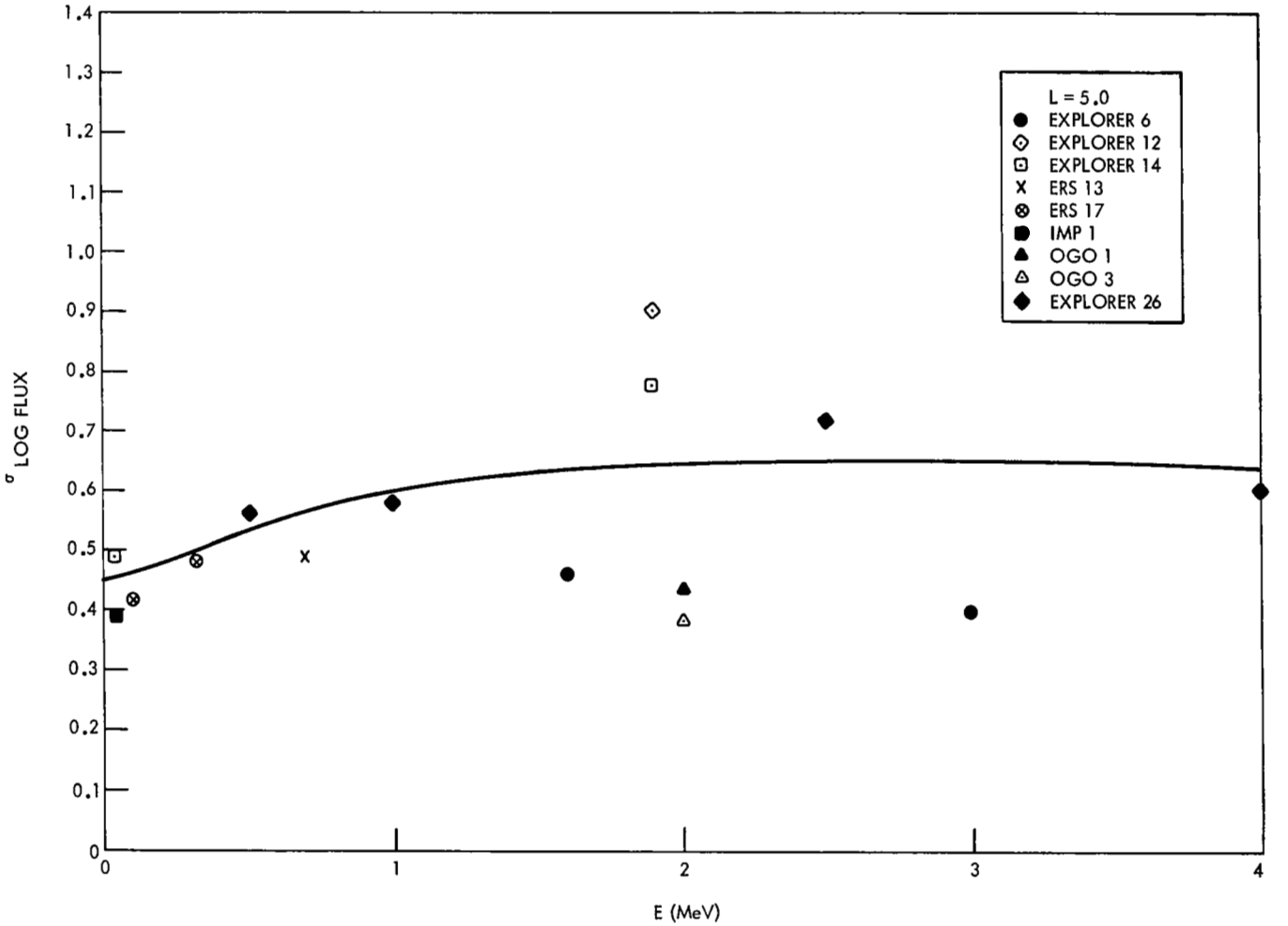

Figure 76. Comparison of AE-4 Model Standard Deviation with Standard Deviation from Data Sets, L = 5.0

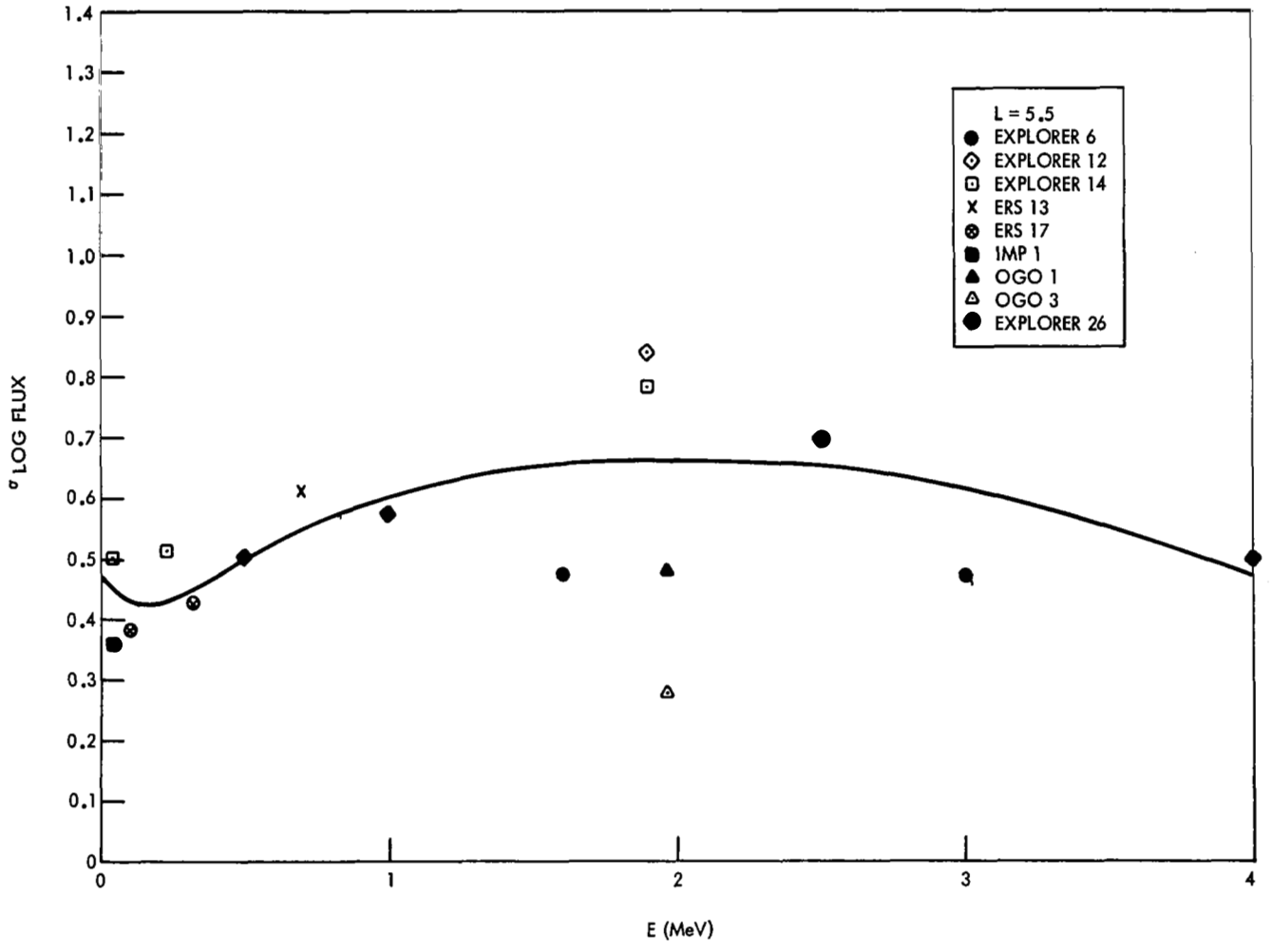

Figure 77. Comparison of AE-4 Model Standard Deviation with Standard Deviation from Data Sets, L = 5.5

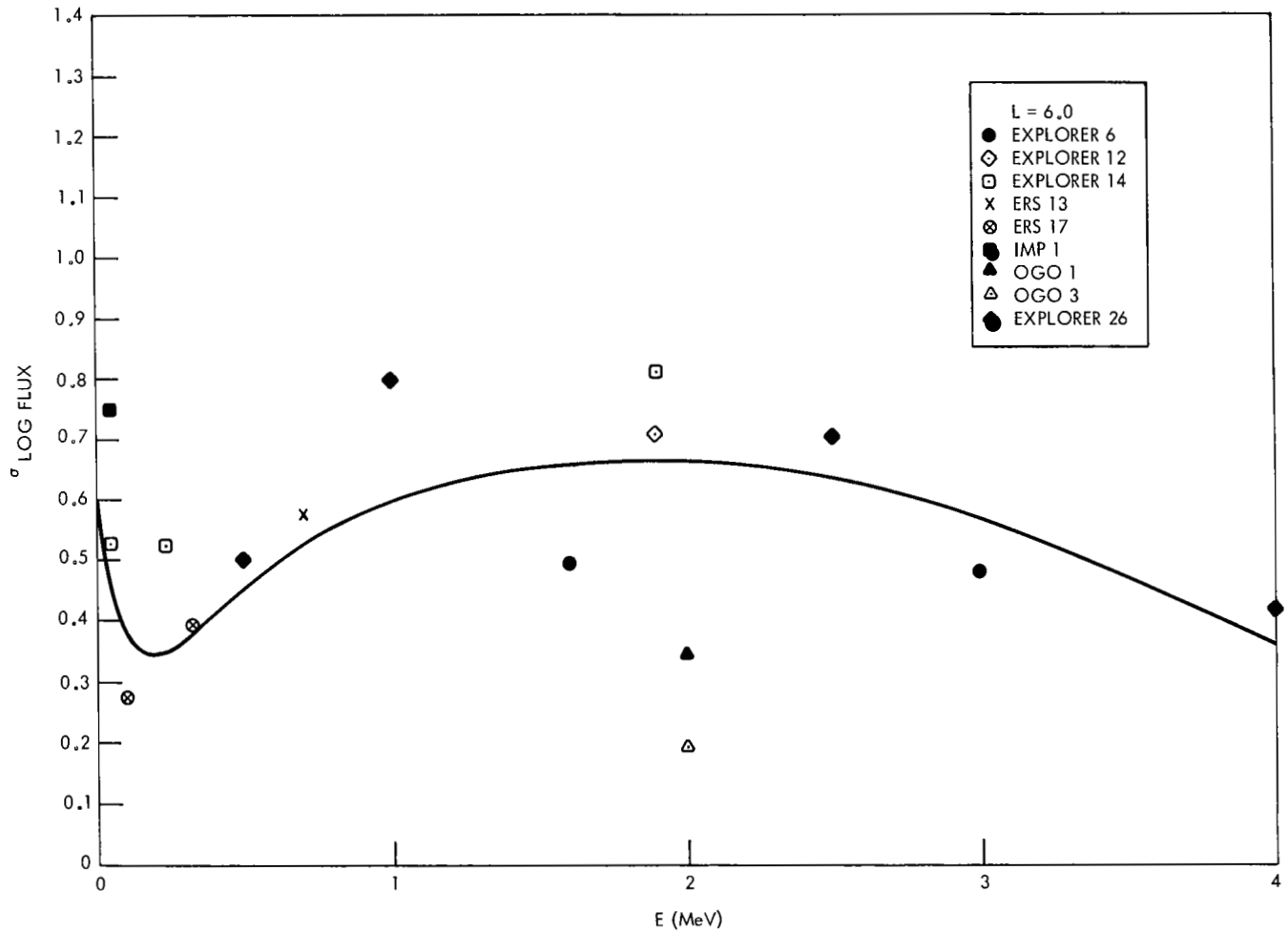

Figure 78. Comparison of AE-4 Model Standard Deviation with Standard Deviation from Data Sets, L = 6.0

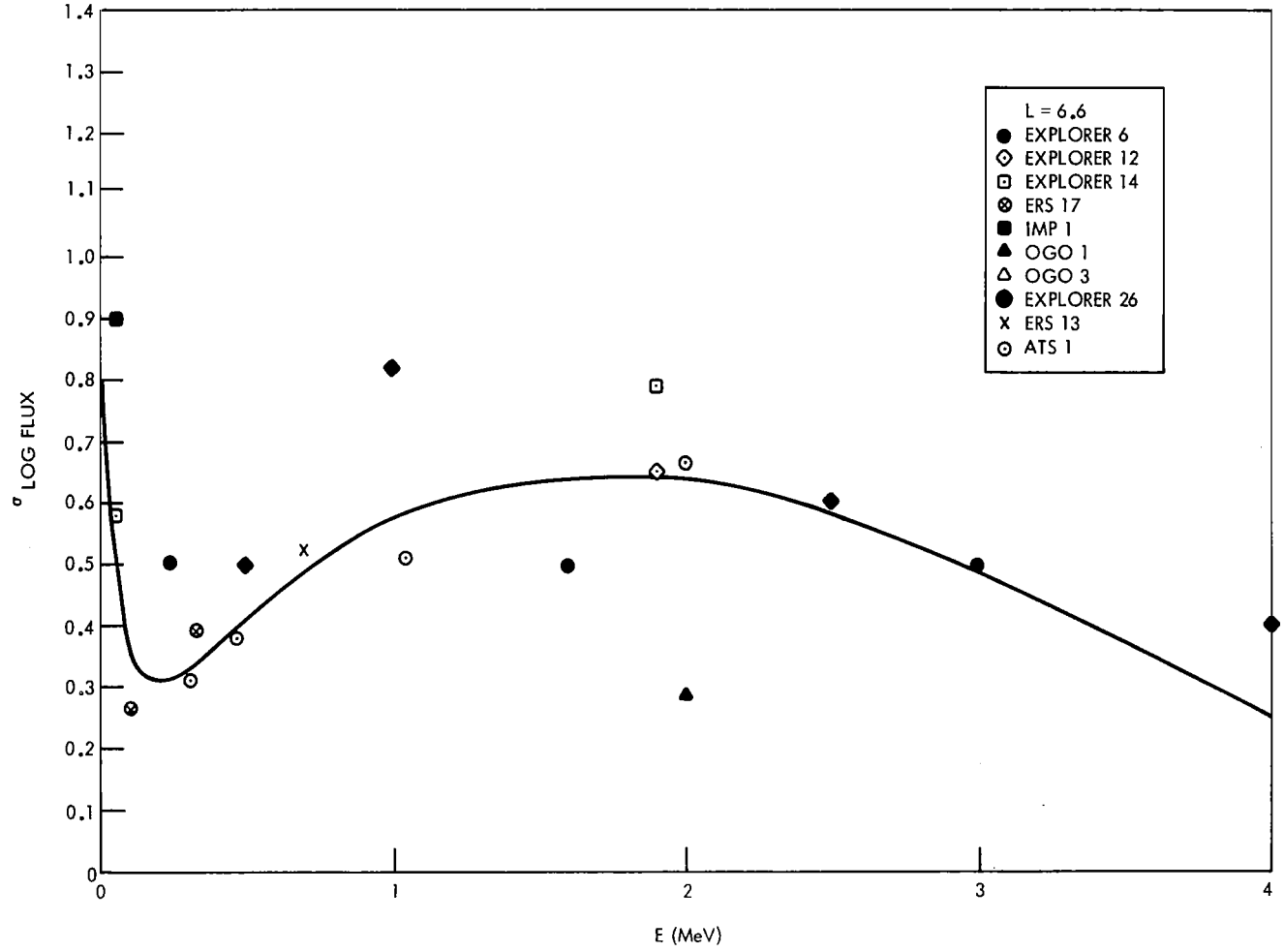

Figure 79. Comparison of AE-4 Model Standard Deviation with Standard Deviation from Data Sets, L = 6.6

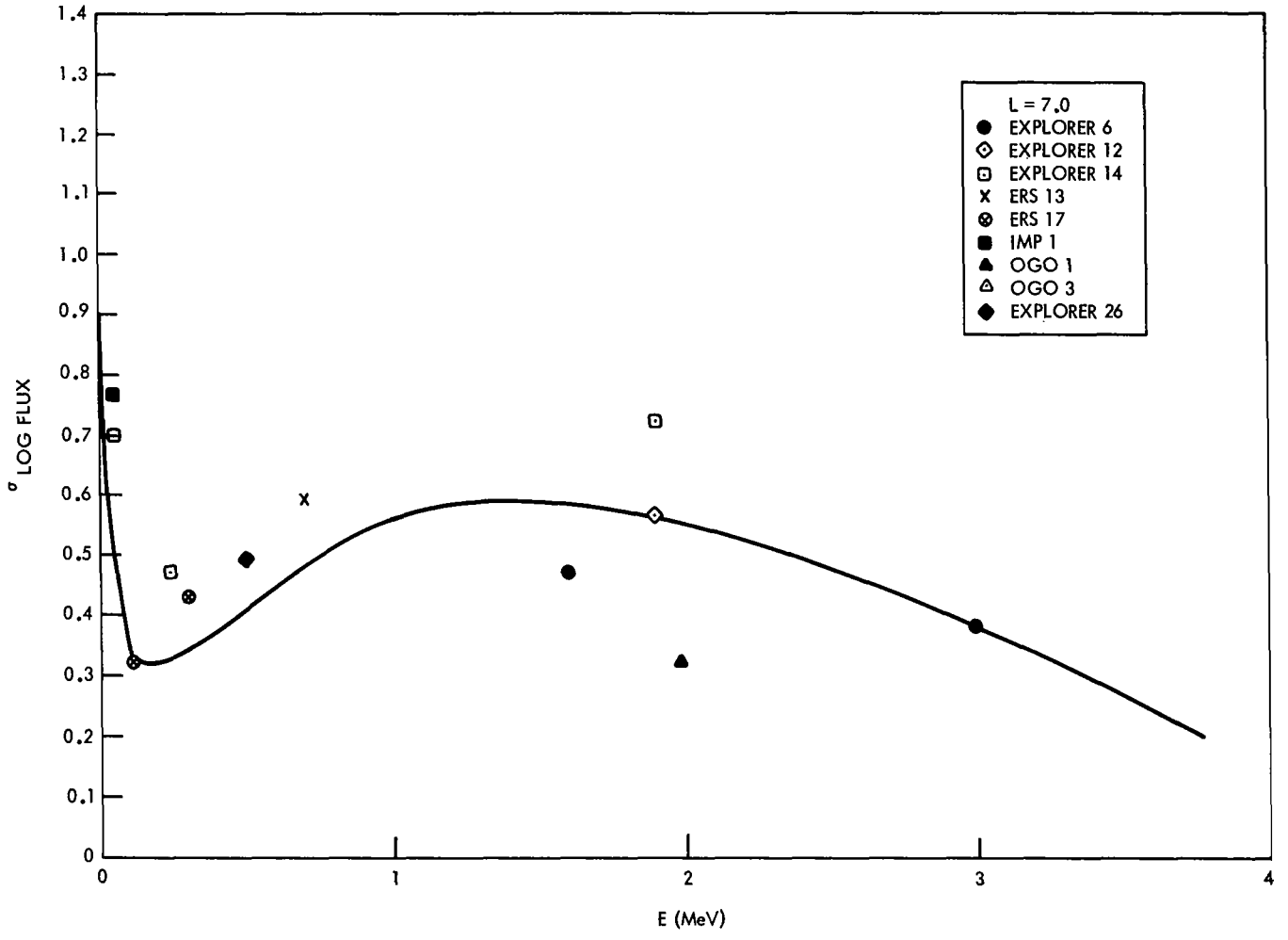

Figure 80. Comparison of AE-4 Model Standard Deviation with Standard Deviation from Data Sets, L = 7.0

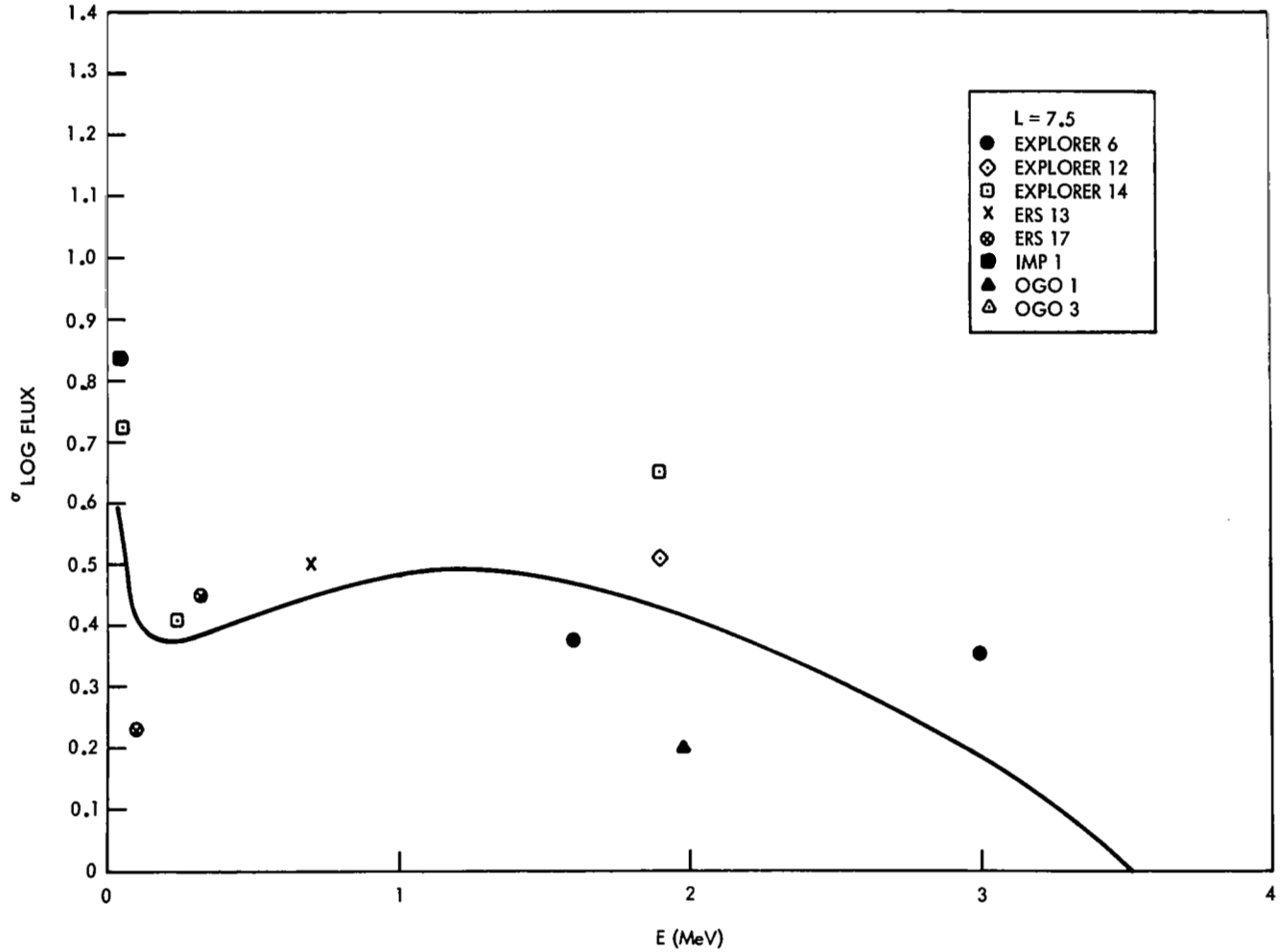

Figure 81. Comparison of AE-4 Model Standard Deviation with Standard Deviation from Data Sets, L = 7.5

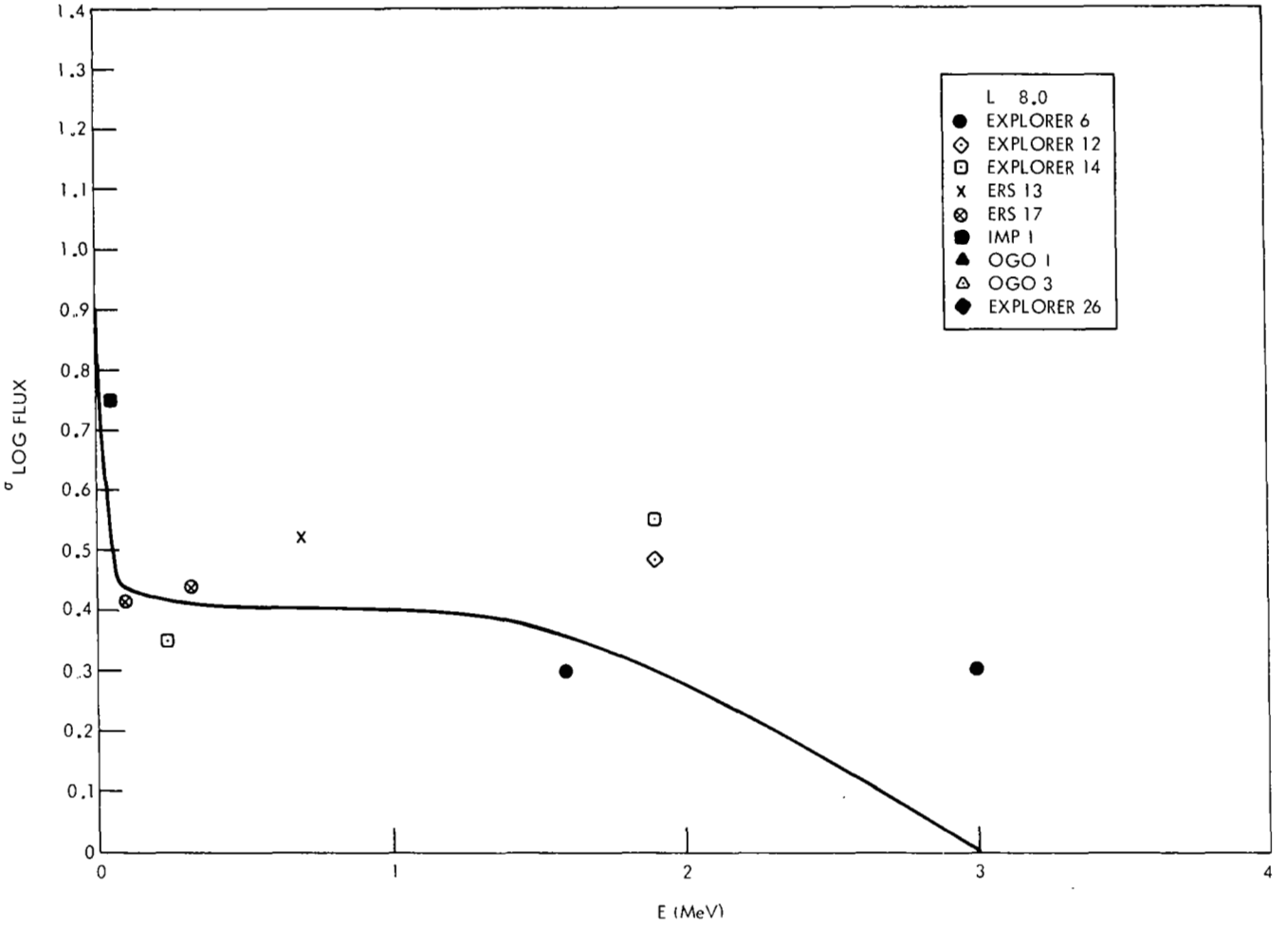

Figure 82. Comparison of AE-4 Model Standard Deviation with Standard Deviation from Data Sets, L = 8.0

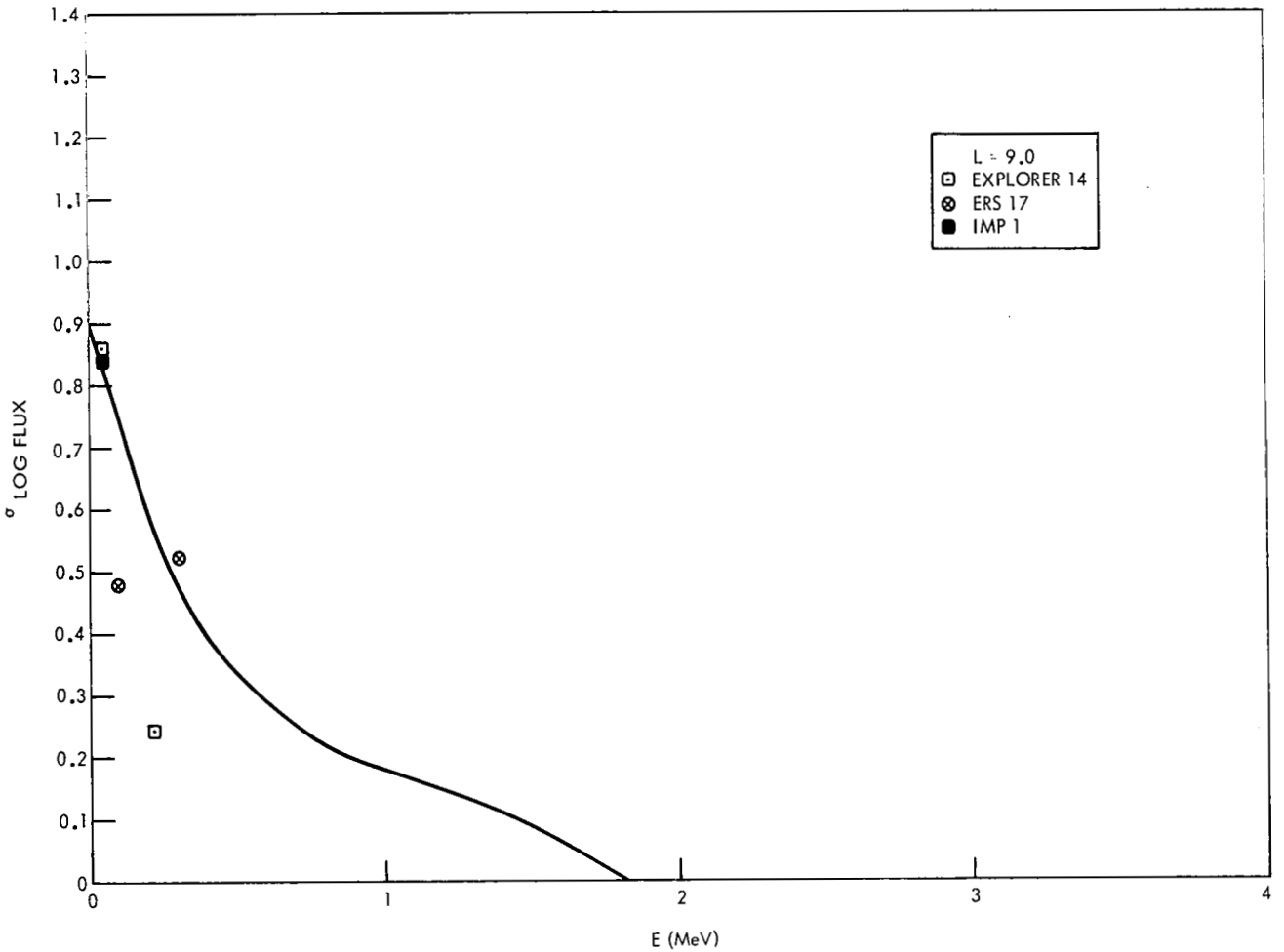

Figure 83. Comparison of AE-4 Model Standard Deviation with Standard Deviation from Data Sets, L = 9.0

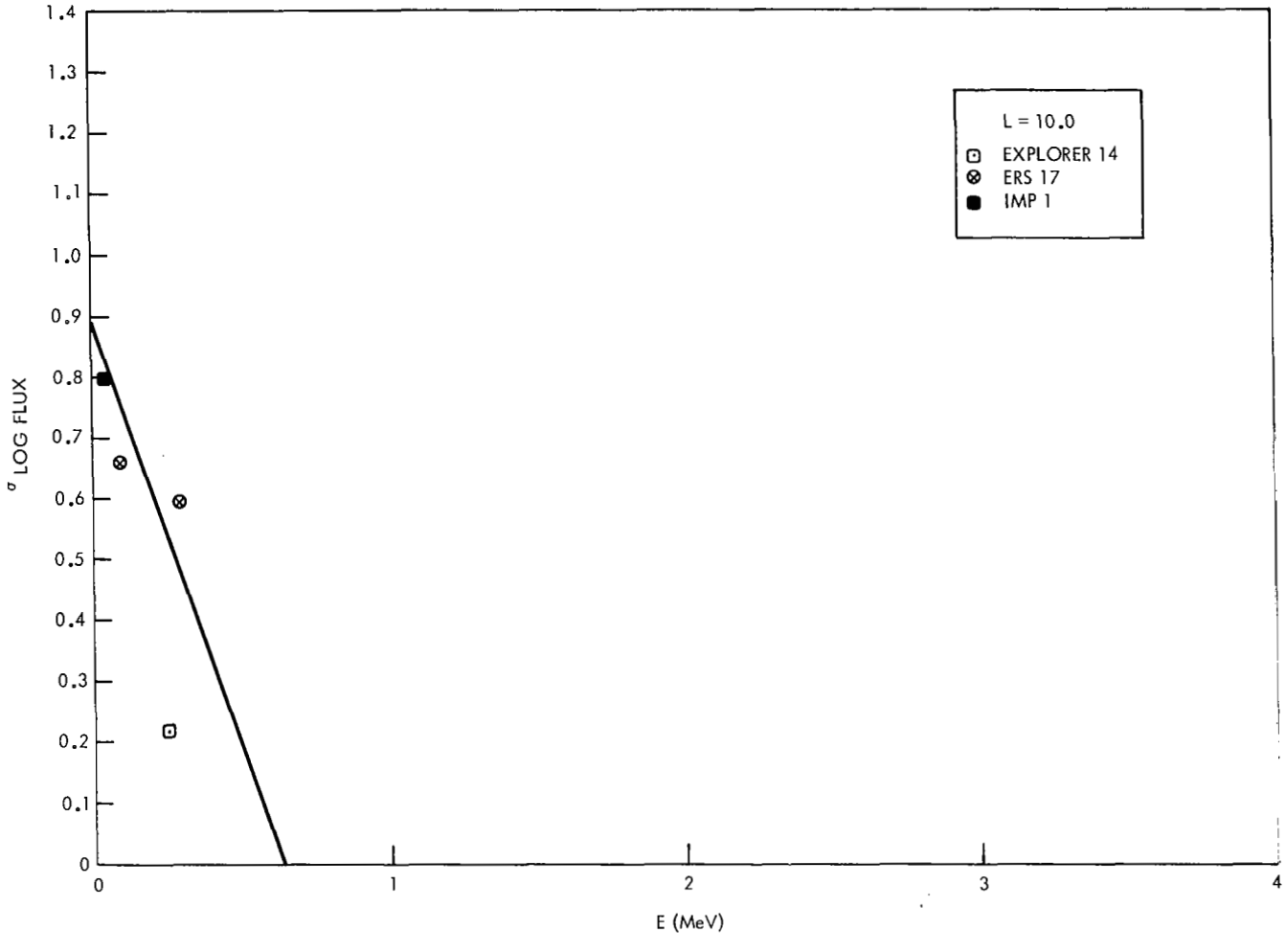

Figure 84. Comparison of AE-4 Model Standard Deviation with Standard Deviation from Data Sets, L = 10.0

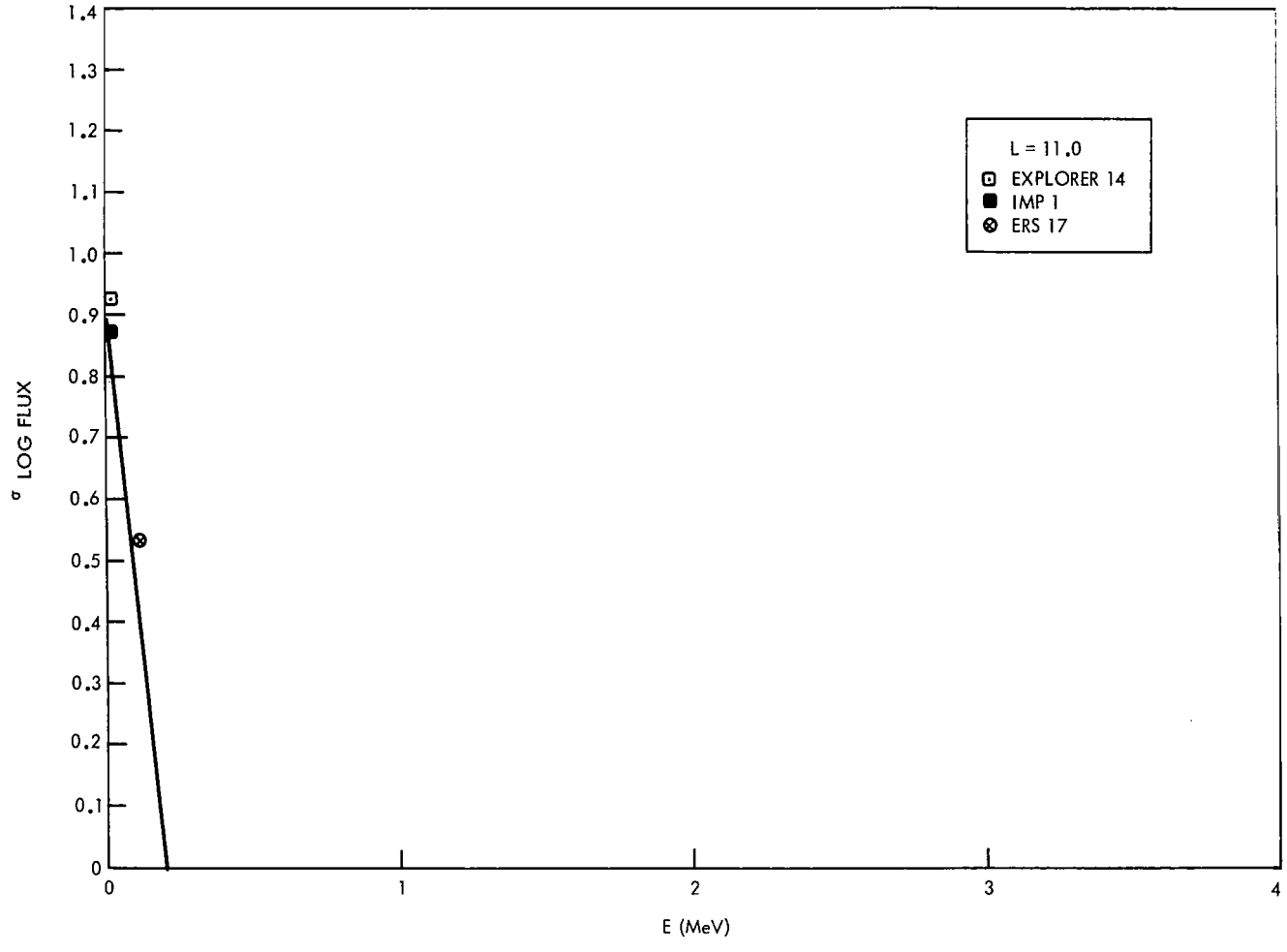

Figure 85. Comparison of AE-4 Model Standard Deviation with Standard Deviation from Data Sets, L = 11.0

* U.S. GOVERNMENT PRINTING OFFICE: 1972—736-964/314